

**The Mirror Alignment and Control
System of H.E.S.S. Phase II, and
Observational Studies of TeV Shell
Candidates and of the Nova Sgr 2015
No. 2 with H.E.S.S.**

Dissertation

der Mathematisch-Naturwissenschaftlichen Fakultät
der Eberhard Karls Universität Tübingen
zur Erlangung des Grades eines
Doktors der Naturwissenschaften
(Dr. rer. nat.)

vorgelegt von
Daniel Gottschall
aus Herrenberg

Tübingen
2018

Gedruckt mit Genehmigung der Mathematisch-Naturwissenschaftlichen
Fakultät der Eberhard Karls Universität Tübingen.

Tag der mündlichen Qualifikation: 13.07.2018

Dekan: Prof. Dr. Wolfgang Rosenstiel

1. Berichterstatter: Prof. Dott. Andrea Santangelo

2. Berichterstatter: Prof. Dr. Josef Jochum

I appreciated the effort that the moonlight had made to reach me. It had left the sun at around 186 000 miles per second, and had then proceeded through space for eight minutes, or ninety-three million miles, and had then upped off the moon's surface and proceeded through space for another 1.3 seconds or 240 000 miles, before pushing through troposphere, stratosphere and atmosphere, and descending on me: trillions of lunar photons pelting on to my face and the snow about me, giving me an eyeful of silver, and helping my moon-shadow to dance.

Robert Macfarlane, *The Wild Places*

Abstract

The High Energy Stereoscopic System (H.E.S.S.) is a hybrid system of five Imaging Atmospheric Cherenkov Telescopes of two different types designed to detect very high energy γ -rays with energies from tens of GeV to tens of TeV.

One key component of the telescopes are the reflective dishes with mirror areas of 614 m^2 for the large size telescope CT5 and 108 m^2 for the medium size telescopes CT1-4 consisting of a large number of mirror segments. The first part of these thesis deals with the alignment of the telescopes. The initial alignment of the larger telescope CT5 has been studied in this work, resolving a problem with the monitoring of the quality of the alignment. After improving the system, a new alignment was done and the possibility of using a fast re-pointing for transient sources from a mirror alignment perspective was investigated and successfully commissioned. Continuous support for the alignment system was provided, including a long-term monitoring system of the stability of the alignment and a new alignment of CT3 after a mirror exchange.

The second part of the thesis covers a study of new supernova remnants (SNRs) discovered at TeV energies. The large field of view of H.E.S.S. is well suited for survey observations and very extended sources. Based on the H.E.S.S. Galactic plane survey (HGPS), for the first time, very high energy (VHE) γ -ray sources were selected as supernova remnant (SNR) candidates solely based on VHE γ -ray observations. The three SNR candidates HESS J1534–571, HESS J1614–518 and HESS J1912+101 were studied in detail including available multi-wavelength information. HESS J1534–571 was associated with a SNR candidate in the radio band and therefore classified as SNR. Possible emission scenarios were investigated even though the results remain inconclusive for the time being.

The thesis has been concluded with a study of the nova V 5668 Sgr at TeV energies. The discovery of emission from classical novae in the GeV band with the Large Area Telescope on the Fermi Gamma Ray Space Telescope Spacecraft (*Fermi-LAT*) triggered an increased activity of H.E.S.S. to observe bright or in the GeV band detected novae. The nova V 5668 Sgr was the first nova observed with the newer telescope CT5 optimized for low energy observations. The source was not detected with H.E.S.S., but based on the detection with *Fermi-LAT* and the upper limits derived from the H.E.S.S. data, the hadronic component of an emission model was constraint.

Kurzzusammenfassung

Das High Energy Stereoscopic System (H.E.S.S.) ist ein System aus fünf abbildenden atmosphärischen Cherenkov-Teleskopen, gebaut, um γ -Strahlung bei höchsten Energien von einigen zehn GeV bis zu einigen zehn TeV zu messen. Ein Schlüsselsystem der Teleskope ist der Hauptspiegel mit einer Fläche von 614 m^2 für das größere Teleskop CT5 beziehungsweise 108 m^2 für CT1-4, der aus vielen einzelnen Spiegelsegmenten besteht. Die erste Spiegelausrichtung von CT5 wurde untersucht. Dabei wurde ein Problem mit Überwachung der Qualität der Spiegelausrichtung gefunden und behoben. Das System für die Spiegelausrichtung wurde verbessert und eine neue Spiegelausrichtungskampagne durchgeführt. Die Möglichkeit einer schnellen Neupositionierung des Teleskops für transiente Quellen wurde untersucht und erfolgreich in Betrieb genommen. Fortdauernde Unterstützung, einschließlich die Überwachung der Qualität der Ausrichtung und einer Spiegelausrichtungskampagne für CT3 wurde geleistet.

Der zweite Teil der Arbeit beschäftigt sich mit einer Studie von Kandidaten für Supernovaüberreste, die im TeV-Energieband entdeckt wurden. Das große Gesichtsfeld von H.E.S.S. eignet sich gut für eine Vermessung großer Himmelsregionen und ausgedehnter Quellen. Basierend auf der H.E.S.S. Galactic plane survey (HGPS), einer Vermessung weiter Teile der galaktischen Ebene, wurden zum ersten Mal Kandidaten für Supernovaüberreste allein anhand von Beobachtungen im TeV-Band ausgewählt. Die drei Supernovaüberrestkandidaten HESS J1534–571, HESS J1614–518 und HESS J1912+101 wurden detailliert untersucht, inklusive Daten anderer Frequenzbänder. Der Supernovaüberrestkandidat HESS J1534–571 konnte mit einem Kandidaten aus dem Radioband assoziiert werden, was zu einer Klassifizierung als Supernovaüberrest führte. Die Arbeit wird mit einer Studie der Nova V 5668 Sgr im TeV-Energieband abgeschlossen. Die Entdeckung hochenergetischer γ -Strahlung von galaktischen Novae mit dem Large Area Telescope on the Fermi Gamma Ray Space Telescope Spacecraft (*Fermi-LAT*) führte zu einem verstärkten Interesse, diese Quellen auch mit H.E.S.S. zu beobachten. Die Nova V 5668 Sgr ist die erste Nova, die sowohl mit dem neueren Teleskop CT5, optimiert für niedrige Energien, als auch mit *Fermi-LAT* beobachtet wurde. Die Quelle wurde mit H.E.S.S. nicht nachgewiesen, aber zusammen mit den Daten von *Fermi-LAT* wurde eine Grenze für eine hadronische Komponente eines Emissionsmodells abgeleitet.

Contents

Abstract	I
Kurzzusammenfassung	III
List of Figures	IX
List of Tables	XIII
Acronyms	XV
1 Introduction	1
2 Scientific Background	5
2.1 Introduction to Cosmic Rays	5
2.1.1 The Cosmic Ray Spectrum	5
2.1.2 Acceleration Processes	6
2.2 Measuring the Origin of Cosmic Rays and an Introduction to γ -ray Emission Processes	12
2.2.1 Emission Mechanisms	13
2.2.2 Summary	16
3 The Imaging Atmospheric Cherenkov Technique	17
3.1 Introduction	17
3.2 Extended Air Showers	17
3.2.1 Electromagnetic Showers	18
3.2.2 Hadronic Showers	20
3.2.3 The Emission of Cherenkov Light	21
3.2.4 Summary of Extended Air Showers	23
3.3 The High Energy Stereoscopic System (H.E.S.S.)	25
3.3.1 Site Location	27
3.3.2 Telescope Structure and Drive System	27
3.3.3 Mirror System	28
3.3.4 Photomultiplier Tube Camera	28
3.3.5 The Trigger System	29

3.3.6	Calibration	29
3.3.7	Monte Carlo Simulations	32
3.3.8	Quality Selection	32
3.3.9	Event Reconstruction	33
3.3.10	Background Estimation	37
3.3.11	Perfomance of H.E.S.S.	39
4	The Mirror Alignment and Control System for H.E.S.S. Phase II	45
4.1	Introduction	45
4.2	Components of the Alignment System	47
4.2.1	Mechanical Components	47
4.2.2	Electronic Components	49
4.2.3	The CCD Camera	51
4.3	Alignment Software	51
4.3.1	Panel Control Board	52
4.3.2	Central Control Computer	52
4.4	The Alignment Algorithm	53
4.4.1	Mathematical Description	53
4.4.2	Alignment Procedure	54
4.5	Results of the Initial Alignment and Interpretation	55
4.5.1	Results	55
4.5.2	Interpretation	57
4.6	Final Alignment	60
4.7	Results	61
4.7.1	Point Spread Function	61
4.7.2	Long Term Stability	63
4.8	Reverse Pointing for Prompt Follow Up Target of Opportunity Observa- tions	64
4.8.1	Introduction	64
4.8.2	Impact on the Optical System	66
4.8.3	Impact on the Air Shower Reconstruction	68
4.9	The 2017 Mirror Exchange of CT3	71
4.10	Summary	75
5	A Study of Three TeV Shell Candidates from the H.E.S.S. Galactic Plane Survey with H.E.S.S.	77
5.1	Introduction and Outline	77
5.1.1	Introduction	77
5.1.2	Outline	79

5.2	Search for New TeV Shell Candidates in the H.E.S.S. Galactic Plane Survey	80
5.2.1	The H.E.S.S. Galactic Plane Survey	80
5.2.2	Search Method	81
5.2.3	Results	85
5.3	Source-by-Source Analysis	87
5.3.1	Analysis of Available H.E.S.S. Data	88
5.3.2	Sky Maps	91
5.3.3	Morphology Study	93
5.3.4	Spectral Analysis	100
5.4	Search for Multi-Wavelength Counterparts	103
5.4.1	HESS J1534–571	105
5.4.2	HESS J1614–518	109
5.4.3	HESS J1912–101	112
5.5	Discussion	116
5.5.1	TeV Emission from Leptons or Protons	118
5.6	Summary	119
6	Target of Opportunity Observation of the Classical Nova Sgr 2015 No. 2 with H.E.S.S.	121
6.1	Introduction	121
6.2	Observation of the Classical Nova Sgr 2015 No. 2 with H.E.S.S.	123
6.3	Analysis of Available H.E.S.S. Data	124
6.3.1	Data Quality	124
6.3.2	Skymap and Upper Limits	124
6.3.3	<i>Fermi</i> -LAT Data Set	127
6.3.4	Interpretation	128
6.4	Target of Opportunity Observation Program of Novae with H.E.S.S.	129
6.5	Summary	129
7	Conclusions and Outlook	131
	Bibliography	135
A	Appendix	i
A.1	Optical Point Spread Function Monitoring of H.E.S.S.	ii
	Acknowledgments	v

List of Figures

2.1	Cosmic ray spectrum 1	7
2.2	Cosmic ray spectrum 2	8
2.3	Diffusive shock acceleration	10
2.4	Hillas plot	11
3.1	Extended air shower development, Heitler model	18
3.2	Extended air shower development, simulations	21
3.3	Production of Cherenkov radiation	22
3.4	Performance comparison of γ -ray observatories	25
3.5	H.E.S.S. phase II at night	26
3.6	Events recorded by H.E.S.S.	33
3.7	Hillas parametrization	34
3.8	γ /hadron separation based on shower parameters	35
3.9	Background determination methods of H.E.S.S.	37
3.10	Background determination methods of H.E.S.S. with exclusion regions	38
3.11	Effective area and angular resolution of H.E.S.S.	40
3.12	Energy bias and energy resolution of H.E.S.S.	42
3.13	Energy bias and energy threshold of H.E.S.S.	43
3.14	Differential sensitivity of H.E.S.S. II	44
4.1	Basic principle of the mirror alignment	46
4.2	Picture of CT5	47
4.3	Image of the mechanical components of mirror alignment and control system for H.E.S.S. phase II (MACSII)	48
4.4	Structure of the dish of CT5	50
4.5	Electronic board of the alignment system	50
4.6	Block diagram of the alignment system	51
4.7	Results of the first alignment of CT5	56
4.8	Mirror point spread function (psf) from quality measurements	58
4.9	Azimuth offset of the main spot	60
4.10	Dark time efficiency of CT1-4 during the alignment of CT5	61
4.11	Result of the final mirror alignment of CT5	62

4.12	Long term monitoring of the optical psf of CT5	64
4.13	Performance of the CT5 drive system	66
4.14	Mirror of CT5 from the back	67
4.15	Time evolution of the optical psf after a reverse pointing	68
4.16	Optical psf for reverse pointing	69
4.17	γ -ray performance for reverse pointings	70
4.18	Muon efficiency over time	72
4.19	Optical psf for CT03	73
4.20	Darktime efficiency of the full array during the CT3 mirror exchange campaign	74
4.21	Muon efficiency of CT3 over time	74
5.1	Illustration of the HGPS	81
5.2	Difference in test statistics ΔTS , Shell versus Gaussian hypothesis . . .	85
5.3	Significance maps for the shell candidates	94
5.4	Azimuthal profiles for the three TeV shell candidates	98
5.5	Radial profiles for the three TeV shell candidates	99
5.6	Flux points and power-law models of the shell candidates with H.E.S.S.	104
5.7	TeV and radio continuum sky map of HESS J1534–571	106
5.8	Elliptical profiles of HESS J1534–571 and G323.7–1.0, and pull distri- bution	107
5.9	TeV sky map and MeV to TeV SED of HESS J1614–518	109
5.10	Infra-red (IR) composite image from Spitzer and <i>XMM-Newton</i> hard band of HESS J1614–518	111
5.11	TeV surface brightness sky map and excess map from 2008	112
5.12	Sky maps from a re-analysis of the 2008 data set of HESS J1912–101 . .	114
5.13	Azimuthal profiles of the full data set overlaid with the reduced data set of HESS J1912–101	115
6.1	Differential sensitivity of different H.E.S.S. cut sets at several energies as a function of observation time, in comparison with Fermi-LAT	122
6.2	Pixel participation fraction of two CT5 mono runs	125
6.3	Significance map for Nova Sgr 2015 No. 2	125
6.4	<i>Fermi-LAT</i> results for Nova Sgr 2015 No. 2	127
6.5	Spectral energy distribution for Nova Sgr 2015 No. 2	129
A.1	Long term monitoring of the optical psf of CT1	ii
A.2	Long term monitoring of the optical psf of CT2	ii
A.3	Long term monitoring of the optical psf of CT3	iii
A.4	Long term monitoring of the optical psf of CT4	iii

A.5 Long term monitoring of the optical psf of CT5 iv

List of Tables

4.1	List of parameters of the mechanical parts of the mirror alignment system	49
4.2	Simulated and measured psf of individual mirror segments	59
4.3	Fit parameters to model the dish bending of CT5	62
4.4	Yearly increase of the psf size for all telescopes	63
4.5	Increase in energy threshold for reverse pointings	70
4.6	Muon efficiency November 2017	74
5.1	List of tested Gaussian (H_0) and shell (H_1) parameters for the grid search	84
5.2	List of candidates from the search and "by eye" candidates	84
5.3	List of the search results of the known shell-like SNRs in the survey region	86
5.4	Number of observation runs and observation time for the mophology study	89
5.5	Number of observation runs and observation time for the spectral analysis	89
5.6	Fit parameter to the significance with exclusion distribution of the shell candidates	95
5.7	Acceptance-corrected livetime and statistics for the shell candidates . .	95
5.8	Results of the morphology study of the shell candidates	97
5.9	Acceptance-corrected observation time for the spectral analysis	100
5.10	Spectral fit results from the power-law fits to the H.E.S.S. data	103
5.11	Basic parameters of known SNRs and the new shell-like sources	117
5.12	Proton energy content of HESS J1534–571, HESS J1614–518, and HESS J1912+101	119
6.1	Livetime and event statistics for the ring background method for Nova Sgr 2015 No. 2	126
6.2	Livetime and event statistics for the reflected region background method for Nova Sgr 2015 No. 2	126
6.3	Differential upper limits derived for Nova Sgr 2015 No. 2	127

Acronyms

ADC analog-to-digital converter

AGN active Galactic nuclei

BDT boosted decision tree

CCD charge-coupled device

CCO central compact object

CMB cosmic microwave background

CORSIKA Cosmic Ray Simulations for the Karlsruhe Shower Core and Array
Detector

CR cosmic ray

CTA Cherenkov Telescope Array

DAQ data aquisition

DSA diffusive shock acceleration

EAS extended air shower

EBL extragalactic background light

FoV field of view

FPGA field-programmable gate array

GRB gamma-ray burst

HAWC the High-Altitude Water Cherenkov Gamma-Ray Observatory

HEGRA High-Energy-Gamma-Ray Astronomy

H.E.S.S. High Energy Stereoscopic System

HE high energy

- HGPS** H.E.S.S. Galactic plane survey
- IAAT** Institut für Astronomie und Astrophysik Tübingen
- IACT** Imaging Atmospheric Cherenkov Telescope
- ImPACT** Image Pixel-wise fit for Atmospheric Cherenkov Telescopes
- I/O** Input/Output
- IR** infra-red
- ISM** interstellar medium
- LED** light-emitting diode
- LHC** large hadron collider
- LMC** Large Magellanic Cloud
- LRT** likelihood ratio test
- LST** large sized telescope
- MACSII** mirror alignment and control system for H.E.S.S. phase II
- MACS** mirror alignment and control system
- MAGIC** Major Atmospheric Gamma Imaging Cherenkov Telescopes
- MC** molecular clouds
- MGPS-2** Molonglo Galactic Plane Survey 2nd Epoch
- MOST** Molonglo Observatory Synthesis Telescope
- MPIK** Max-Planck-Institut für Kernphysik
- MRSL** mean reduced scaled length
- MRSW** mean reduced scaled width
- MST** medium sized telescope
- MSX** Midcourse Space Experiment
- MWL** multi-wavelength
- NSB** night sky background
- pe** photo-electrons

PMT photomultiplier tube

psf point spread function

PWN pulsar wind nebula

rms root mean square

SED spectral energy distribution

SEP Solar Energetic Particle

SGPS Southern Galactic Plane Survey

SNR supernova remnant

SST small sized telescope

TCP/IP Transmission Control Protocol and the Internet Protocol

TMVA Toolkit for Multivariate Data Analysis with ROOT

ToO targets of opportunity

UHECR Ultra High Energy Cosmic Ray

UV ultraviolet

VERITAS Very Energetic Radiation Imaging Telescope Array System

VHE very high energy

1 Introduction

In 1912 two scientists, Victor Hess and Domenico Pacini, investigated the origin of ionizing radiation on Earth. Whereas Victor Hess measured the amount of radiation for different altitudes using balloon flights, Domenico Pacini submerged a similar detector in the water of the Bay of Livorno. Hess measured a rise of the radiation level by a factor of two at five kilometers above sea level. Pacini's result showed the opposite, the radiation level sank significantly under water (Pacini, 1912). Both of them concluded correctly that the source of the radiation can not be on Earth, but must have extraterrestrial origin. For this discovery, Victor Hess was awarded the Nobel prize in 1936¹.

Since then the study of cosmic rays became a very active field in science, for example to study newly discovered particles like the positron (Anderson, 1933). Though many theories on the origin of cosmic rays were proposed, the nature of the sources stayed mainly unknown because the charged particles of the cosmic rays are deflected on their way to Earth by magnetic fields, especially the Galactic magnetic field. Observations of very high energy (VHE) γ -ray emission from astrophysical objects opened up a new window to understand the acceleration process of charged particles that arrive on Earth as cosmic rays. This work was one of the objectives of the High Energy Stereoscopic System (H.E.S.S.) collaboration and covers a broad range of topics ranging from instrumentation to the analysis and interpretation of different source classes.

Chapter 2 contains a summary of the current knowledge about cosmic rays in general and about the acceleration processes and potential sources of cosmic rays. Energetic charged particles can produce γ -rays close to the acceleration sites. The emission processes are described in section 2.2.

The High Energy Stereoscopic System (H.E.S.S.) (Aharonian et al., 2006b) was used as the primary instrument in this thesis for studying γ -rays from possible cosmic ray accelerators. It is a system of five Imaging Atmospheric Cherenkov Telescopes (IACTs) sensitive to photons in the broad energy band from 30 GeV to 100 TeV. A detailed description of IACTs in general and the H.E.S.S. in particular can be found in chapter 3.

¹https://www.nobelprize.org/nobel_prizes/physics/laureates/1936/; Together with Carl Anderson for discovering the positron by studying Cosmic Rays

One main component of IACTs is the reflector. These reflectors consist of up to several hundred mirror segments that need to be aligned precisely.

One part of the work deals with the continuous support of the Institut für Astronomie und Astrophysik Tübingen (IAAT) for the MACSII including hardware and software maintenance, monitoring of the precision of the alignment, detailed measurements for the instrument simulation, and the adjustment of mirror segments. A new alignment of all 876 mirror segments of the largest, fifth telescope turned out to be necessary. In preparation to that, improvements to the existing alignment system were implemented. The result of the alignment was verified and a long term monitoring of the hardware status and the optical properties was established and is still underway. In chapter 4 the technical details of the mirror alignment and control system (MACS) are described. Furthermore, the improvements implemented for the re-alignment and the results of the alignment campaign are presented. The mirror segments are not protected against rain, high humidity, dirt or the sun. As a result, the reflectance is degrading over the years which directly impacts the performance of the telescopes. For one of the four 12 m telescopes, maintenance of the alignment system, a mirror exchange and a full alignment of 381 mirror segments was planned and carried out to restore the efficiency of the telescope.

For observations of gamma-ray bursts (GRBs), a fast re-pointing of the telescope is desirable. Gamma-ray bursts are transient phenomenon lasting only for a very short time. To minimize the angular distance to the observation position of a prompt GRB alert, the 28 m telescope CT5 of H.E.S.S. is exceeding the normal mode elevation range of 0° to 90° . The telescope moves through zenith on the target using the fastest and shortest way. This so called reverse mode has an impact on the optical psf of the telescope. The impact of the reverse mode was studied in detail, and is reported in this thesis.

This work does not exclusively focus on instrumental activities. A large fraction of it is devoted to data analysis and data interpretation. Supernova remnants are proposed to be one of the main sources of Galactic cosmic rays (CRs). The shock fronts formed by the expanding gas from the supernova explosion are efficiently accelerating charged particles to very high energy. The number of supernova remnants (SNRs) detected at VHE γ -ray is limited. Based on the nine years long H.E.S.S. Galactic plane survey (HGPS), a systematic search for SNRs based on their shell like appearance was done. With this approach four candidates were identified. These four sources were analyzed with data selection and analysis cuts optimized for the individual sources. A detailed morphology study revealed that three of these sources have a significant shell morphology and are therefore classified as SNR candidates. Two of these sources have no further indication

supporting the SNR scenario, but for one source, HESS J1534+57, a SNR candidate in the radio Molonglo Galactic Plane Survey 2nd Epoch (MGPS-2) has been identified. Therefore, HESS J1534+571 is classified as SNR. The analysis is described in detail in chapter 5. Furthermore, the sources are put in a multi-wavelength (MWL) context ranging from radio to GeV-energies.

The H.E.S.S. is dedicating one fourth of its observation time to targets of opportunity (ToO) observations. Targets of opportunity are sources visible to the observatory, but not part of the observation schedule. Reasons to observe outside the schedule can be sudden changes of the properties of a source, or a transient phenomena, for example, GRBs. One of the source classes the H.E.S.S. is triggering on are Galactic nova explosions. The Large Area Telescope of the Fermi Gamma-ray Space Telescope detected Galactic novae at GeV energies. The sources show a hard spectrum without a significant cut off, and they are active for up to three weeks. Many models were proposed to explain the emission seen, some predicting significant emission at VHEs. So far no VHE emission has been discovered. In chapter 6 a description of the observation of the nova Sgr 2015 No. 2 is given in addition to details on the analysis performed to derive upper limits. Assuming a specific model, the ratio of luminosity stemming from proton interaction to the luminosity from leptonic emission has been constrained as well as an estimation of the required observation time needed to further constrain the emission processes of this source class.

2 Scientific Background

2.1 Introduction to Cosmic Rays

The discovery of CRs established by Victor Hess posed a major task for both theoreticians and observers. Sources can not be identified directly by observing CRs themselves because these particles are deflected in the intervening magnetic fields. Only indirect measurements are possible. One approach is to measure the spectrum in great detail. The idea is to distinguish different acceleration processes by analyzing features in the CR energy spectrum. Another approach is based on measuring at the composition of particles. An alternative way to study the origin of cosmic rays is to look at the properties of non-thermal electromagnetic radiation ranging from radio to VHE γ -rays. In this section the current knowledge about the CR spectrum, the dominant acceleration process, and the accelerators are discussed.

2.1.1 The Cosmic Ray Spectrum

The term cosmic rays (CRs) refers to massive energetic particles. The use of "ray" is misleading in this context, but the term is motivated historically. Most abundant in CRs are protons and heavier nuclei. They account for about 98% of the particles. About 87% of these hadronic particles are protons. A much smaller fraction consists of electrons, positrons and antiprotons. A measurement of the CR abundances is presented in Longair (2011). The measured CR spectrum ranges over eleven decades in energy and over ten decades in flux continuously dropping with increasing energy. Figure 2.1 shows the cosmic ray energy spectrum as measured with various experiments from a few GeV to 1×10^{11} GeV. For comparison, the energy reach in the center of mass for particle colliders like the large hadron collider (LHC) is shown. At lowest energies the Galactic CRs are cutting off due to the magnetic field of the Earth. The flux is modulated with the solar activity. Low energy CRs diffuse toward Earth from interstellar space through the outflowing solar wind. The flux at these energies is higher for low solar activity because greater solar activity leads to greater disturbances in the interplanetary magnetic field which hinders the propagation of the particles (Longair, 2011). Another

population of particles is accelerated by the sun. Usually they are referred to as Solar Energetic Particles (SEPs) to differentiate them from CRs. Protons can reach GeV energies (Reames, 2013). The source of CRs with lower energy is believed to be Galactic. Above the regime of the solar modulation, the spectrum is well described by a power law:

$$\frac{dN}{dE} \propto E^{-\Gamma}. \quad (2.1)$$

with an index of $\Gamma = 2.7$ (Longair, 2011). This is compatible with the idea of an acceleration at a shock front inside astrophysical sources like SNRs. At roughly 1 PeV the spectrum becomes softer while the composition changes to heavier nuclei. This feature is called "the knee". The acceleration process is thought to change in this energy range. It is possible that the majority of the sources is no longer able to confine CRs with low mass at these energies and thus cannot further accelerate them, whereas ions with higher mass can still be accelerated. Starting from the knee to higher energies, there is an indication of a second knee at $E \sim 1 \times 10^{18}$ eV. This feature is believed to originate from the maximum energy to which iron is accelerated in Galactic sources.

Figure 2.2 shows the cosmic ray spectrum in flux times the cubic energy. The features in the spectrum are much more pronounced. Assuming strong magnetic fields in super nova shock waves, the simulated energy spectra for different species of particles from protons to iron is shown as well. The superposition of these spectra accounts for the measured one including the first and second knee (Longair, 2011). A clear hardening of the spectrum at around 1×10^{19} eV is visible in both figures. This region is referred to as the overlap region between Galactic and extra Galactic CRs which dominate at energies larger than 1×10^{18} eV (Gaisser, 2017). Greisen, Zatsepin, and Kuzmin described a process in which particles with energies larger than 5×10^{19} eV interact with photons of the cosmic microwave background (CMB) and lose energy in the process therefore predicting a cut-off in the spectrum at around this energy if the primary particles are protons. Heavier nuclei may reach higher energies (Zatsepin & Kuz'min, 1966; Greisen, 1966; Longair, 2011).

2.1.2 Acceleration Processes

The acceleration processes need to reproduce the observed CR spectrum and therefore follow a power-law energy spectrum. The index of this energy spectrum Γ should be in the range of 2 to 3 to account for the observed index of $\Gamma \sim 2.7$. The energies achieved by these processes should be at least 1×10^{20} eV to account for the highest energy CR observed by the *Auger Observatory* (Abraham et al., 2004) and the *Telescope*

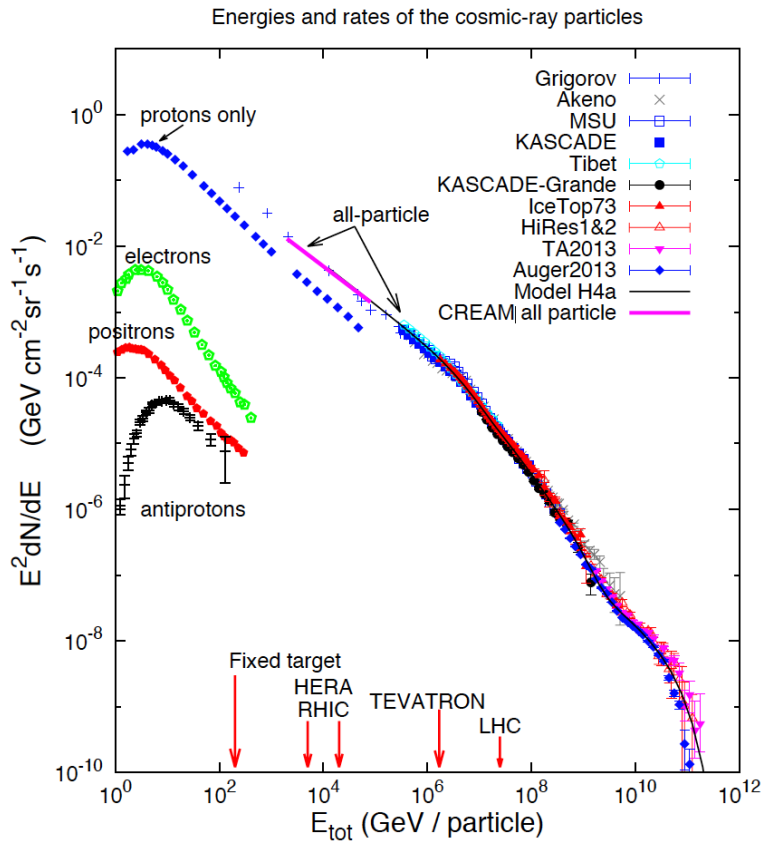


Figure 2.1: Cosmic ray spectrum: Measurements of the CR spectrum from a few GeV to 1×10^{11} GeV measured by various experiments. For comparison the energy of some particle colliders is indicated with a red arrow. Visible are the "knee" at 1 PeV where the spectrum becomes softer because the acceleration process in Galactic sources changes, and the "ankle" at 1×10^{19} eV where the spectrum becomes harder because a new component, supposedly of extra Galactic origin, is visible (Fig. 2.1 of Gaisser et al., 2016).

Array project (Abu-Zayyad et al., 2012). First attempts to describe a process fulfilling these requirements were done by Fermi (1949) assuming shock acceleration of charged particles. Nowadays, the dominant process is believed to be diffusive shock acceleration (see section 2.1.2.1) building up on Fermi's idea. One shortcoming of this theory is the quite complicated explanation of energies above 1×10^{18} eV, where additional factors need to be taken into account, for example an amplification of the magnetic flux density due to a number of possible streaming instabilities. For details refer to Longair (2011).

2.1.2.1 Diffusive Shock Acceleration

This section is based on the description of Longair (2011). Diffuse shock acceleration DSA is taking place in the vicinity of strong shocks and the gain in energy of the particle

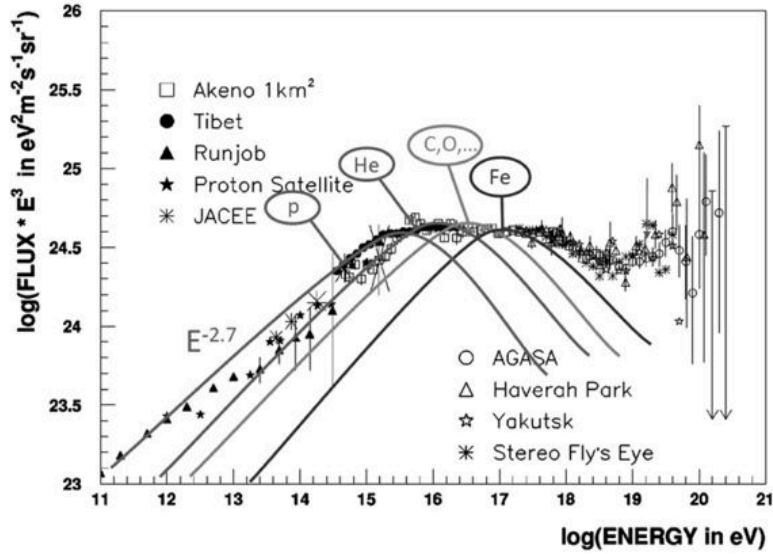


Figure 2.2: Cosmic ray spectrum: Measurements of the cosmic ray spectrum in flux times the cubic energy. The features in the spectrum are much more pronounced. Assuming strong magnetic fields in super nova shock waves, the superposition of energy spectra from particles with different mass could account for the measured total energy spectrum including the two softening in the spectra, the so called first and second knee (Fig. 17.9 of Longair, 2011).

comes from the shock velocity. A strong shock is characterized by a nearly discontinuous change in density, temperature, and pressure in a medium moving with supersonic speed. The accelerated particle gains energy passing through the shock regardless of whether it is in the upstream (in front of the shock front) or downstream (behind the shock front) region, because in the rest frame of either region, the gas of the other region is moving towards the particle with a velocity of $\frac{3}{4}U$, where U is the velocity of the shock front through the medium. In a fully ionized or monotonic gas, the ratio of the heat capacity is $\gamma = \frac{5}{3}$. For a strong shock, the shock front is described with a compression factor (upstream over downstream density) of $\frac{\rho_2}{\rho_1} \approx \frac{\gamma+1}{\gamma-1} = 4$. In the rest frame of the shock, from the equation of continuity:

$$\rho_1 v_1 = \rho_2 v_2 \quad (2.2)$$

the velocity of the gas in the downstream region is $v_2 = \frac{1}{4}$ of the velocity in the upstream region v_1 . Now, considering a particle from the upstream region in the rest frame of the upstream region, the particle gains energy because the shock is approaching with a velocity of $\frac{3}{4}U$. It is then scattered losing the original direction. Therefore, one particle can make multiple shock front crossings. When moving to the rest frame of the downstream region the picture is exactly the same. Again the shock front is approaching

a particle of the downstream region with a velocity of $\frac{3}{4}U$ (see figure 2.3). It can be shown that the average gain in energy for each crossing is:

$$\left\langle \frac{\Delta E}{E} \right\rangle = \frac{2V}{3c} \quad (2.3)$$

where $V = \frac{3}{4}U$ is the velocity of the gas approaching the particle in the rest frame of the up- or downstream region. In the rest frame of either region, the high energy particles are fully isotropic. When passing through the shock, the particles scatter randomly with irregularities of the magnetic fields caused by streaming instabilities or turbulent motions on either side of the shock. Therefore, because in the rest frame of each region an isotropic population is present, the shock is approaching both regions with the same velocity and the movement becomes isotropic again when passing through the shock, a particle gains a small amount of energy ΔE each time. The acceleration of the particles is only limited by the time the particles remain in the vicinity of the shock. Using the probability P that the particle remains in the region of the front, and with the energy gain $\beta = \frac{E}{E_0}$ after a collision, the spectrum of a population of mono energetic particles after undergoing diffusive shock acceleration (DSA) results to be proportional to a power law:

$$N(E) dE \propto E^{-1 + \frac{\ln P}{\ln \beta}} dE. \quad (2.4)$$

Furthermore, for a strong shock the fraction of the natural logarithm of the probability to the efficiency is $\frac{\ln P}{\ln \beta} = -1$. In conclusion, the resulting energy spectrum of particles in the vicinity of a strong shock not only follows a power law, but the index is also of the order of $\Gamma = 2$. This fulfills both properties of the observed spectrum of CRs.

The question remains, which maximum energies can be achieved by the process. This depends on the time the particle spends in the vicinity of the shock and is given by the size of the accelerating region and the strength of the magnetic fields. A more detailed discussion can be found in the next section.

2.1.2.2 Accelerators

The conditions of DSA are fulfilled by many astrophysical objects. To explain the observed CR spectrum, the following question remains: Which are the the sources that can reach very high energies of the order of 1×10^{15} eV for protons for Galactic accelerators and energies up to 1×10^{20} eV for extragalactic accelerators. The energies

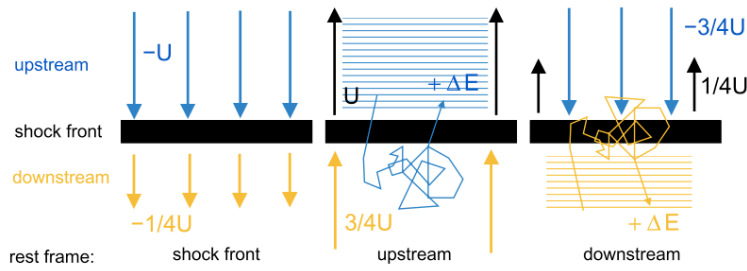


Figure 2.3: Diffusive shock acceleration: The plot on the left shows the gas in the upstream region moving with the velocity U and in the downstream region with the velocity $\frac{1}{4}U$. This is the case for the rest frame of the shock front and for a ratio of the heat capacity of $\gamma = \frac{5}{3}$. The plot in the middle and on the right shows the same scenario in the rest frame of the up- and the downstream region. In both cases a particle from the region in the rest frame sees the gas approaching with a velocity of $\frac{3}{4}U$. When passing through the shock front and scattered back, the particle gains the energy ΔE (Funk, 2005).

achievable by the process are limited by the time the particles stay within the object. This is constrained by the gyroradius (or Lamour radius):

$$r_g = \frac{\gamma mc^2}{qeB}. \quad (2.5)$$

It has to be smaller than the physical size of the accelerator. Here, m , q and γ are mass, charge and Lorentz factor of the particle, c the speed of light and B the strength of the magnetic field. Therefore, the maximum energy E_{\max} depends on the charge of the particle Ze , the velocity βc , the magnetic field B , and the size L of the accelerator (Hillas, 1984):

$$E_{\max} = Ze\beta cBL. \quad (2.6)$$

Following this argument, heavier ions can be accelerated to higher energies by the same source, which is consistent with an expected change in abundances at energies above 1×10^{15} eV.

Based on Hillas (1984), a plot can be created in which the strength of the magnetic field of different sources is plotted over their size. Since the maximum energy reach in sources only depends on these two parameters, a line can be drawn for specific energies and mass of the ion. This is done in figure 2.4 for a proton with 1×10^{20} eV, and 1×10^{21} eV respectively as well as for iron with an energy of 1×10^{20} eV. Sources that lie above the corresponding line can produce particles with these energies. SNRs lie well below all

three lines. They are prime candidates for the bulk of Galactic CR from GeV to PeV in energy. This observation is consistent with the change in shape of the CR spectrum at the first "knee". Energies of 1×10^{15} eV can be reached in SNRs.

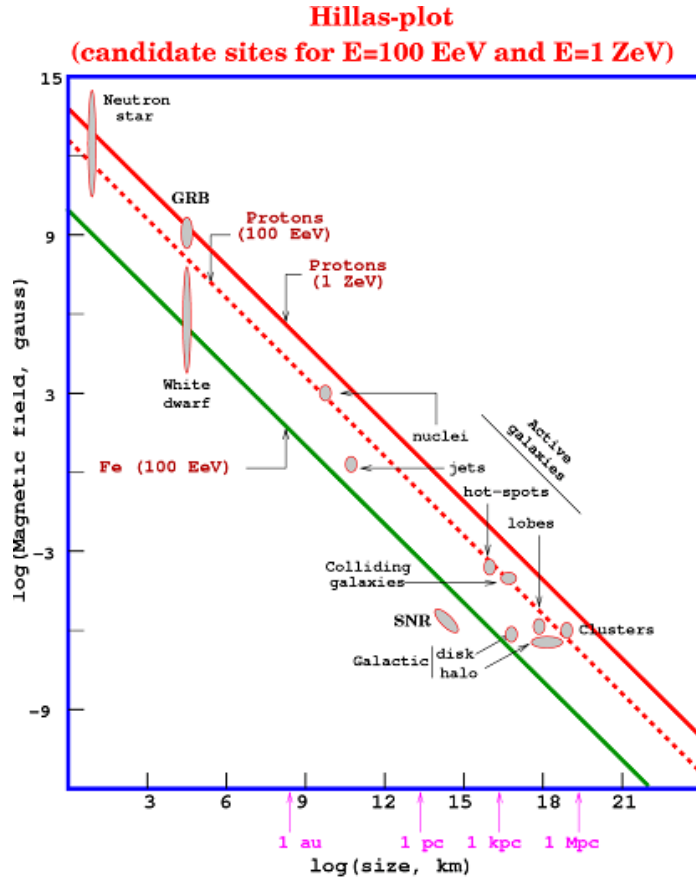


Figure 2.4: Accelerators in the context of maximum energy: The plot shows the size and strength of the magnetic fields for a number of astrophysical sources. This is put into context to the maximum energy reach by an accelerator following Hillas (1984) (see also equation 2.6). The lines show the constraints to accelerate a proton to 1×10^{20} eV, and 1×10^{21} eV respectively and for iron to reach an energy of 1×10^{20} eV. Sources that lie above these lines can accelerate particles to this energy. The plot is taken from Frascchetti (2008).

For CRs with the highest energies the probable origin lies in active galactic nuclei, clusters of galaxies and GRBs (Longair, 2011). Detecting γ -rays from GRBs with H.E.S.S. is one key science topic of the experiment. The observation program is discussed in section 4.8 in the context of the optical properties of CT5 in the fast tracking mode including exceeding the elevation limit of 90° .

2.2 Measuring the Origin of Cosmic Rays and an Introduction to γ -ray Emission Processes

Cosmic rays consist of charged particles, mainly protons and heavier nuclei, but also electrons and positrons. The Galactic magnetic field, although weak, deflects the particles on their way to Earth. Therefore, when observing CRs, the origin remains unknown, however a lot of conclusions can be drawn on the spectrum and composition. One exception are CRs above 1×10^{19} eV for which the deflection should be small. A search for anisotropy and a correlation with active Galactic nuclei (AGN) was done by the *Pierre Auger observatory* with no evidence of either to be found (Aab et al., 2015). Whether this is related to the fact that the deflection is stronger, that more sources are actually reaching energies of this order or whether the statistics is too low, is unclear. With Pierre Auger observatory being already the largest ground based detector for CR, a new space approach was investigated since the 1990s and led to the JEM-EUSO mission (Adams et al., 2015; Gottschall, 2013). Apart from a homogeneous exposure over the entire sky, the space approach also offers an exposure for CR at extreme energies that is several times larger compared to the existing ground based experiments.

Another channel of observation are neutrino detectors like IceCube (Aartsen et al., 2016). The decay of charged pions produced in the interaction of very energetic protons produces neutrinos with extreme energies. See for example Schüssler et al. (2017). A search for electromagnetic counterparts for high energy neutrinos with H.E.S.S. is ongoing.

With the detection of gravitational waves in 2015 (Abbott et al., 2016), a new window for astrophysics has been opened. The first event measured was a black hole merger without a detected electromagnetic counterpart, but it only took another two years for the detection of a neutron star merger, coinciding with the detection of a GRB by the *Fermi* and *Integral* satellites (Goldstein et al., 2017; Savchenko et al., 2017), and afterglows in various wavebands (Abbott et al., 2017). Although the H.E.S.S. experiment was the first observatory on Earth that observed the final position of the neutron star merger, the event was not detected in the energy range of H.E.S.S. Neutron star mergers are possible sources of CRs with the highest observed energies. The precise measurements of the masses and the orbit before the merger and the mass of the final object together with a potential detection of TeV γ -ray would help to test and constrain the acceleration models for Ultra High Energy Cosmic Rays (UHECRs) in neutron star mergers.

Another possibility to observe the acceleration site is to search for high energy and very high energy γ -rays, since CRs produce γ -rays at the acceleration site via inverse

Compton scattering, Bremsstrahlung or neutral pion decay. This is discussed in the following sections.

2.2.1 Emission Mechanisms

The accelerated CRs undergo cooling through a number of processes in which the particles lose energy, and some of which lead to the production of VHE γ -rays. Therefore, a population of high energy CRs is observable in the VHE regime (Longair, 2011).

For leptonic particles, the dominant cooling processes producing VHE γ -rays are Bremsstrahlung, synchrotron radiation, and inverse Compton scattering, whereas for hadronic particles, VHE γ -rays are produced in the decay of neutral pions produced from collisions of CRs.

2.2.1.1 Bremsstrahlung

An electron accelerated or decelerated by an electrostatic field of an atomic nucleus produces electromagnetic radiation. Since it is usually a deceleration in which the electron loses energy towards the radiations, this process is called Bremsstrahlung. Above a critical energy of $E \approx 250$ MeV in hydrogen gas, this process becomes dominant over energy losses by ionization. For typical environments Bremsstrahlung is relevant for high energy (HE) γ -ray production up to GeV energies, but at VHE the process is dominated by inverse Compton scattering (Longair, 2011).

2.2.1.2 Synchrotron Radiation

An electron moving relativistically in a magnetic field is subject to a force perpendicular to the field lines, which induces a circular movement around these lines. The circular movement is connected to an acceleration which is emitting linearly polarized electromagnetic radiation in the plane of motion. The lifetime of electrons losing energy through synchrotron radiation is much shorter than the lifetime of astrophysical objects emitting this kind of radiation, for example the Crab Nebula. The average energy loss rate is given by:

$$-\left(\frac{dE}{dt}\right) = \frac{4}{3}\sigma_{\text{T}}cU_{\text{mag}}\left(\frac{v^2}{c^2}\right)\gamma^2, \quad (2.7)$$

with the Thompson cross section σ_T , the speed of light c , the energy density of the ambient magnetic field $U_{\text{mag}} = B^2/2\mu_0$ and the Lorentz factor of the electron γ . Therefore, the lifetime of electrons losing energy by synchrotron radiation highly depends on the strength of the magnetic field B :

$$t_S = \frac{E}{-dE/dt} \propto B^{-2}E^{-1} \quad (2.8)$$

Therefore, in pulsar wind nebula (PWN) a continuous acceleration of particles needs to take place (Longair, 2011). The energy of the radiation depends on the strength of the magnetic field and on the energy of the electron. For a magnetic field of $5 \mu\text{G}$ and an electron with 100 TeV , synchrotron radiation of 1 keV is produced (Aharonian et al., 1997). Synchrotron emission is mentioned here because it is a relevant cooling process for electrons producing VHE γ -rays, therefore happening at the same time, and the emission is accessible through observations in other energy bands.

2.2.1.3 Inverse Compton Scattering

The process of a photon scattered by an electron, where the wavelength of the photon is much smaller than the size of an atom, is called Compton scattering. In that process the photon loses energy which the electron gains. Inverse Compton scattering is the inverse process where an electron scatters with a photon and the photon gains energy. In astrophysical objects this is the case when electrons with very high energies scatter with the ambient photon field which can also be the CMB. In the process the photons can gain energy up to a level that makes them VHE γ -rays. The relevant total cross section is given by:

$$\sigma_{\text{IC}} = \frac{3\sigma_T}{8\epsilon} \left[\left(1 - \frac{2(\epsilon+1)}{\epsilon^2} \right) \ln(2\epsilon+1) + \frac{1}{2} + \frac{4}{\epsilon} - \frac{1}{2(2\epsilon+1)^2} \right], \quad (2.9)$$

where $\epsilon = \frac{h\nu}{m_e c^2}$ and $m_e c^2$ is the energy of the electron in its rest frame (Aharonian et al., 2013).

Two approximations can be made, first for non-relativistic energies ($\epsilon \ll 1$), where the photon energy $h\nu$ is much smaller than the electron rest mass energy. In this case the inverse compton cross section approaches the Thomson cross section.

Here, the second, highly relativistic case is more relevant. The energy transfer is no longer continuous, but the electron loses a significant part of its energy with one interaction. The cross section can be approximated for $\epsilon \gg 1$ to

$$\sigma_{\text{IC}} \approx \frac{3}{8} \sigma_{\text{T}} \frac{\ln(4\epsilon)}{\epsilon}. \quad (2.10)$$

This approximation is called Klein-Nishina regime (Longair, 2011).

Assuming mono energetic 100 TeV electrons and the CMB as the target photon field, the resulting photons have an energy of 30 TeV, well inside the VHE γ -ray energy range (Aharonian et al., 1997). From this example and the example in Sect. 2.2.1.2 it becomes clear that both processes, synchrotron emission and inverse compton scattering, are happening in parallel. The ratio in flux of synchrotron and inverse compton photons depends on the magnetic field:

$$\frac{F_{\text{IC}}}{F_{\text{S}}} \simeq 0.1 B^{-2} (10^{-5} \text{G}). \quad (2.11)$$

For VHE γ -ray sources whose emission is dominated by inverse Compton emission, a synchrotron emission component is expected at lower energies. For this work, a direct implication is the search for MWL counterparts at lower energies for the detected SNR candidates (see chapter 5). Nevertheless, the emission of a potential counterpart could also be dominated by other emission processes.

2.2.1.4 Neutral Pion Decay

Neutral pions mainly decay to two γ -rays:

$$\pi_0 \rightarrow \gamma + \gamma \quad (2.12)$$

The lifetime of this process is very short (8.4×10^{-17} s). Pions are produced by interaction of hadronic particles, like proton-proton collisions. For the production of neutral pions a minimum kinetic energy of $E_{\text{thres}} \approx 300$ MeV is necessary. In addition, charged pions are also produced, but they decay dominantly into neutrinos and muons via weak interaction. Therefore, the lifetime for charged pions is larger. The rest mass of the neutral pion is $135 \text{ MeV}/c^2$ which is also the energy budget of the result photons, but the accelerated relativistically moving protons create energetically moving neutral pions. The resulting γ -rays are in the VHE regime if the energy of the underlying particle distribution is sufficient (Kelner et al., 2006).

This process is characterized by two features compared to the leptonic case. First, in the rest frame of the pion, the energies of the photons are well defined and then washed out by the direction of the photons. Hence, if the hadronic case is the dominating

emission process, the so called "pion bump" is visible in the spectral energy distribution at the GeV to TeV range (Ackermann et al., 2013). Secondly, since the cooling via collision takes longer than leptonic cooling via synchrotron emission or inverse Compton scattering, this emission can still take place although the accelerator itself is no longer active. The protons can also diffuse into the interstellar medium (ISM) and can interact with molecular clouds (Aharonian et al., 2008c).

2.2.2 Summary

Understanding the production of CRs has many important implications on understanding properties of different source classes. It also helps to understand the fundamental measurement of CR flux on Earth. From the measurement of CRs, only limited conclusions on the origin of the particles can be drawn because the direction information of CRs is lost. One method to study accelerators of CRs is via electromagnetic emission produced by the CRs at the production site. This is achieved by instruments sensitive in the GeV to TeV range like H.E.S.S. and is described in more detail in the next chapter. Being able to distinguish emissions from hadronic particles from leptonic emissions is the main challenge in the interpretation of VHE γ -rays. At these energies mainly hadrons contribute to the CR flux on Earth because leptons are cooling very efficiently on their way towards earth. Unfortunately, the VHE data alone are not very constraining due to the similar spectral features of inverse Compton emission (leptonic scenario) and emission for the decay of neutral pions (hadronic scenario). Therefore, data at TeV energies have to be studied in the context of observations at HE γ -rays to detect the signature of the "pion bump". Hence, HE refers to an energy range of MeV to GeV. A typical instrument in this range is the *Fermi-LAT* (Atwood et al., 2009). Furthermore, adding observations in the radio or X-ray band helps to identify the underlying particle population by constraining or detecting the synchrotron emission signature from the leptonic scenario. Also searching for the target material for a hadronic scenario, mainly dense gas clouds, is essential. These clouds are detected by observing line emission in the radio band.

In chapter 5 this approach is followed to investigate potential SNR candidates, the prime candidates for producing the bulk of Galactic CRs. The sources are identified as SNR candidates in the VHE band, but studied in great detail also at other wavelengths.

3 The Imaging Atmospheric Cherenkov Technique

3.1 Introduction

Imaging Atmospheric Cherenkov Telescopes (IACTs) are instruments used to observe extended air showers generated by primary energetic particles. Although IACTs are used to study cosmic rays as well, their primary goal is γ -ray observations in the energy range from tens of GeV to tens of TeV. The atmosphere is only transparent to optical light and in the radio band. In other wavebands, for example in X-rays, formerly rockets and balloons were used, and later satellites (Santangelo & Madonia, 2014; Arnaud et al., 2011). The atmosphere is not the only problem when trying to observe VHE photons directly on ground, also the flux is very low. According to DSA (Sect. 2.1.2.1) the number of produced CRs is dropping with a power of -2 to -3 . Therefore, the flux of γ -rays is dropping as well. The limited collection area of satellites puts a limit to the achievable exposure to γ -rays at GeV to TeV energies. In 1958 Jelley proposed to study CRs and γ -rays from the Cherenkov light produced by extended air showers (EASs) which in turn are induced by primary particles or photons. In this case, the atmosphere itself is the active detector medium. It took a long time to be able to detect an astrophysical source with this method of observation. The first detected source with high confidence was the Crab Nebula observed by the Whipple 10 m telescope in 1989 (Weekes et al., 1989). For a brief history of the field see Mirzoyan (2014). Over the next 28 years many discoveries were made using this technique. In the following section an overview of the physical processes relevant for the detection method and the detector principle are given with a focus on H.E.S.S.

3.2 Extended Air Showers

When a CR or a γ -ray with energies larger than a few GeV enters the atmosphere of the Earth, an EAS is created. Such a shower consists of a cascade of particles that collide, scatter and decay. These showers appear in two different forms, depending on

the primary particle. A so called hadronic shower is initiated by a charged hadron, in most cases a proton. An electromagnetic shower is initiated by a lepton or a photon. Hadronic showers are dominant and their arrival directions are isotropically distributed whereas electromagnetic showers can reveal details about their sources if the primary particle is a photon. The next two sections present a summary of how these showers start and develop (Longair, 2011).

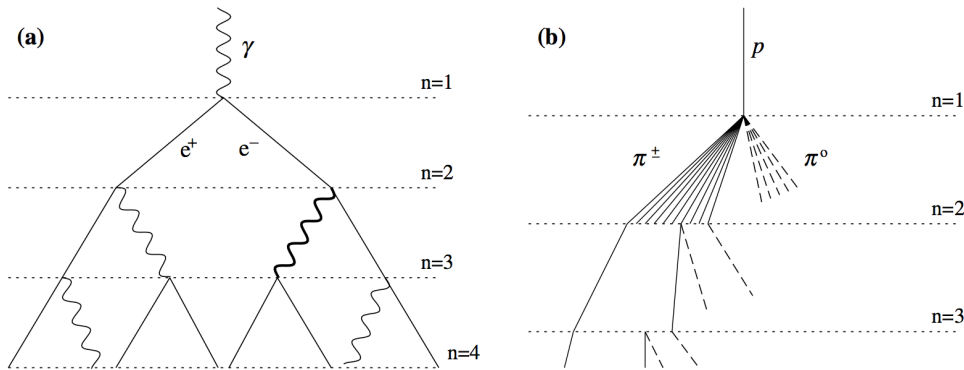


Figure 3.1: Extended air shower development according to the Heitler model: **(a)** Electromagnetic shower in which positrons and electrons are produced via pair-production which emit photons due to Bremsstrahlung. **(b)** Hadronic shower in which pions are produced that decay fast and produce electromagnetic sub showers. The plot is not to scale and is taken from Matthews (2005).

3.2.1 Electromagnetic Showers

The primary particles of electromagnetic showers are leptons or photons. Showers from these two primaries mainly differ in the height of the first interaction. The main processes involved in the shower development are pair-production and Bremsstrahlung, whereas ionization is playing a minor role. Nowadays, all known and relevant processes are included in simulations of air showers, but before the necessary computing power became available, a simple model was developed by Heitler (1954). This model predicts the basic parameters of the EASs very well. The model is presented here. In the electrostatic field of a nucleus, a pair of electrons and positrons is produced as long as the photon energy is at minimum greater than the rest mass energy of the particles produced. These secondary particles undergo Bremsstrahlung due to the Coulomb field of the nuclei in the atmosphere and produce a photon in the process. Fig. 3.1 **(a)** shows a schematic view of such an electromagnetic shower.

The energy loss due to Bremsstrahlung is proportional to the energy of the particle. Thus, a radiation length X_0 is defined as the distance on which the energy of the

electron is reduced by $\frac{1}{e}$. Using the radiation length, the energy of the shower as a function of depth x can be described as:

$$E(x) = E_0 e^{-\frac{x}{X_0}}. \quad (3.1)$$

For electrons the radiation length for Bremsstrahlung emission is $X_0 \sim 37 - 38 \text{ g cm}^{-2}$. The length of the energy loss due to Bremsstrahlung depends on the density of the atmosphere, since interactions take place in the Coulomb field of a nucleus. Therefore, the density of the atmosphere is taken into account for the radiation length and the unit is g cm^{-2} . At sea level, the radiation length of electrons is roughly equivalent to 300 m. The photons generated by Bremsstrahlung are emitted in a cone with an opening angle of:

$$\langle \theta \rangle = \frac{1}{\gamma} = \frac{\mu c^2}{E}, \quad (3.2)$$

with μ being the particle mass. The process is dominated by electrons and positrons because Bremsstrahlung is inversely proportional to the squared mass of the particle. The interaction length for pair production is $X_{0,\gamma} = 9/7 X_0$ (Grieder, 2010).

The Heitler model is based on three assumptions: First, only pair production and Bremsstrahlung are contributing to the shower; second, the interaction length for pair production $X_{0,\gamma}$ is equal to the radiation length X_0 ; and third, the energy is distributed evenly among the secondary particles at each step (Matthews, 2005). The first interaction typically takes place at 10 km to 20 km above sea level. Due to particle productions, the shower becomes longer in the longitudinal direction and because of scattering and particle decay with a transverse component, the lateral extent grows as well. The size of the shower depends on the initial energy of the particle, the incident angle, and the height of the first interaction. The maximum of the shower X_{max} is measured from the top of the atmosphere in g cm^{-2} . In the Heitler model an interaction is taking place once per X_0 (Fig. 3.1). For the number of particles after a distance x this leads to:

$$N_x = 2^{\frac{x}{X_0}}. \quad (3.3)$$

Accordingly, the energy of each particle produced at a step is:

$$E(x) = E_0 2^{-\frac{x}{X_0}}. \quad (3.4)$$

The critical energy for this process E_c is reached when the energy losses for Bremsstrahlung and ionization are equal. This happens at $E \sim 85$ MeV. The depth of the shower maximum is given by:

$$X_{\max} = \frac{\ln E_0/E_c}{\ln 2} X_0. \quad (3.5)$$

In summary, for an electromagnetic shower a particle cascade of positrons and electrons is formed close to the trajectory of the primary particle. These charged particles produce Cherenkov radiation (c.f. 3.2.3). A simulation of a 300 GeV photon shower is shown in 3.2.

3.2.2 Hadronic Showers

Photons and leptonic particles are only responsible for a very small fraction of all EAS. Most showers are induced by hadronic CRs rather than VHE γ -rays. An experiment sensitive to the detection of electromagnetic EAS will also detect hadronic showers. The vast number of these showers in comparison to the desired electromagnetic ones, and the fact that their arrival direction is isotropic, imply that these showers are a significant background component that needs to be discarded or rejected. To distinguish the showers from each other, one can exploit the intrinsic differences in the shower development.

When a hadronic shower starts to develop, the interaction is dominated by strong interactions between the primary particle and atmospheric nuclei. Mesons (mostly pions and kaons) are a significant portion of the secondary products (Fig. 3.1). The charged pions decay into muons which later on decay into electrons or positrons and neutrinos. The neutral pions decay into γ photons on much shorter timescales. Typically, late in the development of the shower, electromagnetic processes are dominant, but because of the transverse momentum of the secondary particles produced earlier, these showers are very extended (Longair, 2011). On the other hand, electromagnetic showers show a lateral spread mostly due to Coulomb scattering. Therefore, electromagnetic showers are much more concentrated around the shower axis, whereas hadronic showers show a more complex and much wider distribution of particles. The larger width of the overall shower and the more prominent fluctuations and subshowers within hadronic showers are the features used to distinguish between electromagnetic showers induced by VHE γ -rays and electrons and hadronic showers (c.f. 3.3.9). Figure 3.2 shows a comparison between a shower induced by a 300 GeV γ -ray and a 1 TeV proton from Monte Carlo simulations.

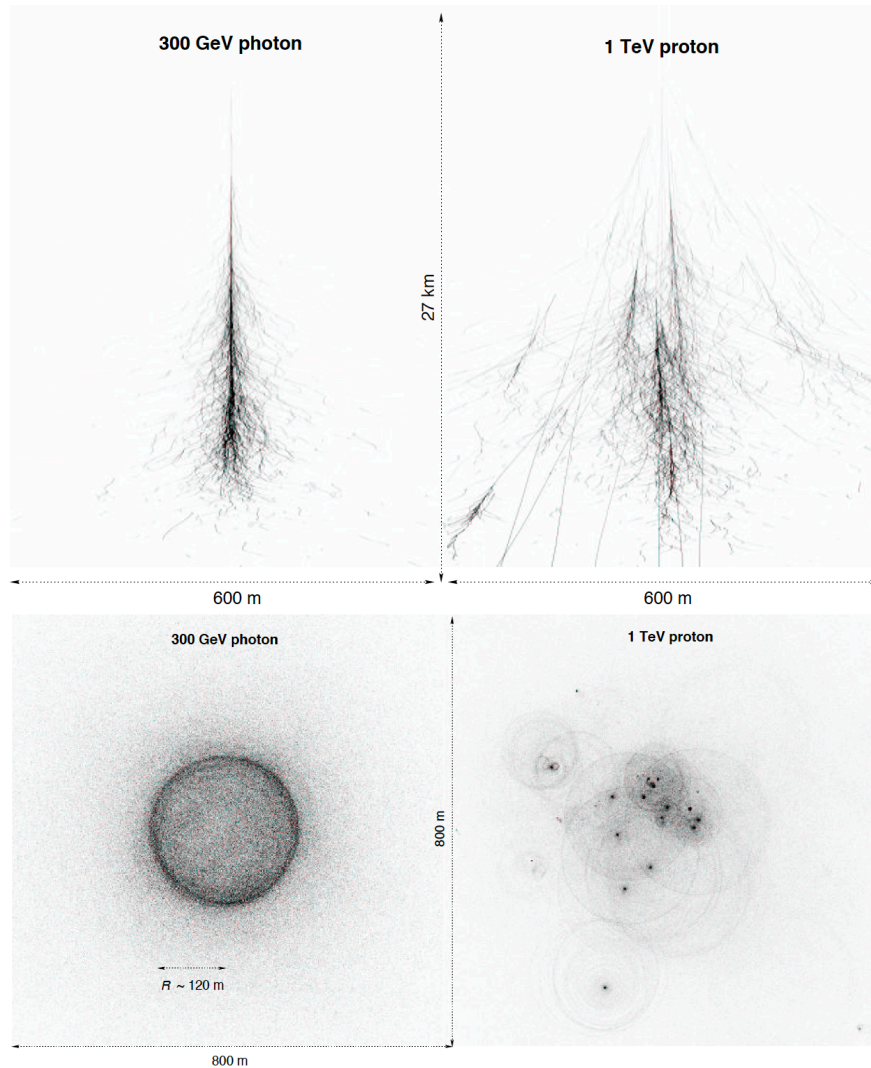


Figure 3.2: Example of electromagnetic (left) and hadronic (right) shower: On the left, a simulation of a 300 GeV primary γ -ray interacting with the atmosphere is shown. The Cherenkov light emitting electrons and positrons are concentrated in the shower axis. The plot on the bottom shows the light pool on ground at roughly 2000 m above sea level. On the right, a simulation of a proton with 1 TeV is shown. The hadronic shower consists of several subshowers and has a larger lateral spread. Figure taken from Funk (2005), based on simulations from Bernlöhner (<http://www.mpi-hd.mpg.de/hfm/~bernlöhr/HESS/>).

3.2.3 The Emission of Cherenkov Light

Charged particles moving through a dielectric medium like the atmosphere, polarize the molecules on their path. A dipole field in the medium is formed around the charged particle. When the particle moves on, the medium relaxes and, in the process, dipole

transitions occur emitting light. When the velocity of the particle v is smaller than the phase velocity in the medium c_a , the radiation produced on the particle's track interferes destructively. For a velocity larger than the phase velocity in the medium ($v > c_a$), according to Hygen's construction, the radiation will add coherently along the particle track with an angle of Θ_C (see figure 3.3). This radiation is called Cherenkov radiation. The effect is named after Pavel Cherenkov who measured the effect first and was awarded the Nobel Prize for his discovery together with Il'ja Frank and Igor Tamm who found an explanation for the radiation².

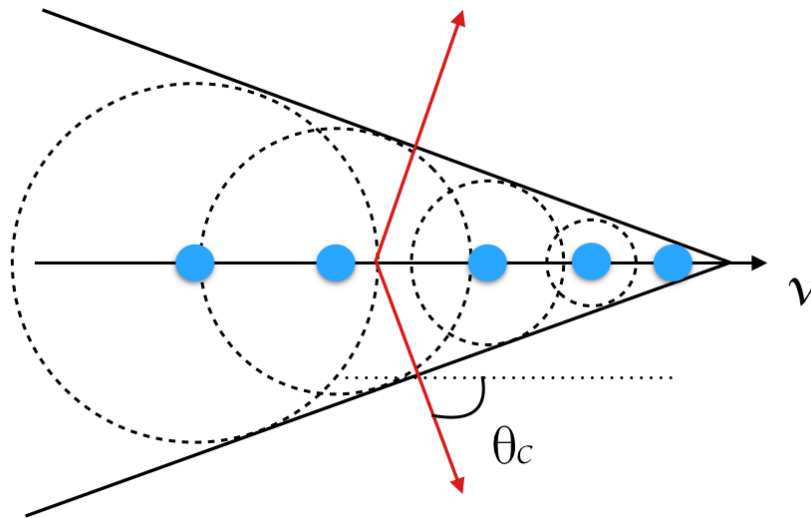


Figure 3.3: Schematic view of the production of Cherenkov radiation: The particle is moving through the atmosphere with the velocity v causing fundamental spherical light waves. If the velocity v is larger than the phase velocity in the medium c_a , the case that is shown here, the waves form a coherent wave front which moves outwards at c_a . The cosine of the angle Θ_C is given by the ratio of c_a and v . Plot taken from Mitchell (2016).

The secondary particles of an EAS move relativistically with $v > c_a$. Each individual charged particle produces Cherenkov radiation which, collectively, leads to a light cone along the particle's trajectory. The opening angle of the cone is given by the velocity of the particle v , the speed of light c , and the refractive index n :

$$\cos \theta_C = \frac{c}{vn}. \quad (3.6)$$

The duration of such a shower on ground is only a few nanoseconds. The critical energy is given by:

²http://www.nobelprize.org/nobel_prizes/physics/laureates/1958/

$$E_{\min} = \gamma_{\min} m_0 c^2 = \frac{m_0 c^2}{\sqrt{1 - n^{-2}}}. \quad (3.7)$$

Since, apart from the refractive index, this value is defined by the rest mass of the particle m_0 , light particles dominate the Cherenkov radiation (Longair, 2011). The number of produced photons depends on the traveled distance and as a function of wavelength λ is given by the Frank-Tamm formula:

$$\frac{d^2 N}{dx d\lambda} = 2\pi\alpha Z^2 \lambda^{-2} \left(1 - \frac{1}{\beta^2 n^2(\lambda)} \right). \quad (3.8)$$

Following the wavelength dependency of this formula, the peak of Cherenkov emission typically occurs at shorter wavelengths. The atmosphere is opaque to light below 300 nm. Hence, the Cherenkov light spectrum peaks close to optical wavelengths in the ultraviolet (UV).

The total Cherenkov light pool of an electromagnetic shower is the sum of the individual particles. The refractive index of the atmosphere changes depending on the density. The index as a function height h is given by:

$$n(h) = 1 + n_0 e^{\frac{-h}{h_0}} \quad (3.9)$$

with $n_0 = 0.00029$ and $h_0 = 7250$ m. The resulting index at sea level is 1.00029. The short duration of the shower leads to a light pool formed like a ring on ground. The extent of the light pool depends on the height of the interaction and the refractive index. A primary particle of 300 GeV forms a ring with a radius of ~ 120 m (see figure 3.2). The ring is filled with a reasonable flat distribution and some residual light can be seen outside the ring. A telescope placed inside the light pool is able to detect the shower (Grieder, 2010).

3.2.4 Summary of Extended Air Showers

The Cherenkov radiation produced in EASs is used to detect the arrival direction and energy of γ -rays by various experiments, using an imaging technique. This technique faces three main challenges that need to be addressed:

- On longer timescales the amount of light produced in an EAS is very small compared to the night sky background light.
- The duration of a shower is of the order of 10 ns.

- Hadronic showers are an order of magnitude more frequent than showers induced by γ -rays

To collect the light of EASs, a reflector with a diameter of a few meters up to 28 m is used in current IACT experiments. The telescope utilizes an imaging optics like the Davies-Cotton optics, used in the H.E.S.S. experiment for the 12 m telescopes. The light is focused onto a fast-imaging camera. The optics of H.E.S.S. is shown in section 3.3.3.

The focal plane cameras are equipped with detectors amplifying the incident light, for example by using photomultiplier tubes (PMTs) and are read out very fast. The H.E.S.S. cameras are operated with a sampling rate of 1 GHz (see section 3.3.4). The internal trigger logic filters out events fulfilling specific trigger thresholds and sums the data over the duration of a shower to achieve a reasonable data rate. The trigger system of H.E.S.S. is presented in section 3.3.5. The fast read-out and short duration of the shower enables the systems to differentiate EASs from the night sky background (NSB).

To discriminate between electromagnetic showers and hadronic showers, intrinsic properties of the showers are used. For a camera with a sufficiently high resolution, the larger lateral spread of hadronic showers compared to electromagnetic showers is used. The applied methods range from simple parameterization over the application of neural networks to a template based fitting procedure. The methods used by the H.E.S.S. collaboration are presented in section 3.3.9.

3.2.4.1 Current Experiments

The history of TeV γ -ray astronomy started with the detection of the Crab Nebula with the Whipple 10 m telescope in 1989 and continued with the second generation of experiments, most notable the experiment High-Energy-Gamma-Ray Astronomy (HEGRA) among others. Today the third generation of experiments is operated. The most successful ones are the Major Atmospheric Gamma Imaging Cherenkov Telescopes (MAGIC), the Very Energetic Radiation Imaging Telescope Array System (VERITAS) and the H.E.S.S.. These experiments are sensitive in an energy range from tens of GeV to tens of TeV and can detect sources with a flux of 1% of the flux of the Crab Nebula in a reasonable amount of time (Mirzoyan, 2014). All of these are arrays of two or more telescopes.

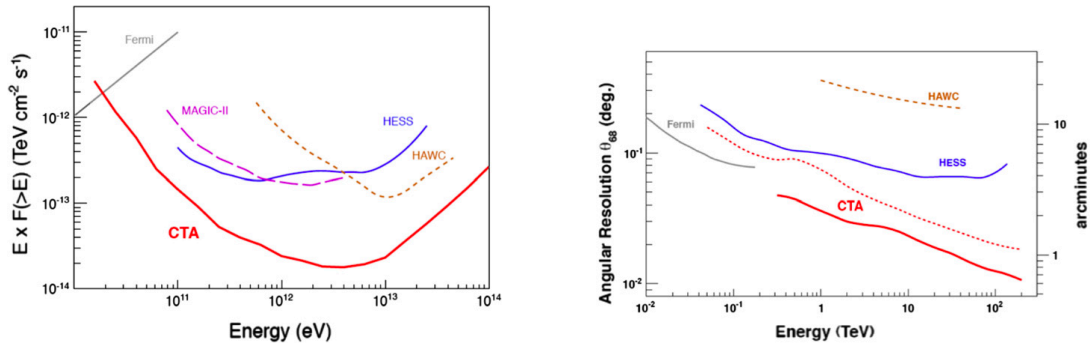


Figure 3.4: Sensitivity and angular resolution of existing experiments and CTA: On the left the sensitivity of existing IACTs (for 50 h), *Fermi-LAT* and HAWC (1 yr) is shown. On the right the angular resolution is plotted, the dashed red line shows the resolution for CTA for events from two telescopes (Acharya et al., 2013).

3.2.4.2 The Cherenkov Telescope Array

Currently, an international consortium is developing the major future system for VHE γ -ray astronomy using IACTs. The project is in its prototype phase. The goal of the project is an increased angular resolution and sensitivity of the order of a magnitude over the existing experiments. Figure 3.4 shows the sensitivity and angular resolution of the future system compared to the existing experiments MAGIC and H.E.S.S., the *Fermi-LAT* (Atwood et al., 2009) and HAWC, a system of water tanks at high altitude (Abeysekara et al., 2017). Secondary particles of EAS produce Cherenkov radiation in the water tanks with a higher refractive index.

The improved energy range of the Cherenkov Telescope Array (CTA) is achieved by utilizing three different telescope types, each one sensitive to a different energy range. The large sized telescopes (LSTs) are most sensitive at a few hundred GeV, the medium sized telescopes (MSTs) are most sensitive at around 1 TeV and the small sized telescopes (SSTs) around 5 TeV. The improved angular resolution and sensitivity will be achieved by a large number of telescopes. In total 8 LSTs, 40 MSTs and 70 SSTs are planned. The observatory will be split into two sites, a northern site on La Palma and a southern site in Chile (Acharya et al., 2013).

3.3 The High Energy Stereoscopic System (H.E.S.S.)

The H.E.S.S. is an array of five IACTs in the Khomas Highlands of Namibia. It is named after Victor Hess. In its first phase, consisting of four identical telescopes with a dish diameter of 12 m, H.E.S.S. started observations in 2003. These telescopes are



Figure 3.5: H.E.S.S. phase II at night (Image credit: Matthias Lorentz).

called CT1-4. In 2012 H.E.S.S. went to the second phase with the inauguration of a fifth telescope in the center of the existing array called CT5. Its dish diameter is 28 m which leads to a lower energy threshold and an improved sensitivity at low energies. The construction of this telescope was motivated by its projected capability to bridge the gap to satellite data, a wider energy range of the full array to probe spectral features, and the much higher sensitivity on transient phenomena at low energies compared to existing γ -ray satellites (Aharonian et al., 2006b; Holler et al., 2015; Hoischen et al., 2017). A key feature of the telescope is a fast repointing which is addressed in sections 3.3.2 and 4.8.

In this work results from the first phase of H.E.S.S. are presented exploiting a deep data set with a high sensitivity above a few hundred GeV and an excellent angular resolution (see chapter 5). In addition, the mirror alignment and the resulting optical point spread function (psf) of CT5 is discussed, also in the context of prompt follow up ToO observations (see chapter 4). In chapter 6 the result of a ToO observation of a Galactic nova is presented exploiting the low energy threshold of CT5.

3.3.1 Site Location

At 1800 m above sea level H.E.S.S. is located in the Khomas Highlands of Namibia at $23^{\circ}16'18''$ S, $16^{\circ}30'00''$ E. Being on the Southern Hemisphere, the array has a unique view on the central part of the Galactic Plane under low zenith angle. Therefore, more than half of the known TeV γ -ray sources were discovered with H.E.S.S.³. Furthermore, the location within the Khomas Highland, close to the Namib desert, offers a dry climate with low cloud coverage. Another benefit is the low magnetic field strength (Aharonian et al., 2006b).

The altitude of the experiment determines the size of the Cherenkov-light pool. For a typical opening angle of $\Theta_C = 1.2^{\circ}$, the radius of the light pool at 1800 m is 120 m for a γ -ray coming from zenith. Consequently the telescopes are arranged in a square with a side length of 120 m with CT5 in the center (Bernlöhr et al., 2003). The array is therefore optimized for the possibility of all telescopes to detect light from one EAS. Also, high altitudes reduce the atmospheric absorption of Cherenkov light. An altitude of around 2000 m offers a good trade-off between absorption and telescope separation for the stereoscopic reconstruction.

3.3.2 Telescope Structure and Drive System

The structure of the telescopes is made of steel. This reduces dish deformations dependent over the elevation angle. The mounting is an altitude-azimuth system holding the dish on two elevation towers. The entire structure is moved in azimuth on rails.

The performance of the drive system differs between CT1-CT4 and CT5. CT1-CT4 move with a velocity of $100^{\circ} \text{min}^{-1}$ both in altitude and azimuth. The range of the elevation drive is limited to an angle of almost 90° for observations and only for maintenance the telescopes can move to 180° (Bernlöhr et al., 2003).

The drive system of CT5 achieves a slewing speed of $200^{\circ} \text{min}^{-1}$ in azimuth and $100^{\circ} \text{min}^{-1}$ in elevation (Deil et al., 2008). Furthermore, the telescope can exceed an elevation angle of 90° . In case of a ToO which requires a fast followup like GRBs, this special mode can reduce the time to target significantly. CT5 can reach every position in the sky from any position in less than 100 s (Hofverberg et al., 2013; Hoischen et al., 2017).

³<http://tevcat.uchicago.edu>

3.3.3 Mirror System

The telescopes of H.E.S.S. phase I feature a large reflector dish which focuses the light onto the PMT-camera. As for all IACTs in operation, the reflector dish is the support structure for mirror segments. In the case of CT1-CT4 381 round, spherical mirrors with a diameter of 60 cm each are used with a resulting mirror area of 107 m^2 per telescope. The optics is a Davis-Cotton optics with a focal length of 15 m (Gottschall et al., 2015).

CT5 is considerably larger with a reflector dish of $23\text{ m} \times 33\text{ m}$ hosting 876 hexagonal mirror segments. From edge to edge the mirror segments have a size of 90 cm resulting in a mirror area of 614 m^2 . The hexagon shape was chosen because the gaps between individual mirror segments could be minimal. The mirrors are spherical, the dish is parabolic (H.E.S.S. Collaboration, 2017).

All mirror segments are adjustable, for details see chapter 4. The design optical psf for both telescope types is 0.03° (0.53 mrad).

The coating of the mirrors must provide a good reflectivity in the UV to blue range of above 80%. Simple aluminumized glass would provide this property, but the coating is very sensitive to mechanical wear. Considering that the telescopes are placed close to the desert without protection the coating is therefore protected with a thin layer of silizium-oxide. Nevertheless, degradation of the mirror coating is a major source of reduced optical efficiency of the telescopes over time.

3.3.4 Photomultiplier Tube Camera

The fast readout and the amplification of the faint Cherenkov light signal are achieved with cameras comprised of PMTs and Winston cones to collect the light and funnel it to the PMT. PMTs consist of a photon sensitive layer of a material with loosely bound electrons. Via photo effect, these electrons are set free by an incident photon and are accelerated by a succession of several dynodes with increasing high voltage. The pixels are grouped in eight pixels with one front-end card. Two front-end cards are one drawer. The drawers are controlled by a back-end crate inside the camera. At the anode the signal is amplified and read out in a high- and low-gain channel.

The cameras of CT1-4 consist of 960 pixels with a total field of view of 5° (Aharonian et al., 2004). The camera of CT5 hosts 2048 pixels⁴ which adds up to a field of view of 3.2° . Both cameras are operated at a sampling rate of 1 GHz (Bolmont et al., 2014).

⁴<https://www.mpi-hd.mpg.de/hfm/HESS/>

3.3.5 The Trigger System

The resulting data rate from the cameras using a continuous read-out is too high to be handled by the back-end crate or the data acquisition. Therefore, a trigger scheme is in place to reduce the data rate. The first level trigger criteria is met when an individual pixel reaches an adjustable threshold (e.g., 4 pe) and a sector consisting of 64 neighboring pixels reaches another adjustable threshold of pixels reaching the pixel threshold (e.g., 3), all within 1.5 ns. After one sector triggers, a trigger signal is created. For CT5, if the read-out chain is ready, the event is read out immediately. One event consists of the sum over 16 ns around the trigger time. The resulting rate of events is 1000 Hz to 2000 Hz. For CT1-4, a trigger signal is created in the camera and sent to the control building using optical fibers. The signals of all four telescopes are evaluated and if a trigger was sent from at least two telescopes at the same time (within 80 ns), the entire array is read out (Funk et al., 2004). Events from CT5 only are called monoscopic events whereas the events with a trigger of at least two telescopes are called stereoscopic events. The resulting event rate of stereoscopic events including CT1-5 is a few hundred hertz.

The original cameras of CT1-4 had a dead time fraction of roughly 10% using the standard trigger criteria. In August 2016 the cameras were upgraded with new front- and back-end electronics which reduced the dead-time significantly and improved the reliability of the cameras. Now, the entire array including CT5 is operated almost dead-time free (Klepser et al., 2017).

3.3.6 Calibration

3.3.6.1 Camera Calibration

An in depth description of the camera calibration can be found in Aharonian et al. (2004). Here, the basic concept of how to calibrate the cameras is described. The read-out is divided into a high gain and low gain channel. For the final intensity of the high gain channel A^{HG} , the individual pedestal of the pixel P^{HG} , the gain of the high gain γ_e^{ADC} , and a flat-field coefficient FF are taken into account. With the gain the pedestal corrected analog-to-digital converter (ADC) counts are converted to the physical unit of photo-electrons (pe). The flat-field is of the order of one and corrects an inhomogeneous response of the camera. The final amplitude is calculated as:

$$A^{\text{HG}} = \frac{ADC^{\text{HG}} - P^{\text{HG}}}{\gamma_e^{\text{ADC}}} \times FF. \quad (3.10)$$

ADC^{HG} is the measured number of ADC counts in the high gain channel. To determine the final amplitude of the low gain channel A^{LG} from the measured ADC counts ADC^{LG} , the amplification ratio of the two channels HG/LG is used:

$$A^{LG} = \frac{ADC^{LG} - P^{HG}}{\gamma_e^{ADC}} \times (HG/LG) \times FF. \quad (3.11)$$

The electronic noise of each channel is measured with so called pedestal runs. The camera is triggered by software while the lid is closed and the high voltage is active. The pedestal for an observation run P is derived from the data of the observation run every few thousand events. In a distribution of intensities the baseline peak is visible and can be fitted. From the difference between the pedestal measured with closed lid and the pedestal measured in an observation run, the NSB rate is determined.

The gain γ_e^{ADC} is derived from single photoelectron calibration runs. The cameras are illuminated with a light-emitting diode (LED) flasher which generates a signal of 1 pe per pixel in average. A histogram of number of entries per ADC count is fitted to derive the conversion from ADC count to pe.

To derive the flat-field coefficient FF , the camera is illuminated homogeneously with the LED flasher at intensities higher than for the gain measurement. By taking the ratio of the measured intensity to the average intensity in the camera, a correction factor for each individual pixel is calculated. Single photoelectron runs and flat-field runs are taken every two to three nights.

The ratio of high and low gain HG/LG is derived from observation runs. For the same event both ADC values are available. The linear region of the high and low gain overlap. From such events in the overlap region, the ratio can be calculated directly by just taking the ratio of the raw ADC counts.

3.3.6.2 Pointing Calibration

An exact knowledge of the pointing position has a direct impact on the precision of the direction reconstruction of an EAS. Although the telescopes' tracking systems are precise on a level of a few arcsec, the pointing of the optical system depends on deformations of the dish and also on the precision of the rails. To improve the accuracy, a pointing model depending on the telescope's position is created. Each telescope is equipped with two charge-coupled device (CCD) cameras with lenses, one observing the sky and the other one observing the lid of the PMT camera. LEDs on the PMT camera lid are used to determine the exact center of the PMT camera. For the standard

pointing model, the telescopes point to stars distributed evenly over the sky and both the lid and sky CCD are taking images. The star light is focused onto the closed PMT lid. The deviations between the center of gravity of the spot from the star and the camera center determined by the position of the LEDs are measured. A model containing the different sources of a miss-pointing (camera rotation, azimuth and elevation offset, dish bending, etc.) is fitted. The result are crosschecked with the sky CCD as part of the normal calibration procedure. The star positions are measured and compared with the nominal ones. Another possible crosscheck is to compare star catalogs with the position of stars in the field of view during an observation run. The stars are visible in the PMT camera through higher NSB rates (Braun, 2007).

3.3.6.3 Optical Efficiency

The optical efficiency of the entire telescope system, starting from the quality of the mirrors over the effectiveness of the Winston cones funneling the light onto the PMTs to the quantum efficiency of the PMTs themselves, plays an important role, especially since these parameters are not stable over time due to aging. The efficiency of the PMTs can be corrected by adjusting the high voltage so that the nominal gain is reached. The other parameters need to be measured to be taken into account in the simulations of the effective area.

Some of the recorded events during an observation run contain muons. They are produced in hadronic showers by the decay of pions and kaons. Relativistic muons produce a Cherenkov light cone and they reach the ground before they decay. When the muon passes through the reflective dish, a circular event is recorded in the camera (for the Cherenkov light of the muon's light cone, see Figure 3.6). The opening angle of the light cone is directly dependent on the muon's energy. Hence, the number of Cherenkov photons is known as is the measured light in the camera. Therefore, the efficiency of the telescope can be calculated. The method also works for partial rings when the muon is not hitting the telescope face on. Muons are present at a rate of about 1.5 Hz. The muon efficiency is derived from observation runs.

The optical efficiency is an important parameter for the simulations of the instrument response (see section 3.3.7). Since the phases in which one set of simulations is valid extends over several months while the optical efficiency is degrading, a correction factor is derived from the observation runs to correct variations within one calibration phase (Bolz, 2004; Mitchell et al., 2016).

3.3.7 Monte Carlo Simulations

Monte Carlo simulations serve two purposes within the H.E.S.S. experiment. First, to develop, test and verify new techniques ranging from hardware changes over event reconstruction and γ /hadron separation techniques to high level analysis techniques. Second, to simulate the response of the instrument. To simulate the shower development and the production of Cherenkov light, for example the Cosmic Ray Simulations for Cosmic Ray Simulations for the Karlsruhe Shower Core and Array Detector (CORSIKA) software package is used (Heck et al., 1998). The Cherenkov light output from CORSIKA is then used as an input for an instrument simulation. The software suite *sim_telarray*, originally developed for HEGRA, is completely flexible in the instrument's setup that is simulated. It covers the full chain of events from the Cherenkov light to a final data product as it is measured by the actual instrument. It includes accurate models of the reflective dish including mirror facet mispointing, surface roughness, individual reflectivity of the mirror facet and shadowing of the camera and the camera masts. The geometry of the camera is included as well as the response of the camera hardware (Bernlöhr, 2008). A specific H.E.S.S. version is available within the collaboration (*sim_hessarray*). It is preconfigured for the H.E.S.S. array, contains all relevant instrument parameters and is compatible with the H.E.S.S. data format. Monte Carlo simulations are produced to fill look-up tables for the event reconstruction. These simulations are redone as needed to account for major changes on the array's configuration, for example a mirror exchange.

3.3.8 Quality Selection

The quality selection serves two purposes. First, runs that are highly affected by hardware problems or bad weather are filtered out. Second, especially for the energy reconstruction of the events, the condition of the instrument should not differ too much from the nominal condition used in the Monte Carlo simulations. This also includes the quality of the atmosphere. For a set of parameters a cut is used to filter out runs. The cuts are applied on run duration, number of broken pixels, stability of the trigger rate and the transparency coefficient of the atmosphere (Aharonian et al., 2006b; Hahn et al., 2014). The cuts have been verified using simulations and real data. A study on the impact of the run quality on the results of the analysis for CT5 is ongoing. Preliminary results show that the parameters from H.E.S.S. phase I do not need to be changed.

3.3.9 Event Reconstruction

3.3.9.1 Image Cleaning

To clean the images from NSB fluctuations, hot pixels from stars or hardware problems, a two level cleaning is applied. Standard values are for example 10 pe and 5 pe^5 . Pixels have to be above the higher threshold and the direct neighbors have to be above the lower threshold to not be removed. Pixels below the higher threshold but above the lower threshold with at least one neighbor above the higher threshold survive the cleaning as well. The values are optimized to keep the shower information whilst removing the aforementioned unwanted signal (Aharonian et al., 2006b).

3.3.9.2 Hillas Reconstruction

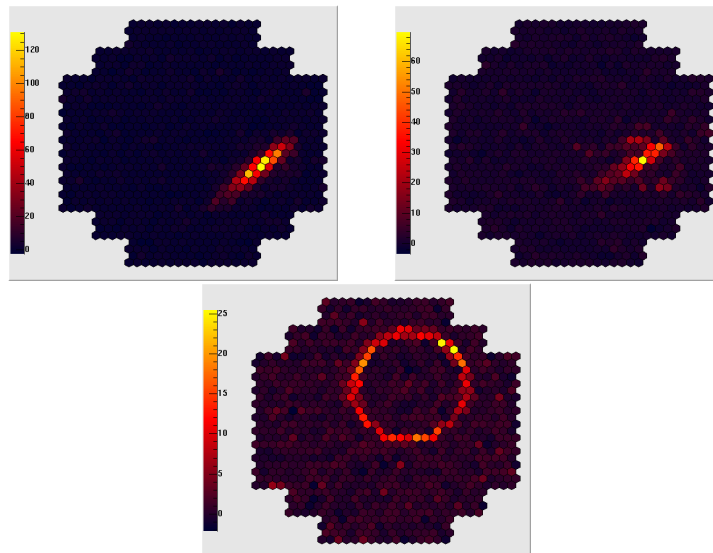


Figure 3.6: Events recorded by the first H.E.S.S. telescope: On the left an electromagnetic shower, probably from a photon, is shown. In the center a hadronic event is shown, identifiable by the more irregular and broader light distribution caused by sub showers. On the right a muon that passed through the reflector is shown (Image taken from <https://www.mpi-hd.mpg.de/hfm/HESS/pages/about/telescopes/>).

After image cleaning the standard procedure includes shower parameterisation using Hillas parameters which in turn are used for γ /hadron separation and direction reconstruction (Hillas, 1985; Aharonian et al., 2006b). Even though more sensitive methods are available now, this technique is well understood and provides robust results. Therefore it is still in use. As it is shown in figure 3.6 on the left, an electromagnetic shower

⁵pe: Photo-electrons, the charge that is created in a PMT from one photo-electron

creates an elliptical image in the camera whereas hadronic showers create a more irregular and broader image due to the sub showers (as shown in the middle, see also figure 3.2). The images are approximated with an ellipse characterized by the parameters width, length, centroid of the ellipse and distance to the camera center. A cut on the distance to the camera center is applied to remove truncated images.

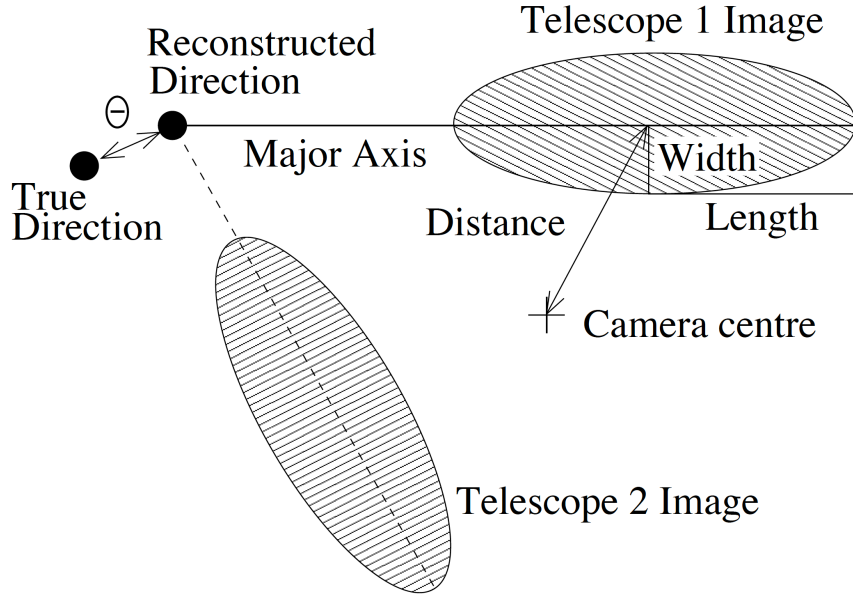


Figure 3.7: Shower parametrization following Hillas (1985): The images (see Figure 3.6 left) are approximated by ellipses. The parameters are centroid, distance to the camera center, width and length. From the intersection of the major axis of two telescope images, the reconstructed direction is derived. Θ is the distance between true and reconstructed direction (Aharonian et al., 2006b).

For stereoscopic events, a direction reconstruction is done based on information of at least two telescopes. The telescopes observe the event from different angles. The major axis of the ellipses is equivalent to the path of the primary particle for electromagnetic showers. By intersecting the major axis from the images of at least two telescope, an accurate shower reconstruction is done as well as impact parameter reconstruction, which is the center of the light pool of the shower on ground (Aharonian et al., 2006b). The method is shown in Figure 3.7. For CT5 mono events this approach is not possible. The direction is reconstructed based on the light distribution of the shower along the major axis (Murach et al., 2015).

The background is dominated by hadronic showers that have a different shower development compared to showers from γ -rays which are the desired signal. From Monte Carlo simulations lookup tables are filled with the width and length of γ -ray showers depending on the impact parameter, the image amplitude, and the zenith angle. From

the real event the zenith angle, the image amplitude and the impact parameter are taken to search for the mean width and length in the lookup tables that fit the observation parameters best. Also the root mean square (rms) of the Monte Carlo distribution is read from the lookup tables. The difference of measured width w_i to expected width $\langle w \rangle_i$ over the rms σ_i is calculated for all participating telescopes. The mean of these values is the mean reduced scaled width (MRSW):

$$MRSW = \frac{1}{N_{\text{tel}}} \sum_i^{N_{\text{tel}}} \frac{w_i - \langle w \rangle_i}{\sigma_i}. \quad (3.12)$$

The same is done for the length to derive the mean reduced scaled length (MRS�). Cutting on these values is a very powerful discriminator between γ -like events and hadrons. An example is shown in Figure 3.8. The MRSW of simulated γ -rays and protons is shown on the left together with measured background events from the H.E.S.S. experiment. The distribution of the measured events follows the simulated proton background which validates the simulations. The long tail of positive values for background events results in a very effective cut position. The one presented by Aharonian et al. (2006b) is shown as a dashed line. In the same figure on the right the measured MRSW distribution is compared to the simulated one for the Crab Nebula at 50° zenith angle.

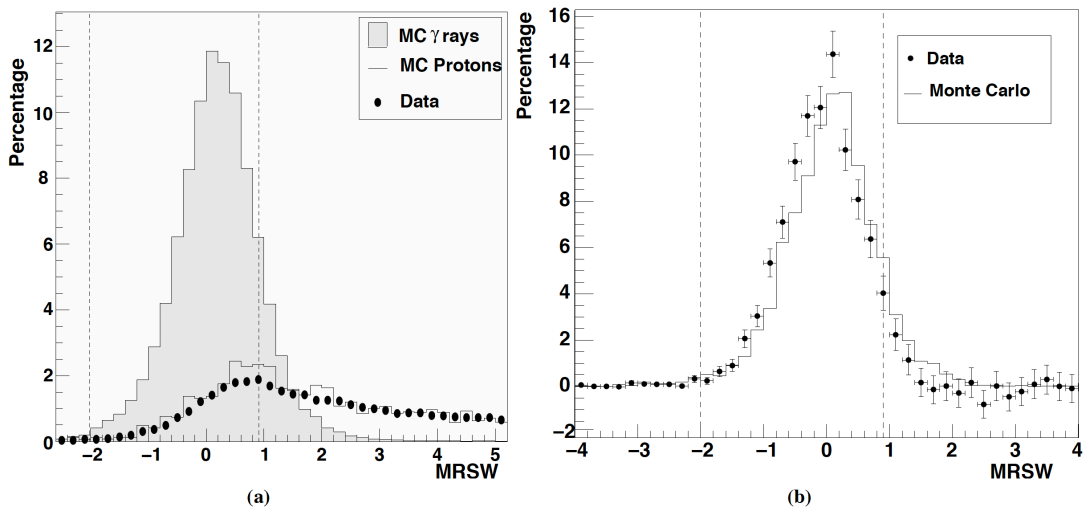


Figure 3.8: γ /hadron separation based on shower parameters: On the left, the simulated MRSW distribution for γ -rays and protons is shown together with the measured background from the H.E.S.S. experiment. Dashed lines show the cut on this parameter. On the right, the simulated MRSW distribution is shown together with the measured one for an observation of the Crab Nebula at 50° zenith angle (Aharonian et al., 2006b).

With this method a significant portion of the background events is removed. The resulting events after this cut are called γ -like events. Remaining background in this event class are hadronic events that are very similar to electromagnetic events and showers induced by leptons.

The energy reconstruction is entirely based on the zenith angle of the observation, the measured image amplitude, and distance to the camera center. The distance to the camera center is related to the distance of the shower core from the telescope, or the impact parameter. With these two values lookup tables are used that contain simulated events with known energy of the primary particle. The image amplitude directly correlates to the energy of the primary particle though this value is sensitive to the optical efficiency of the entire system. Hence, although the lookup tables are reproduced in regular intervals, the remaining difference between simulated optical efficiency and actual optical efficiency are corrected using muon events in the simulation. From the simulated and real muon events, a correction factor is calculated (Mitchell, 2016).

The methods mentioned before have been developed with previous experiments and adjusted for the use with H.E.S.S. (Aharonian et al., 2006b). Over the years some attempts were made to improve the reconstruction either partially or overall. One approach is to use a combination of shower parameters in a machine learning environment. Boosted decision trees (boosted decision trees (BDTs)) of the Toolkit for Multivariate Data Analysis with ROOT (TMVA) are trained on shower parameters from simulations. Applied on real data the γ /hadron separation power is improved significantly (Ohm et al., 2009). Another approach is a high performance likelihood reconstruction of γ -rays for imaging atmospheric Cherenkov telescopes (de Naurois & Rolland, 2009). It uses a likelihood fit of models derived from Monte Carlo simulations to real data. The likelihood of the fit is used as a discriminator between hadronic and γ -like events. A similar approach is an Image Pixel-wise fit for Atmospheric Cherenkov Telescopes (ImPACT). One important difference is that instead of using a semi-analytic approach for the model, a full set of Monte Carlo simulations plus instrument simulation is done. Also, instead of using the goodness of the fit as discriminator between γ - and hadronic events, the method from Ohm et al. (2009) is used. Relying on the goodness of the fit requires an excellent knowledge of the pixel background which mainly depends on the NSB (Parsons & Hinton, 2014). Both likelihood methods reconstruct the energy and direction simultaneously and provide an improved result compared to the standard Hillas based analysis. An issue with improved γ /hadron separation is that for an imperfect calibration the number of γ -like events drops in an uncontrolled way. For example, in case of a calibration problem, the distribution of the measured MRSW and MRSL might be shifted or changes the shape compared to the simulated distributions.

The separation power of these parameters does not break down completely. Finding the root cause of the differences is possible by looking at the calibration parameters one by one. When using derived parameters like the goodness of the fit from a likelihood reconstruction (de Naurois & Rolland, 2009), or the ζ parameter from a TMVA based γ /hadron (Ohm et al., 2009) the separation power might break down completely depending on the calibration problem because both methods highly depend on precise instrument simulations. Finding the root cause is therefore much harder compared to a Hillas reconstruction.

3.3.10 Background Estimation

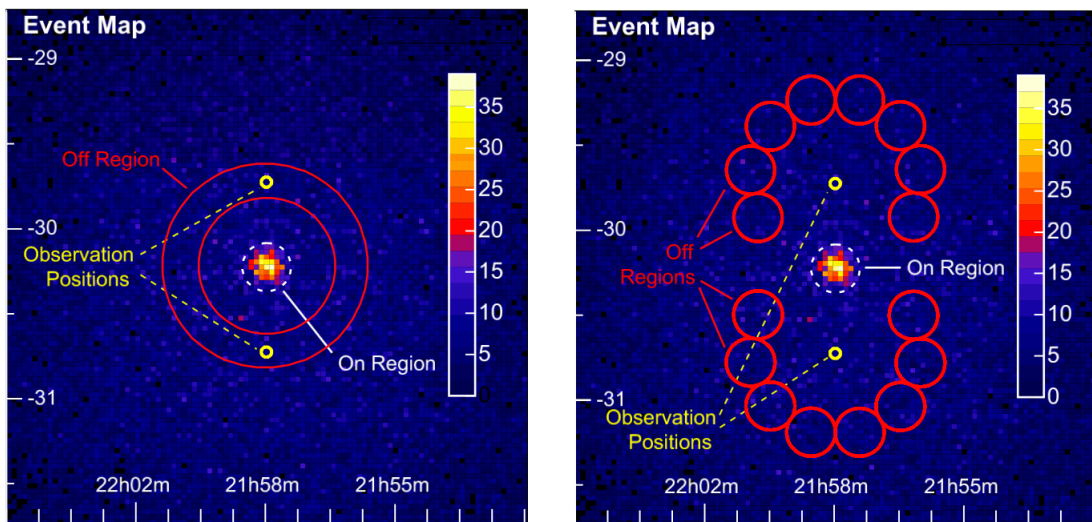


Figure 3.9: Background determination methods of H.E.S.S.: On the left the ring background method is shown. The method is applied to a γ -like map from an observation of PKS 2155–304 with H.E.S.S.. A ring is placed around the test position (ON region). The observation shown here was taken with an alternating offset of 0.5° in declination. On the right, the reflected region background estimation is shown. Around the test position (ON region) identical OFF regions with the same offset to the pointing position are placed. The array’s acceptance is to the first order radially symmetric, therefore only the number of background regions needs to be taken into account. This is the preferred method for spectral analysis. (Plots taken from: Berge et al., 2007).

After γ /hadron separation the resulting data is not background free, remaining events are sub-threshold sources in the field of view, wrongly classified hadronic events and leptonic events. Therefore, a background estimation is done with the reconstructed events after separation. An overview of the most relevant two methods is presented by Berge et al. (2007) and H.E.S.S. Collaboration (2018d).

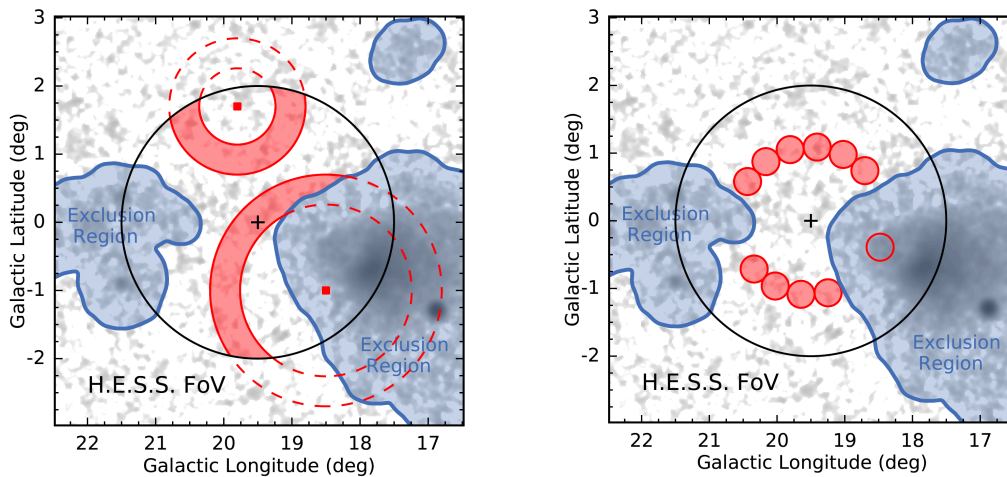


Figure 3.10: Background determination methods of H.E.S.S. with exclusion: On the left the ring background method is shown. Regions of known significant emission are masked with an exclusion region (blue). The black circle shows the field of view of the observation. For a test position (red square) the background is estimated from a ring around the test position. If the ring is overlapping with an exclusion regions, this part of the ring is not taken into account. The ring radius is adjusted to guarantee a minimum size of the background region. To create a map of γ -ray excess, the background is estimated for each pixel. The relative exposure between test position and background region needs to be taken into account. On the right, the reflected region background estimation is shown. The tested region is the open red circle. Identical regions with the same offset to the pointing position are placed excluding significant emission. (Plots taken from: H.E.S.S. Collaboration, 2018d).

The basic approach of all background methods is to compare the counts of an ON region to an OFF region as background. The basic approach with H.E.S.S. is to estimate the background from the observation runs on the targets themselves. The region of interest is observed with a pointing offset depending on the extent of the expected source (usual offset is 0.5° to 0.7°). The background is extracted from the same observation run as the signal which ensures identical instrument and weather conditions. Two specific approaches are usually used depending on the high-level analysis result (sky maps or spectra) that is derived.

Figure 3.9 shows the basic approach to estimate the background for an ON region using an observation of PKS 2155–304 with H.E.S.S. as an example. The source was observed with an alternating pointing offset of 0.5° in declination. Around the ON region a ring is placed. The ring should have a size of seven times larger than the ON region. Although under ideal conditions most acceptance differences between the different sky position cancel out, the acceptance is taken into account when determining the background.

For a realistic observation, the observation conditions (mainly zenith angle) vary and have to be taken into account. The radial acceptance is derived from extra galactic observations. AGNs are point sources and the positions are well known so they can easily be excluded. The remaining signal is filled into a histogram as a function of camera offset. This is done for different zenith bands. The distribution is fitted with a radial acceptance curve which is then used for the background determination. This method is called ring background method. An alternative method is to place regions identical to the ON region with the same offset around the observation position. To the first order the acceptance of the array is radially symmetric. Therefore, no acceptance correction has to be done. This method is called reflected region method and is the preferred method for spectral analysis.

Figure 3.10 shows the same approach including exclusion regions for arbitrary positions in the sky. The ring background method can be applied to create a map of excess events or a map of the significance of the emission. For an ON region, a ring is placed around this ON region. Typically the ring has a thickness of 0.44° and an inner radius of 0.7° . Known emission is masked in the process with exclusion regions. Parts of the OFF region overlapping with the exclusion region is not taken into account. To ensure a minimum in background exposure, the radius of the ring is increased until the acceptance of the OFF region is at least four times larger than for the ON region. A parameter α is calculated as the ratio of ON-exposure to OFF-exposure. The background is defined as α times number of OFF counts. This can either be done for a region of interest or for each pixel of a sky map. If the exclusion regions are not known a priori, they can be derived from a sky map from the ring background method in an iterative process. For the first iteration no exclusion regions are used, while in the second step all significant emission from the first step are masked with exclusion region. In all further steps the regions are refined until they are stable.

The reflected region method with exclusion regions does not differ from the method without exclusion regions apart from the fact that if a potential OFF region is overlapping with the exclusion region, it is not taken into account.

3.3.11 Performance of H.E.S.S.

The performance of H.E.S.S. varies significantly depending on the array's configuration. Four different modes are presented here:

- H.E.S.S. I or H.E.S.S. II stereo: Events from the 12 m telescopes are taken into account. The event has to be present in at least two telescopes. A stereoscopic reconstruction is done.

- H.E.S.S. II hybrid: Events from all telescopes are taken into account. The event has to be present in at least two telescopes. A stereoscopic reconstruction is done.
- H.E.S.S. II mono: Events from the 28 m telescope CT5 are taken into account. A monoscopic reconstruction is done.
- H.E.S.S. II combined: A combination of hybrid and mono reconstruction. If a hybrid reconstruction is possible, no mono reconstruction is done. Otherwise a CT5 mono reconstruction is done.

The appropriate configuration is chosen based on the available data or the source properties. Technical problems or an observation with a split array leads to data sets where only a monoscopic or stereoscopic reconstruction are possible. If the focus lies on the low energy emission of a source, a monoscopic or combined analysis is preferred. The energy threshold is lower, but the angular resolution, energy resolution and sensitivity of a monoscopic reconstruction is not as good as hybrid or stereo and the field of view is smaller.

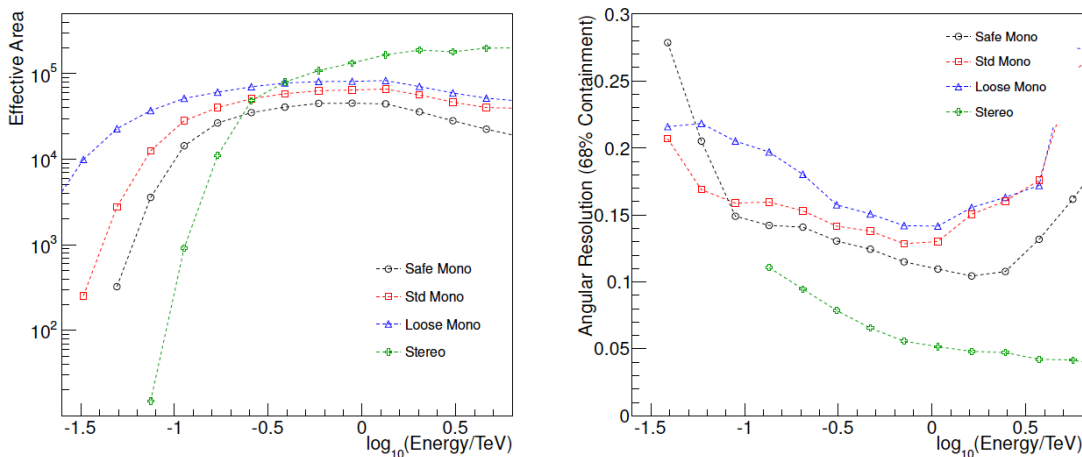


Figure 3.11: Effective area and angular resolution of H.E.S.S.: On the left the effective area as a function of energy is shown for stereoscopic reconstruction (CT1-5) and mono reconstruction (CT5) in units of m^2 for four different image amplitude cuts. The simulation was done for a zenith angle of 20° . On the right the angular resolution as a function of energy in degree is shown for the same configurations. (Plots taken from: Parsons et al., 2015b).

The effective area A_{eff} is determined from Monte Carlo simulations. It is defined as:

$$A_{\text{eff}} = \frac{N_\gamma}{N_{\gamma, \text{MC}}} A_{\text{MC}}, \quad (3.13)$$

where $N_{\gamma,MC}$ is the number of simulated photons, A_{MC} the area the photons are simulated for, and N_{γ} the number of photons that pass all analysis cuts and are reconstructed. The effective area is required to calculate a physical flux from the number of measured photons. The effective area is stored in lookup tables for the analysis. It depends on the shower energy, the offset to the center of the field of view, the zenith and azimuth angle. Figure 3.11 shows the effective area as a function of energy for a stereoscopic reconstruction and a monoscopic reconstruction using three different image amplitude cuts. As expected, the monoscopic reconstruction using only events from the 28 m telescope CT5 has a larger effective area at lower energies whereas the stereoscopic reconstruction becomes more sensitive at higher energies (Parsons et al., 2015b).

The angular resolution is the precision with which the origin of a γ -ray can be reconstructed. It is described with a γ -ray psf. To determine the psf, a point source with a given spectral energy distribution is simulated with the instrument simulation tool. The squared distance of the reconstructed position to the simulated position Θ^2 is included into a histogram. A rotational symmetric psf is assumed. Simulations have been done as part of the lookup tables for the analysis. The simulation results in the lookup tables are weighted for the assumed (or measured) spectrum of the source. The histogram filled from the lookup tables is fitted with a triple exponential analytic function:

$$\frac{dP}{d\Theta^2}(\Theta^2) = \sum_{i=1}^3 A_i \exp\left(-\frac{\Theta^2}{2\sigma_i^2}\right). \quad (3.14)$$

P is the event probability, and A_i and σ_i the weights of the different components (H.E.S.S. Collaboration, 2018d). The angular resolution is usually given as the 68% containment radius of this function in two dimensions. The angular resolution is energy dependent because the direction reconstruction of events with higher energy is more precise due to the larger extent of the shower images. This is true until the events are truncated or saturate the camera. The precision also depends on the reconstruction technique. The angular resolution of a monoscopic reconstruction is worse by a factor of a few. Figure 3.11 on the right shows a comparison of the angular reconstruction as a function of energy between a monoscopic reconstruction for three different image amplitude cuts and a stereoscopic reconstruction (Parsons et al., 2015b).

Effective area and angular resolution are two important performance parameters. The third topic to discuss is the energy resolution and energy threshold of the array. Like the direction reconstruction, the energy reconstruction is not perfect. Therefore, a difference in reconstructed energy to true energy over the true energy is derived from Monte Carlo simulations:

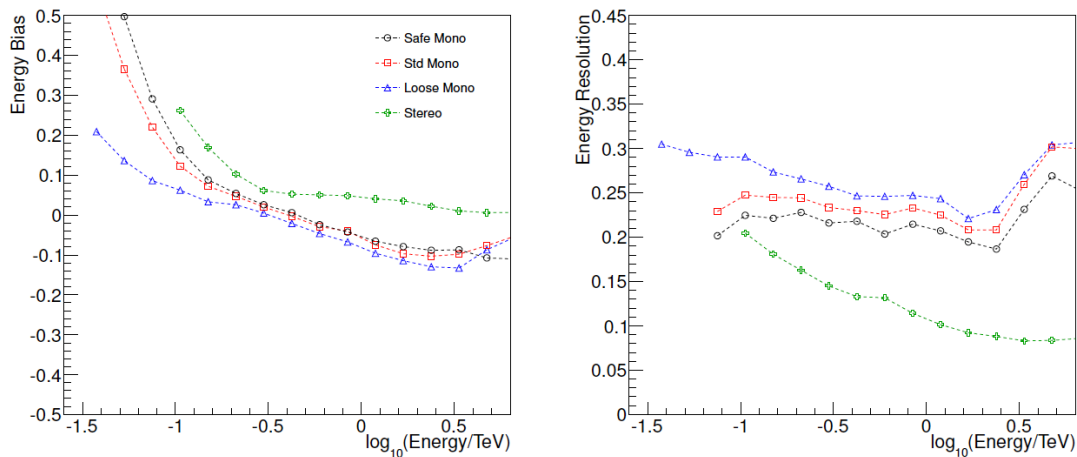


Figure 3.12: Energy bias and energy resolution of H.E.S.S.: On the left the energy bias as a function of energy is shown for stereoscopic reconstruction and mono reconstruction for four different image amplitude cuts. On the right the energy resolution as a function of energy is shown for the same configuration. (Plots taken from: Parsons et al., 2015b).

$$\Delta E = \frac{E_r - E_t}{E_t} \quad (3.15)$$

For a large enough sample of simulations, the distribution of ΔE for a given energy can be well fitted with a Gaussian function. The resulting width is defined as the energy resolution (Aharonian et al., 2006b). At low energies the system tends to record and reconstruct showers that are brighter than the mean of showers at a given energy. Consequently, the mean of ΔE is shifted to positive values. At the highest energies the inverse happens. Bright and therefore close showers saturate the cameras or the events are truncated. A bias to dimmer showers at a given energy is present which shifts mean of ΔE to negative values. The effect is called energy bias and specifies the threshold of a given observation. The energy threshold as used in the presented analysis is defined as the energy at which the energy bias in the simulation is 10% or larger. Figure 3.12 shows the energy bias and energy resolution at low energies for stereoscopic and monoscopic reconstruction. The energy resolution of the stereoscopic reconstruction is superior and becomes better with rising energy. On the other hand, CT5 mono has a superior energy threshold as shown on the left (Parsons et al., 2015b). Figure 3.13 shows the energy threshold for the full energy of the stereoscopic reconstruction on the left and the evolution of the energy threshold versus the zenith angle. The energy threshold rises as a function of zenith angle as expected since the light from the shower has to pass through more atmosphere to reach the telescopes (Aharonian et al., 2006b).

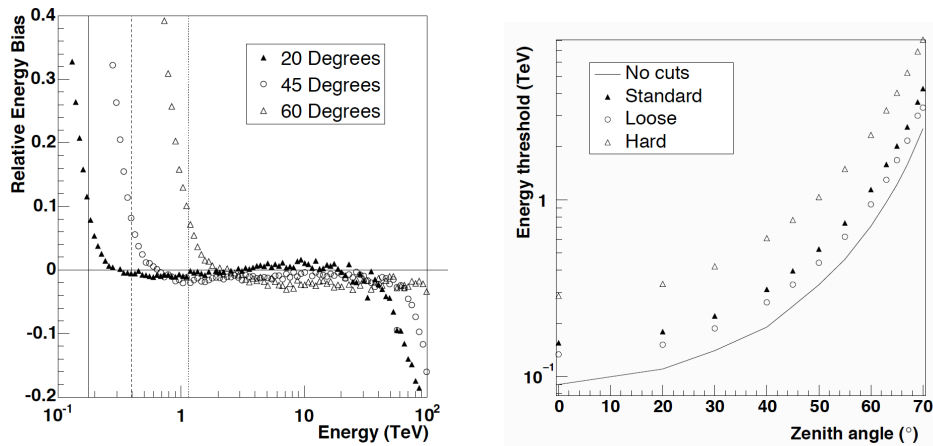


Figure 3.13: Energy bias and energy threshold of H.E.S.S. for different zenith angles: On the left the energy bias as a function of energy is shown for a standard stereoscopic reconstruction (CT1-4) for different zenith angles. The dotted lines indicate the lower safe energy threshold. On the right the energy threshold is shown as a function of zenith angle. The values are for a stereoscopic reconstruction with no cuts and three different cut sets optimized for different sources (Plots taken from: Aharonian et al., 2006b).

From the effective area a sensitivity curve can be derived. In Figure 3.14 the sensitivity of H.E.S.S. for a 50 h observation is shown for a moderate zenith angle of 18°. On the y-axis the flux needed for a 5σ detection for a point source is plotted. The plot contains sensitivity curves for CT1-4 stereo and CT1-5 combined as defined above. The fact that CT1-4 stereo is more sensitive than CT1-5 hybrid is related to the fact that the size of the extraction region for a point source detection (also known as Θ^2 cut) is complicated to optimize for a mixed array with different angular resolution (Holler et al., 2015). An energy dependent Θ^2 cut is needed. The implementation of such a cut is an ongoing effort.

Adding the fifth telescope to the array lowered the energy threshold of the system significantly and it made the array more sensitive to sources with soft spectra. One example for the performance of H.E.S.S. in its second phase shows H.E.S.S. Collaboration (2017). In this paper a study of the blazars PKS 2155-304 and PG 1553+113 with H.E.S.S. is presented including energy spectra reaching down to below 100 GeV.

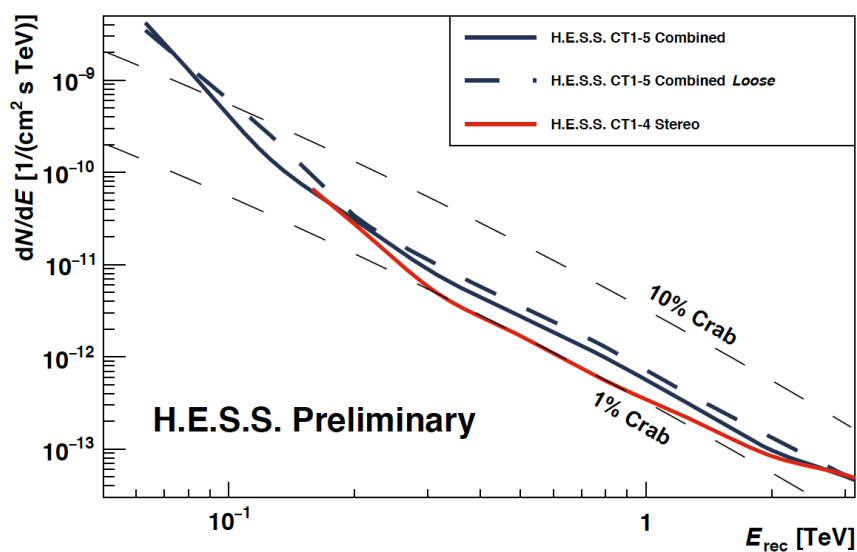


Figure 3.14: Differential sensitivity of H.E.S.S. II: The differential flux needed for a 5σ detection in a 50 h observation with a zenith angle of 18° is shown. (Plots taken from: Holler et al., 2015).

4 The Mirror Alignment and Control System for H.E.S.S. Phase II

4.1 Introduction

The reflective dishes of the two types of IACTs of H.E.S.S. consist of a large number of mirror segments. For the 12 m telescopes of H.E.S.S. phase I, CT1-4, 381 to 385 mirror segments are used, for the fifth additional telescope CT5 with a dish diameter of 28 m there are 876 segments. The challenge of such a system is the alignment of the mirror segments. The focal lengths of the telescopes of ~ 16 m for CT1-4 and ~ 36 m for CT5 require a system that can adjust the position of the mirror segments with a precision of μm . The mirror segments themselves have a spherical shape with a focal length comparable to the focal lengths of the telescopes. Details of the alignment system for the 12 m type telescope of H.E.S.S. phase I are discussed by Cornils (2006), and a more general overview of the optical system of these telescopes is found in Cornils et al. (2003).

For aligning a mirror segment the telescope is pointed to a star and it tracks this star for the duration of the alignment. The individual mirror segments create an image of the star on the lid of the PMT camera because of their spherical shape and a focal length comparable to the focal length of the telescopes. A CCD camera in the dish takes images of the PMT camera lid. By adjusting the mirror tilt, the position of the star images from one mirror segment changes on the PMT camera lid. Tilting the mirror is achieved by using two actuators per mirror. By measuring the movement of the star image with the CCD camera, a transformation matrix between actuator movement and CCD position movement is calculated and used to align the star images to the center of the PMT camera lid. In principle it would be possible to calculate the transformation matrix from the geometry of the dish, the position and optics of the CCD camera, and the parameters of the actuators. This approach would require a high precision of the parameters which can not be achieved. Figure 4.1 shows a schematic of the basic principle. This idea was described by Hofmann (1998) in an internal note first.

Aligning the star images on the PMT camera lid generates a total optical system that is best focused for stars at the position of the lid. For observations the PMT camera lids are open. The opening windows of the PMTs lie a few centimeters behind the lid. The core of EAS from γ -rays are located 10 km to 15 km away from the telescope. The PMT cameras of CT1-4 are designed so that the telescopes are focused on the typical value of the distance of the shower. For the 28 m telescope CT5 a system was installed to change the distance of the PMT camera to the dish. First, the large focal length of the telescope requires a larger shift of the PMTs compared to the alignment position to focus the telescope to the showers. Second, the distance of the showers and therefore the optimal focus position is elevation angle dependent. The so-called AutoFocus unit positions the camera to the optimal distance.

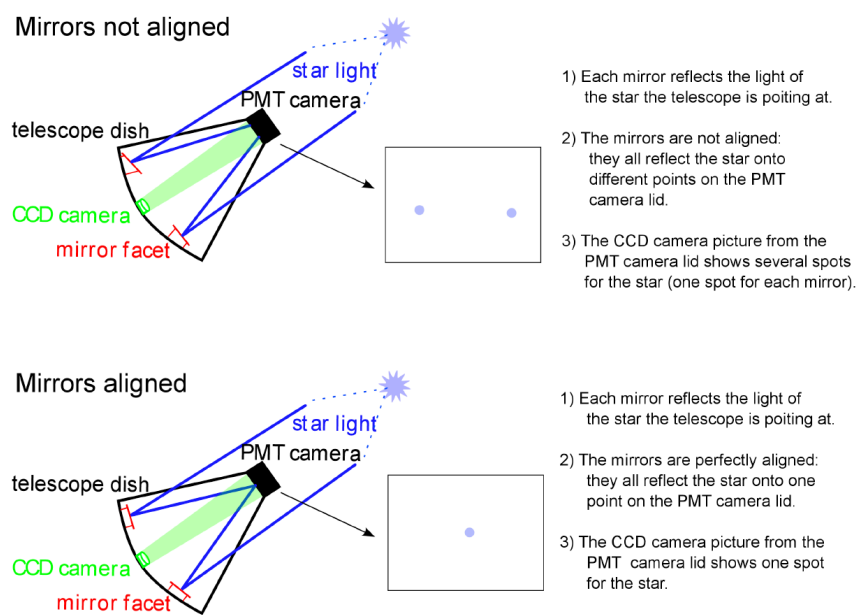


Figure 4.1: Basic principle of the mirror alignment: The telescope tracks a star. The top panel shows two unaligned mirrors, creating two images of the star on the PMT camera lid called spots. On the bottom the two mirrors are aligned to the PMT camera center creating one single spot. The CCD camera in the dish takes images for the alignment procedure and the monitoring. Image taken from Schwarzburg (2012).

For the 28 m telescope CT5 that was added for H.E.S.S. phase II, the same principle as described in Cornils (2006) is used with some improvements concerning the time needed for a full alignment to account for the higher number of mirror segments. In the following sections the components and software are discussed as well as a detailed description of the alignment procedure. As a reference Schwarzburg (2012) is used. When the work related to this thesis started, technical problems with the drive system of CT5 made a re-alignment of its mirrors necessary. Prior to that the software was

improved to speed up the alignment and to reach a higher precision in the alignment (see section 4.6). The results are discussed concerning the achieved optical point spread function, the long term stability of the system and the impact of reverse pointing on the alignment. This is a special case because the telescope exceeds zenith with the elevation drive to reduce the angular distance to a target of a ToO observation on the optical system. Figure 4.2 shows CT5 with a fully aligned dish.



Figure 4.2: Picture of CT5: The 28 m telescope CT5 with a fully aligned dish is shown in this picture. One mirror on the top right is missing for a CCD camera.

4.2 Components of the Alignment System

4.2.1 Mechanical Components

The mirror segments of CT5 have a hexagonal shape with a flat to flat size of 90 cm. The reflector dish hosts 876 mirror segments, all equipped with two actuators each and a fixed point. To interface the glass mirror and the steel structure, connecting points are glued to the backside of the mirror on which the actuator and the fixed point are screwed on. The length of the fixed point is adjustable depending on the position of the telescope. The actuators are equipped with a ball joint. The fixed point (fixed in length) is rotatable in two ball joints, together with the ball joint of one actuator the mirror can

be tilted onto one direction by moving the spindle of the actuator. Hence, the mirror is connected stress free to the telescope structure with two degrees of freedom controlled by the actuators. The actuators together with the mounting have been developed at the Max-Planck-Institut für Kernphysik (MPIK). The components are shown in Figure 4.3.

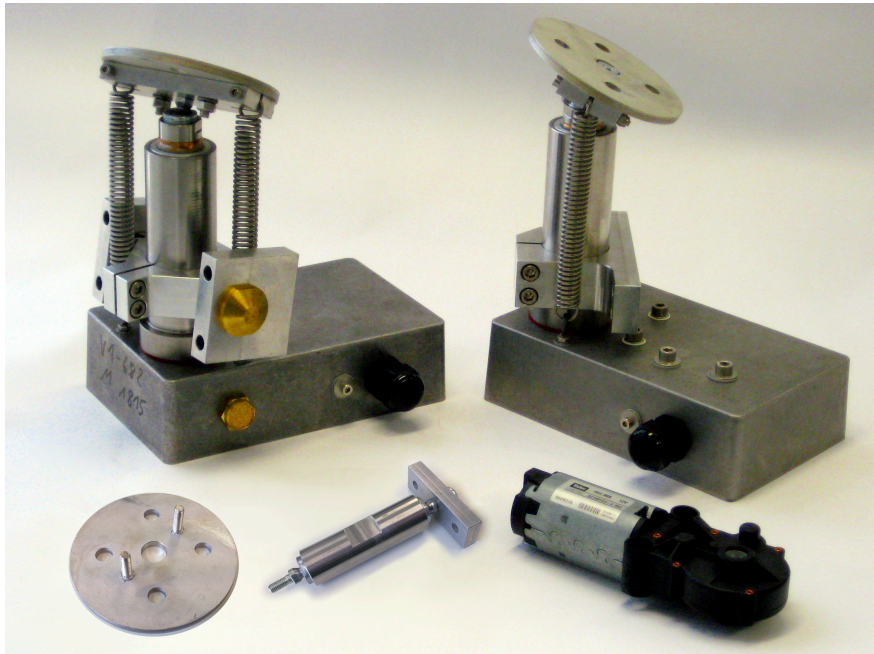


Figure 4.3: Image of the mechanical components of MACSII: Two actuators with the connection plate to the mirror are shown in the background. In the foreground the connector plate, the fixed point and a motor are shown. The motor is usually placed within the aluminum case shown at the bottom of the actuators. The image is taken from Schwarzburg (2012).

The motors driving the actuators are standard industry products with a hallsensor creating one impulse per motor turn. With this signal the motor movement is tracked. Nominally the motors are operated at 12 V with a power consumption of 600 mA to 800 mA without load, and up to 1200 mA in operation. The speed of the motor is 21 rpm. The motors are connected to the spindle of the actuator with a worm gear with a ratio of 210/1. One turn of the spindle creates 210 impulses from the hallsensor. Both the rising and falling edge of the impulse are detected, one transition is called hallcount in the following. The pitch of the thread of the spindle is 1 mm. The resulting resolution of the spindle position is therefore $2.3\ \mu\text{m}$. The mechanical play of the components is not taken into account for this accuracy calculation since it is negligible. Two springs reduce the mechanical play, they are attached to the outside of the actuator.

The range of the spindle is 40 mm. Within the case, the endpoints are secured by disk springs which leads to an increase in power consumption and time between the

Table 4.1: List of parameters of the mechanical parts of the mirror alignment system. The values are taken from Schwarzburg (2012).

Description	Value
Hallsensor pulses per spindle turn	210
Hallsensor pulse edges per spindle turn	420
Lift per spindle turn	1 mm
Lift per hallsensor edge	2.3 μm
Lever arm of the actuator movement	450 mm
Mirror tilt per hallsensor edge	0.005 mrad
Light spot movement per hallsensor edge	0.01 mrad
Pixel size of the PMT camera	1.22 mrad
Time between two hallsensor edges	1/120 s
Actuator range	40 mm
Time to drive the actuator range	120 s

hallcounts when coming close to the dead stop of the actuator range. It is by this increased power consumption that the endpoints of the actuator range are detected. Typical values of the entire actuator system relevant for the mirror movement are listed in table 4.1.

4.2.2 Electronic Components

The mirror alignment system is controlled from a computer in the control room or via a remote connection world wide. The control computer has an optical Ethernet connection to the CCD camera in the dish called LidCCD and to a central control box which hosts an Ethernet switch and a central power supply. The central box is connected to panel control boxes. For CT5, the dish is separated into 25 panels with up to 42 mirrors each (see Fig. 4.4). The panel control boxes are connected to the central box with optical Ethernet to control the hardware and with power cables, one for each box.

Each panel control box hosts a panel control board. On the panel control board a multiplexer, an ADC and a field-programmable gate array (FPGA) are located. The FPGA hosts a microcontroller which communicates with the control computer via Ethernet. It receives the commands to move actuators and returns the relative movement of the motor. The hallsensor pulses are digitized with the ADC and both rising and falling edge of the pulse are detected and counted. To move the motor, a motor control card is addressed using the multiplexer. Because of the multiplexing, only one motor per panel control box can be moved. This is sufficient for the required performance of the entire system. The signal lines and power lines of the motor control card are connected

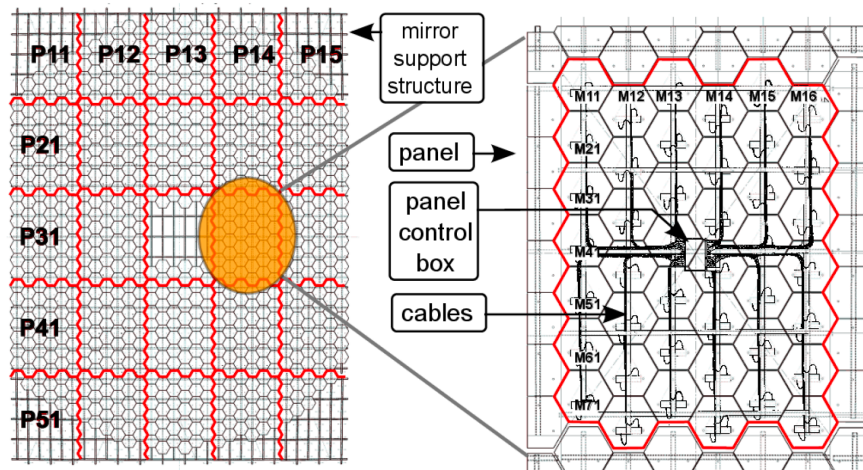


Figure 4.4: Structure of the dish of CT5: The mirror support structure is divided into 25 panels. A panel supports up to 42 mirrors. In the schematic the numbering scheme used by the alignment software and the cabling of one panel is shown. The schematic is taken from Schwarzburg (2012).

to the ADC and the power supply. Furthermore, the panel control board is monitoring the power consumption and time between hallsensor pulses to detect endpoints of the actuator or mechanical problems. For details on the firmware in the FPGA see Schwarzburg (2012). A thorough test of the hallcount detection was conducted using a highly accelerated lifetime test. Only 4 ± 5 counts are missed. The offset between commanded and actual actuator movement is 0 ± 2 (Gottschall et al., 2015).

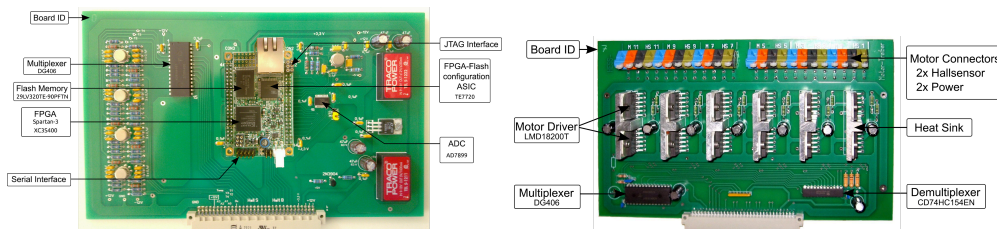


Figure 4.5: Electronic board of the alignment system: On the left the panel control board with its components is shown. On the right the motor board is shown. The images are taken from Schwarzburg (2012).

On the motor boards, motor drivers for each motor are connected. To select motors and to communicate with the panel control board, a multiplexer and demultiplexer are used. Figure 4.5 shows the panel control board. The motor board was designed by S. Vetter at the IAAT.

The mirror alignment and control system of CT1-4 is designed in a way that only one motor can be active at a given time. Since the panel control boxes can be active at the same time, the limitation for CT5 is 25 actuators at the time. This improves the

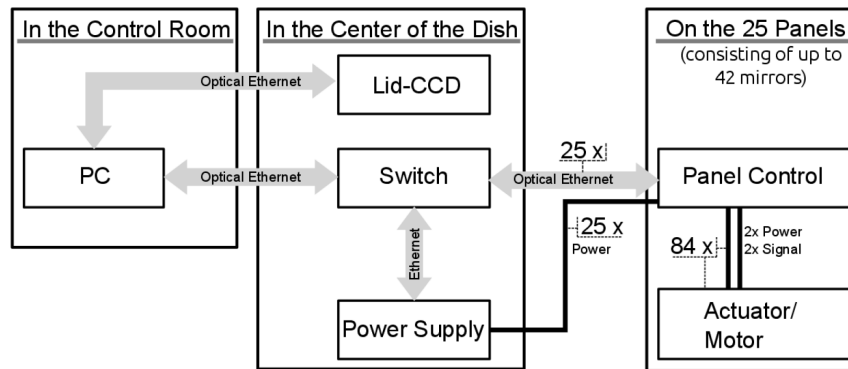


Figure 4.6: Block diagram of the alignment system: The individual components of the alignment system and their location in the telescope are shown. The schematic is taken from Schwarzburg (2012).

performance significantly compared to the system used for CT1-4. Figure 4.6 shows the structure of the system in a block diagram.

The limitation of 25 parallel motor movements of MACSII is driven by the power consumption and the number of Input/Outputs (I/Os) of the panel control board. For the alignment technique used here more parallel motor movements are not needed and a repositioning of all mirrors to another alignment position, for example from an elevation dependent lookup table, can be achieved in less than 5 min.

4.2.3 The CCD Camera

For the alignment, images from the CCD camera mounted in the dish of the telescope are necessary. The camera type used is an Apogee Alta-U32 with a 180 mm lens. One main purpose of the so called LidCCD is to provide the input for a pointing model of the telescope (see section 3.3.6.2). The camera is connected to a camera server in the dish of the telescope which provides an Ethernet interface based on TCP/IP to the central data acquisition (DAQ) and to the mirror alignment software.

4.3 Alignment Software

In this section a short introduction is given on how the software works. For a detailed description see Schwarzburg (2012).

4.3.1 Panel Control Board

In addition to the hallcount detection and the task of turning the motors on and off, the FPGA on the panel control board features a micro controller, a so called Microblaze soft processor core⁶. Due to limitations in the memory management and the overall performance, a Linux micro kernel specifically for micro controllers is used, the so called uCLinux. The kernel provides a full Transmission Control Protocol and the Internet Protocol (TCP/IP) stack. The communication to the control computer is realized by TCP/IP via Ethernet. A custom protocol is used on top to reduce the overhead of the data packets.

4.3.2 Central Control Computer

The interface to the panel control boards and to the CCD camera uses the standard TCP/IP protocol. Therefore any computer within the instruments data network can be utilized for the alignment software.

Schwarzburg (2012) listed the following tasks that have to be handled by the alignment software:

- Providing a user interface to control the alignment of the mirrors
- Implementing the alignment algorithm
- Extracting information from and storing information in the mirror database
- Communicating with the server on the panel control board
- Accessing the LidCCD camera server

The software was developed in python 2.x with dependencies for numpy, scipy, pyfits and matplotlib. The database is handled by the Django database abstraction layer. It stores the relevant information on the individual mirrors for the alignment and the details on the individual panel control boards.

Because of limited bandwidth, for example when working at the telescope from Europe, a command line interface is used to control the software. Additional information like documentation, database access, and list of available stars are available on the web server. For details on the software architecture see Schwarzburg (2012).

The following section outlines the basic alignment algorithm used for the re-alignment of the telescope.

⁶<https://www.xilinx.com/products/design-tools/microblaze.html>

4.4 The Alignment Algorithm

The main goal of the alignment algorithm is to provide a transformation from light spot movement in the CCD image to actuator movement. The final position of the light spot should be in the center of the PMT-camera.

4.4.1 Mathematical Description

The mathematical principle has been presented by Cornils (2006) for H.E.S.S. phase I. Since for CT5 the same principle is used, the description is also valid for the mirror alignment and control system for H.E.S.S. phase II (MACSII).

A linear dependency of actuator movement and spot movement is assumed. Therefore, the transformation can be written as

$$\Delta \vec{x} = T \Delta \vec{a}. \quad (4.1)$$

The position of the mirror spot in the CCD image is expressed as $\vec{x} \equiv (x_1, x_2)$ whereas the actuator position is described as $\vec{a} \equiv (a_1, a_2)$. The transformation matrix T is expressed as

$$T \equiv \begin{pmatrix} \delta x_1 / \delta a_1 & \delta x_1 / \delta a_2 \\ \delta x_2 / \delta a_1 & \delta x_2 / \delta a_2 \end{pmatrix}. \quad (4.2)$$

The mirrors have a fixed tilting axis of 120° . Therefore, two elements of the transformation matrix are dependent when using a rotation matrix R_{120} for 120° . The rotation matrix is defined as

$$R(\Theta) = \begin{bmatrix} \cos \Theta & -\sin \Theta \\ \sin \Theta & \cos \Theta \end{bmatrix}, R_{120} = \begin{bmatrix} -1/2 & -\sqrt{3}/2 \\ \sqrt{3}/2 & -1/2 \end{bmatrix}. \quad (4.3)$$

With this rotation matrix the transformation matrix can be determined by measuring the displacement of the light spot for only one of the actuators because by taking the rotation matrix into account, the following dependency reduces the problem of determining the transformation matrix:

$$\begin{pmatrix} \delta x_1 / \delta a_1 \\ \delta x_2 / \delta a_1 \end{pmatrix} \simeq R_{120} \begin{pmatrix} \delta x_1 / \delta a_2 \\ \delta x_2 / \delta a_2 \end{pmatrix} \quad (4.4)$$

Because of the shape of the telescope, the dependency is not completely linear and the precision of the angle between the tilt axis is not completely accurate. The positioning if the mirror needs to be precise on a few micrometers level, less than typical engineering tolerances. In the following section, the alignment procedure for CT5 is outlined. By splitting the alignment in a coarse alignment step using the rotation matrix and potentially extrapolating the final position and a fine alignment step determining the full transformation matrix and interpolating the final position, a high precision is achieved.

4.4.2 Alignment Procedure

The telescopes are usually observing under elevation angles larger than 35° since the energy threshold and the effective areas are elevation angle dependent (see section 3.3.11). Even larger elevation angles are common. Since the mirror support structure shows elevation dependent dish bending, the alignment of the mirrors is optimized to 65° elevation angle. As light sources, bright and isolated stars are used when their elevation is between 60° to 70° . An additional constraint is the distance to the moon of 10° to 90° . Shadows from the camera support structure or a very high noise level can complicate the alignment. A list of usable stars has been compiled by Cornils (2006).

For the duration of the alignment the telescope is tracking the star. The procedure is separated into two parts, the coarse alignment and the fine alignment.

4.4.2.1 Coarse Alignment

For the coarse alignment, the fact is exploited that measuring the displacement of only one actuator is sufficient to determine T . After mirror mounting, the individual light spots of the mirrors should be located on the PMT-camera. This is true in general, a small fraction of mirrors need manual adjustment. For the simple procedure the following steps are carried out (Cornils, 2006):

- Move all mirrors out of the field of view of the CCD camera
- Move a single mirror to the center position of both actuators so the spot is likely to be in the field of view
- Take a picture
- Tilt the mirror in one axis
- Take another picture

- Take the difference of the two pictures and run a spot finding algorithm which determines the start (negative excess) and end position (positive excess)
- Calculate the transformation matrix T using δa_1 , δx_1 and δx_2
- Move the mirror to the center of the PMT camera
- Repeat from the top with the next mirror

For details on the spot finding algorithm see Schwarzburg (2012). Standard routines of the python packages numpy and scipy are used. After a sufficient number of spots are coarsely aligned, the final position the mirrors are moved to is the center of mass of the main spot created by several mirrors, in case of CT5 20 mirrors.

This process is rather time consuming: roughly 1 min is needed for one mirror. A fast algorithm is implemented in the software by moving several mirrors at the same time in a predefined pattern to identify the mirrors simultaneously. Here the fact that the alignment system of CT5 can move up to 25 mirrors at a time compared to one mirror for the system of CT1-4 is exploited. For details see Schwarzburg (2012).

4.4.2.2 Fine Alignment

The precision of the coarse alignment is limited by the assumed rotation matrix and non-linearity effects of the translation between the spot movement in the CCD image and the actuator movement. To overcome the limitations a second step is executed. From the center position of the PMT camera a mirror is moved out slightly in all four directions. By doing so the transformation matrix is fully determined because both actuator axes are used and the final position, the PMT camera center, lies within the actuator movement. This procedure is based on Cornils (2006), but since for CT5 the orientation of the tilt axis is the same for all mirrors and several mirrors can be moved at the same time, the fine alignment step is performed for four mirrors at a time (Schwarzburg, 2012).

4.5 Results of the Initial Alignment and Interpretation

4.5.1 Results

From the experience with CT1-4, the characteristics of the mirror segments, and the mechanical design of the telescope, an expected optical psf was simulated for CT5. The optical psf depends on the quality of the mirrors, mainly the roughness of the

surface and the precision of the focal length of the individual mirror, the elevation dependent bending of the dish, and the quality of the alignment. The precision of the alignment has been estimated based on the mechanical design. To characterize the elevation dependent psf, a ray-tracing simulation was done assuming a point-like source at infinity. To characterize the psf a radius of a circle enclosing 80% of the reflected light in the simulation was derived. This parameter is called R_{80} . For the psf, *hessarray*, a H.E.S.S. specific version of *simtelarray* as described in section 3.3.7, was used. The result of the initial simulation is shown as a red curve in figure 4.7 as a function of elevation.

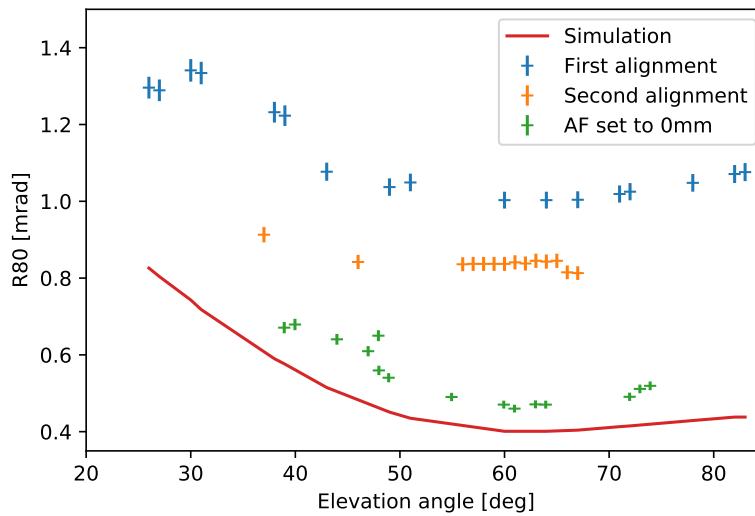


Figure 4.7: Results of the first alignment of CT5: The plot is showing the R_{80} , a measure of the optical psf of CT5, as a function of the elevation angle of the telescope. In red a simulation of the expected behavior is shown. The blue data points indicate measurements after the first alignment, the yellow data points after the second alignment. The green data points show a measurement with the correct auto focus setting.

To verify and adjust the simulation parameters, the optical psf was measured at the telescope using stars at different elevation angles. The telescope is pointing to a star, an image of the PMT-camera lid is taken and the R_{80} is derived. After the initial alignment in summer 2012 done by Schwarzburg et al., the results showed that the psf is more than twice as large as expected. The measured results are shown as blue data points in Figure 4.7. The fine alignment was repeated under better conditions (less moon illumination and a reduced star list only containing the brightest and most isolated stars), but the results were still insufficient. This is shown by the yellow data points in Figure 4.7. This was the status when this work started.

4.5.2 Interpretation

The reasons for the difference between measured and expected psf were searched for various aspects:

- The focus of the CCD camera
- The quality of the mirrors
- The assumed settings of the simulations
- The accuracy of the alignment
- The position of the auto focus unit of the PMT camera

The focus of the CCD camera was adjusted and measured several times, the camera performed as expected and could be excluded from the list. This work was done by the University of Hamburg.

The quality of the mirrors had been verified by measurements in the lab. Nevertheless, to exclude the mirrors from this list of possible errors and also to verify the simulated mirrors, a test was done. In the telescope, 16 mirrors were measured individually with a bright star and the lid-CCD camera. This was done by moving all mirrors out of the field of view of the CCD camera with MACSII except for one mirror. Using a bright star and a long exposure time, a spot of this individual mirror was recorded. The R_{80} was determined using the psf monitoring image analysis. The same mirrors were simulated individually with *simhessarray* at their same position in the telescope using the standard simulation parameters. The results are shown in table 4.2. The sample was not large enough to represent the entire telescope, but a major result was that the measured and simulated R_{80} do not differ significantly. Furthermore, the results from the individual mirror segments in the telescopes are in the range of the results of the quality measurements. Figure 4.8 shows a normalized distribution of the measured R_{80} from a mirror test setup (Giavitto, 2006). The measurements were done for 900 mirror segments for CT5 at the Institut für Astronomie und Astrophysik Tübingen (IAAT). The nominal focal distance was used for this measurement. Therefore, values identical with the measurements shown in table 4.2 are not possible, but for the mirrors from panel 33 (central panel) similar values are expected. A normal distribution was fitted to the data resulting in an R_{80} of (0.24 ± 0.08) mrad.

The values from the measurements in the telescope agree reasonably well with the simulation results of individual mirror segments. Nevertheless, the entire telescope was simulated again with parameters for the mirrors that did match the worst measurement of the mirror segments P35M46 and P24M46. The resulting R_{80} of the telescope is

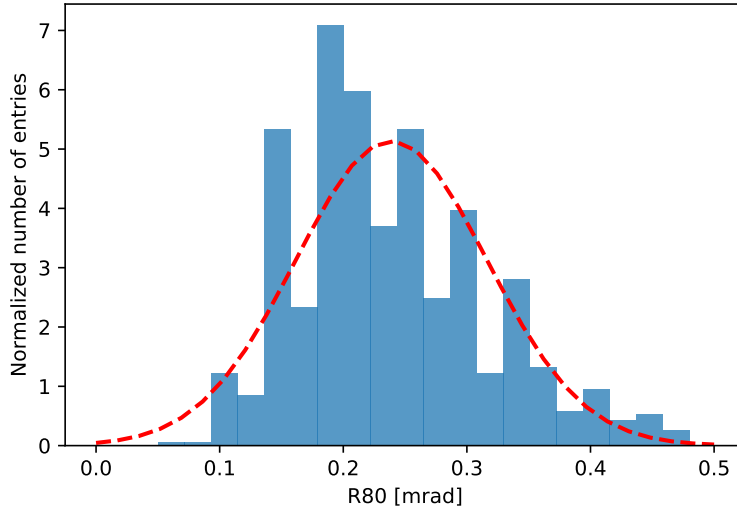


Figure 4.8: Mirror psf from quality measurements: The mirror segments of CT5 were measured in a test setup prior to the installment at the telescope. The resulting R_{80} is shown in a histogram together with a normal distribution with an R_{80} of (0.24 ± 0.08) mrad.

37.5% larger, but it could not explain a factor of two as seen in 2012. Furthermore, this was a worst case assumption to estimate the impact of the mirror parameters on the overall psf simulation.

Another possible concern was the auto focus unit of the PMT-camera. The alignment is done with a star at very large distance, whereas the air showers happen 10 km to 15 km away from the telescope. For CT5 it was foreseen that the focus should be adjusted depending on the elevation angle of the telescope. Therefore, CT5 is equipped with a system to change the focus by several centimeters. For the alignment, the system is set to 0 mm whereas for observations the value is typically 66 mm. It turned out that the auto focus unit was not correctly working for the psf measurements. However, in the log files of the auto focus system, the problem was not obvious which delayed the discovery of the problem significantly.

It is not possible to reconstruct in what setting the auto focus unit was for the first two measurements shown in figure 4.7. After the problem was discovered, reported and fixed, the measurement was repeated in the position the alignment was probably done. The measurement is shown in green. The conclusion is that the expected performance is almost reached. No formal requirement on the optical psf exists. The measured performance is well inside the range in which the impact on the air shower observations

Table 4.2: Simulated and measured psf of individual mirror segments

Mirror ID	Measured R_{80} [mrad]	Simulated R_{80} [mrad]
P33M12	0.324	0.326
P33M14	0.442	0.332
P33M16	0.385	0.335
P33M72	0.402	0.332
P33M74	0.342	0.332
P33M76	0.342	0.332
P31M41	0.314	0.379
P13M14	0.395	0.665
P35M46	0.629	0.401
P22M43	0.304	0.332
P53M73	0.420	0.579
P24M46	0.503	0.365
P42M43	0.291	0.329
P24M54	0.316	0.335

is negligible. The mirror alignment and control system for H.E.S.S. phase II performed as expected.

During further characterizations of the optical properties, a problem with the tracking system was discovered. The zero point of the azimuth axis was not calibrated correctly, but showed a small offset of a few tenths of a degree. Since the alignment was done on the camera center assuming a correct pointing, the main spot position showed a significant elevation dependency. The spot is perfectly centered for elevation angles in the range of the angles used for the alignment (60° to 70°). Depending on the difference in elevation angle, the angular distance to the star changes for a constant offset in the azimuth shaft encoder. Because of the horizontal coordinate system used, this deviation should depend on the cosine of the elevation angle. In figure 4.9 the measured deviation to the camera center in azimuth direction is shown. The elevation angle reaches 160° . The telescope can exceed zenith and point to the other direction with the elevation drive. The advantages of the so called reverse pointing is explained in section 4.8. A fit of the data points was done and they can be well described by a function that depends on the cosine of the elevation angle.

The offset of the azimuth drive was corrected which led to a constant offset of the optical axis. Furthermore, after the initial tests of the reverse pointing, the bolts holding the actuators and mirrors were checked. It was discovered that some of the bolts and screws were slightly loose. Only a marginal increase in psf size was measured after tightening, but because of this and the azimuth offset of the main spot, a new alignment of the mirrors was done as part of this work.

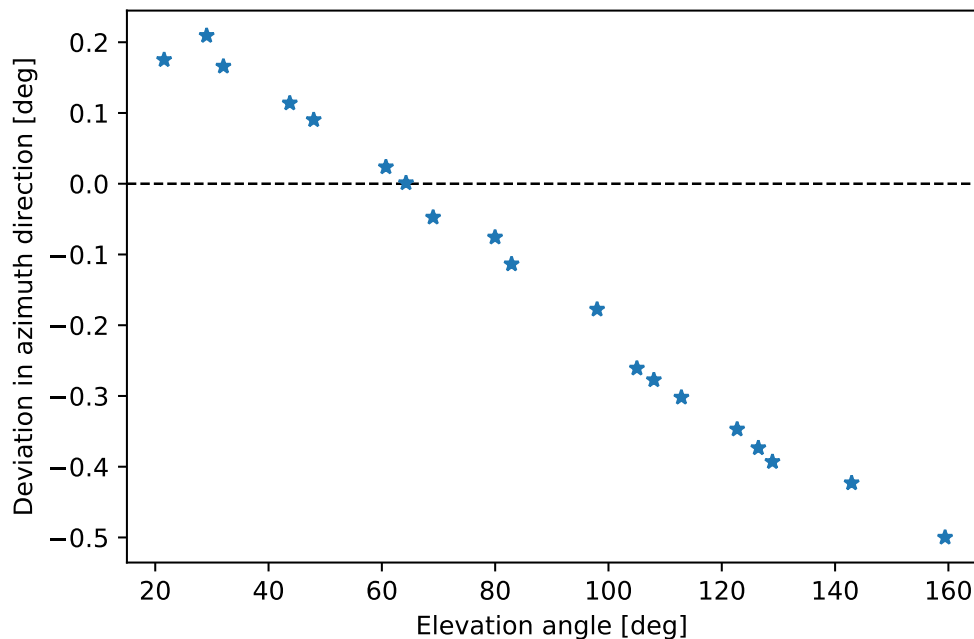


Figure 4.9: Azimuth offset of the main spot: The offset of the main spot to the camera center was measured by determining the center of mass of the spot. The offset in elevation direction is negligible. Here the offset in azimuth is shown. The elevation angle ranges to more than 90° which is related to the fact that the so called reverse pointing capability of the telescope was used as well.

4.6 Final Alignment

Prior to the final alignment, two additional features were added to the software packet.

- To avoid the coarse alignment step, a function was implemented to move the individual light spots of the mirror segments to the camera center using the fine alignment transformation matrix. This was possible because a good alignment had already been performed.
- To further reduce the impact of mechanical play in the actuators probably due to the gear, the final position of the actuators is always reached by pushing against the external springs.

The alignment was carried out between the 19th of January 2014 and the 2nd of March 2014. The alignment system performed as expected. The long duration of the alignment compared to the expectations of Schwarzburg (2012) is explained by delays because of the rainy season in Namibia and the carefully selected alignment conditions. Figure 4.10 shows the dark time efficiency for CT1-4 during the first two shift periods in 2014

during which the alignment of CT5 took place. More than 60% of the dark time the four telescopes could not observe because of bad weather which of course also affected the alignment of CT5. The database was not filled correctly for CT5.

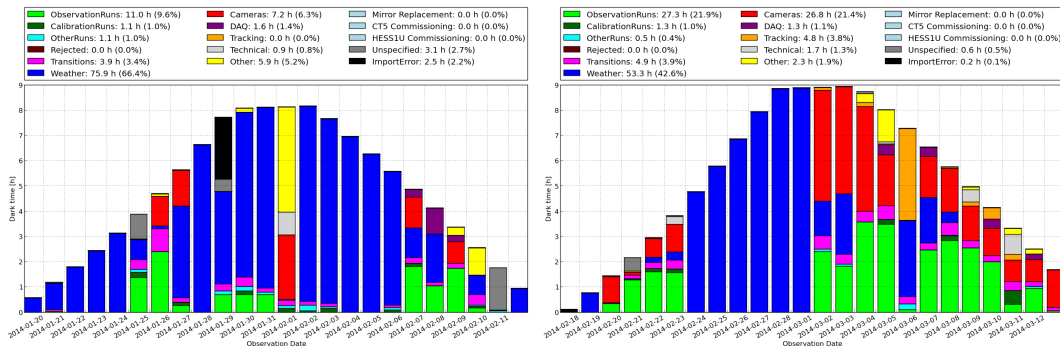


Figure 4.10: Dark time efficiency of CT1-4 during the alignment of CT5: For each night the available observation time is shown over plotted with the time the telescopes spent on different tasks. More than 60% of the time the four telescopes could not observe because of bad weather which also affected the alignment of CT5.

4.7 Results

4.7.1 Point Spread Function

After the alignment the psf was characterized by measuring the extent of star images under various elevation angles. From the previous alignment to the final alignment a small improvement is visible, probably due to the reduced impact of the mechanical play. Figure 4.11 shows a comparison between the two alignments. The final one is shown in green, the previous one in blue. The offset in azimuth has been corrected successfully. The minimal measured spot size is almost equivalent to the minimal simulated spot size, verifying the simulation parameters for the mirrors and the performance of the alignment system. For CT1-4, Cornils (2006) characterized the dish bending with the following function:

$$R_{80}(\Theta) = \sqrt{R_{\min}^2 + d_0^2 (\sin \Theta + \sin \Theta_0)^2}. \quad (4.5)$$

The minimum extent of the light spot R_{\min} is reached at an elevation angle of Θ_0 which is between 60° and 70° corresponding to the elevation angle range used for the alignment. The parameter d_0 is a measure of the magnitude of the dish bending. This behavior was also used for the original simulation shown in red in figure 4.11. Since the

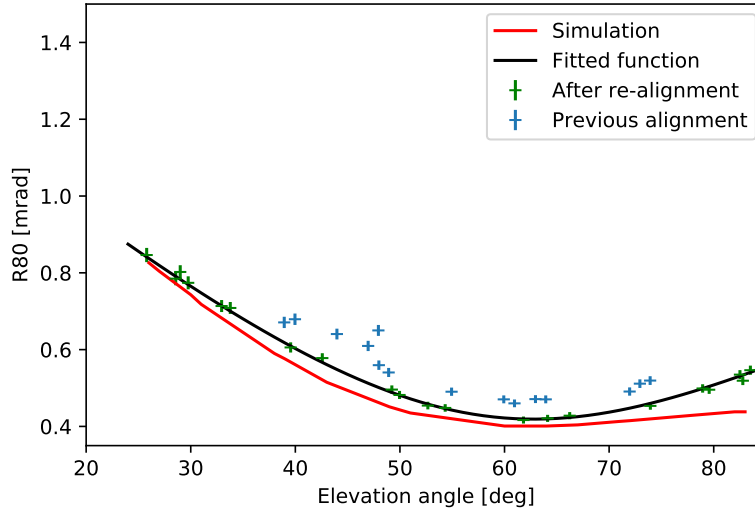


Figure 4.11: Result of the final mirror alignment of CT5: The measured R_{80} over different elevation angles (green data points) is fitted with equation 4.6, the fit results are shown in 4.3. For comparison the original simulation is plotted in red and the data from the previous alignment is plotted in blue.

Table 4.3: Fit parameters to model the dish bending of CT5

R_{\min} [mrad]	Θ_0 [deg]	d_0	d_1	$\chi^2/\text{d.o.f.}$
0.419 ± 0.006	63.1 ± 0.5	1.34 ± 0.06	0.91 ± 0.06	5.47/17

larger and heavier dish of CT5 leads to a stronger bending for large elevation angles, the function is no longer valid to describe the system. Therefore, an additional term was added:

$$R_{80}(\Theta) = \sqrt{R_{\min}^2 + d_0^2 (\sin \Theta + \sin \Theta_0)^2 + d_1^2 (\cos \Theta + \cos \Theta_0)^2}. \quad (4.6)$$

The additional cosine term was introduced to model the bending for large elevation angles, d_1 is a measure of the strength of this additional bending. This function has been fitted to the data with the best fit the parameters listed in table 4.3.

For the simulations, the dish bending is modeled using a elevation dependent alignment error. The quality of the mirrors is known, so the alignment error is derived from the fit presented here. The simulations have been adjusted by the additional cosine term.

Table 4.4: Yearly increase of the psf size for all telescopes

Telescope	Increase in psf size
CT1	$(2.55 \pm 0.23) \%$
CT2	$(2.13 \pm 0.16) \%$
CT3	$(3.85 \pm 0.33) \%$
CT4	$(1.11 \pm 0.11) \%$
CT5	$(2.76 \pm 0.39) \%$

4.7.2 Long Term Stability

The telescopes are designed in a way that the psf should be stable over an extended period of time. This is verified on a regular basis with calibration measurements. In the past, the alignment of CT1-4 did not need an update for more than seven years. With the entire array, 80 pointing runs are carried out per shift period (four weeks) for the mechanical pointing model. The telescope is pointing to a star and the deviations from the spot to the camera center is measured. As an additional input, the images from the Sky-CCD, a CCD camera in the dish measuring the position of the stars in the field of view of the telescope, is used. For CT5, this measurements are carried out using the auto focus setting for the γ -ray observations. For CT1-4 these pointing runs provide a valid input for the psf monitoring, but for CT5 the auto focus unit needs to be set to the position of the alignment. Therefore, a new run type was created called psf runs. No sky-CCD images are taken and the auto focus is set to 0 mm. Every two to three months 30 stars are measured this way, well distributed over the elevation range of the telescope. For each set of 30 measurements from one night, a fit of equation 4.6 is performed and the R_{80} is evaluated at 65° . These values are plotted over time and a linear trend is fitted to the data. Figure 4.12 shows all measurements taken since the 3rd of April 2014. The trend shows a moderate increase of $(3.12 \pm 0.48) \%$ per year. Table 4.4 lists the yearly increase of the psf size of CT1-5 as of spring 2018. For CT3 the yearly increase from spring 2017 is listed. In summer 2017 a mirror exchange was done and the data is insufficient to provide a reliable number of the yearly increase. For each telescope a representation of the elevation plots and the long term monitoring plot is shown in section A.1.

Another consideration of the long term performance of the system is the functioning of the mechanical and electronic parts. For CT1-4, mirror exchange campaigns suffered from a high number of non-operational actuators (see section 4.9). To avoid a similar problem with CT5, regular tests were performed every six months until 2016. For the test all actuators were moved away from the alignment position by 500 hallcounts in both directions. Out of 1752 only 10 actuators did not move the requested counts, though the alignment position of 8 of them is close to the end point of the actuator

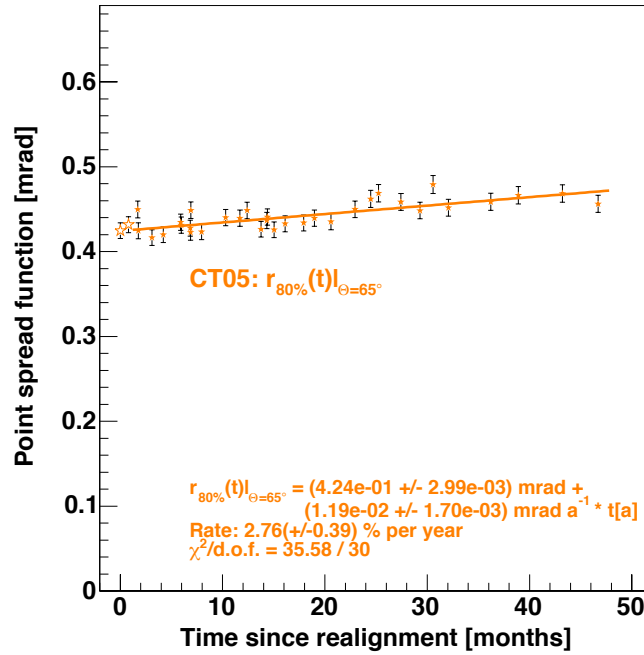


Figure 4.12: Long term monitoring of the optical psf of CT5: The plot shows the R_{80} at 65° measured in regular intervals. A linear trend is fitted to the data.

range. No full test of the actuator range was done to avoid losing the alignment position and because it would take a significant amount of time. The test showed that improvements concerning water tightness used for the CT5 actuators are effective which also is a valuable insight for the actuator development for CTA. Since the psf is stable and a further mirror alignment is not planned during the lifetime of H.E.S.S., further tests were stopped. The results of the alignment campaign, the long term monitoring of the psf and the hardware tests have been published in Gottschall et al. (2015).

4.8 Reverse Pointing for Prompt Follow Up Target of Opportunity Observations

4.8.1 Introduction

The H.E.S.S. experiment features an automatic follow up system for short lasting target of opportunity observations, mostly GRBs, but the scheme can also be applied to other phenomena. GRBs are short lasting phenomena, the measured duration of the prompt phases ranges from 0.1s to a few hundred seconds. They emit up to 1×10^{55} erg of energy in this short time interval which makes them one of the most powerful events known today. The emission can be divided into two phases, the prompt phase of the

intense emission with energies ranging from keV to GeV and the afterglow phase in which the emission decays. The afterglow of GRBs is commonly detected in the radio to optical band. According to the Fireball-Model presented by Piran (1999), particle acceleration takes place at multiple points of the evolution of the system. In this model, when a new compact object is formed, ultra-relativistic jets are created which are powered by the new compact object. Shells with various Lorentz factors are created which eventually collide and create γ -rays in a broad energy range from keV possibly up to TeV. This is the so called prompt phase. In a second phase, the afterglow phase, the shocks reach the not shocked ISM. The highest energy that can be observed in these various stages highly depends on the photon field in the object. A very dense photon field leads to γ - γ absorption which can reduce the initial energy of the radiation. Furthermore, the absorption through the extragalactic background light (EBL) has to be taken into account for large distances from Earth.

Only a small fraction of the detected GRBs (less than 1%) show a component above 10 GeV. These GRBs already challenge the understanding of the Fireball-model concerning gamma factors and acceleration efficiency. These measurements stem from satellite based γ -ray detectors. With IACTs, such a measurement can be performed with an effective area of several orders of magnitude larger and therefore, on much shorter time scales. The highest energies are reached in the prompt phase, therefore it is crucial to start the observations as fast as possible.

Hoischen et al. (2017) reported on the status of the GRB follow-up program currently in place. A key component is the automatic follow-up of online triggers from various sources. The transition time of all subsystems has been optimized making the slewing to the new source the most time consuming task. The tracking system of the H.E.S.S. telescopes is capable of reverse pointing. In this case the telescope can move through zenith with the elevation drive basically turning the telescope upside down. Depending on the start and final position, this reduces the angular distance to the target significantly. For CT5 it was planned that this operation mode is active for prompt follow up of short lasting transient phenomena like GRBs. For CT1-4 reverse pointing is not planned, the mode is only used for maintenance. Figure 4.13 shows the simulated fraction of times CT5 is on target to a random position on the sky over the time since the repositioning started for normal operations ($EL < 90^\circ$) and including reverse pointing ($EL < 175^\circ$). A fraction of 90% is reached after 52s for reverse pointing whereas in normal operation the same is achieved after 107s (Hofverberg et al., 2013).

One key question that needed to be answered is the optical performance of the system for a reverse pointing. The results of optical psf measurements is presented in the

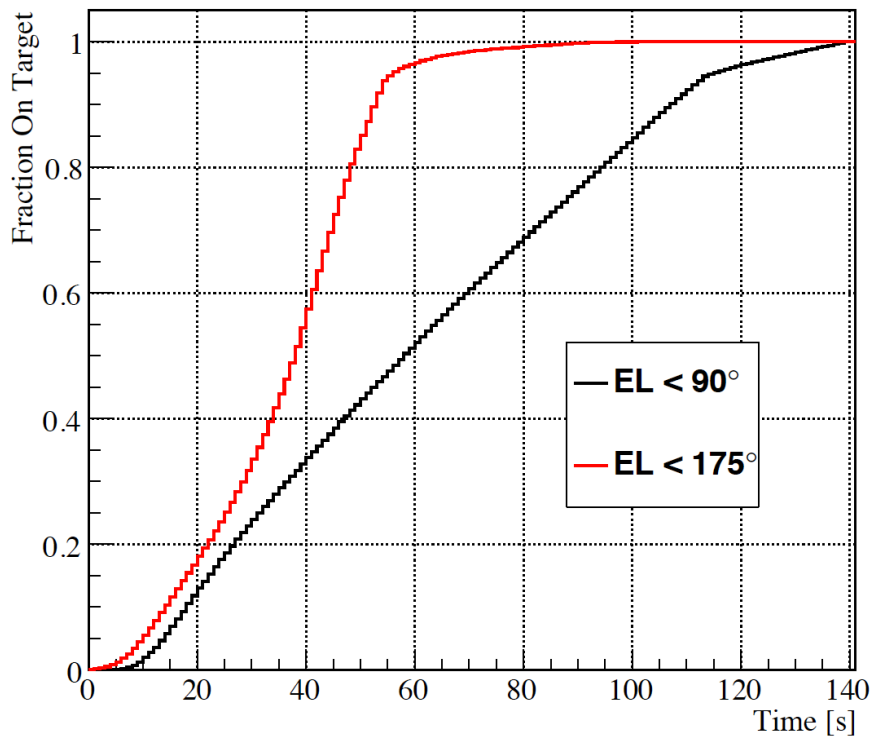


Figure 4.13: Performance of the CT5 drive system: The plot shows the fraction of times CT5 is on target to a random position on the sky from a random position over the time since the repositioning started for normal operations in black ($EL < 90^\circ$) and including reverse pointing in red ($EL < 175^\circ$). The plot is taken from Hofverberg et al. (2013).

following section together with an estimate of the impact on the effective area for γ -rays of the telescope.

4.8.2 Impact on the Optical System

To characterize the optical psf for reverse pointing, the psf was measured for several stars with different elevation angles. The first tests were done before the final alignment which at that point had already been planned. During these tests the following behavior was observed:

- The size of the star images increases further with rising elevation angle.
- The increase in star image size is not continuous, but there is a step at around 90° elevation.
- The psf shows a moderate increase in size for normal pointings right after a reverse pointing at all elevation angles.

4.8. REVERSE POINTING FOR PROMPT FOLLOW UP TARGET OF OPPORTUNITY OBSERVATIONS

At 90° there is a discontinuity of the optical psf size. This is probably caused by the bending of the mirror mounting: For normal pointings, the fixed point is on top and the two adjustable points on the bottom as shown in figure 4.14. When the telescope is moving through zenith the mirror mounting is upside down. This could lead to discontinuous bending of the mounting structure. Another possibility is the bending of the entire dish. The root cause of this effect was not studied.



Figure 4.14: Mirror of CT5 from the back

The last effect is the least understood and also the most dangerous effect, in particular when it accumulates over time. The larger optical psf during normal operations right after a reverse pointing is probably caused by inelastic bending of parts of the dish structure or the mirror mounting. This bending settles over time and is hardly measurable after one day. The increase is about 5% to 10% at 65° elevation (it decreases for other elevation angles) which has a negligible effect on the γ -ray performance. To exclude an accumulative effect, the measurement has been repeated several times and an additional monitoring after a reverse pointing was implemented. No negative long term effect was observed. A sudden increase of the psf size in the long-term monitoring would be such a negative effect (see figure 4.12). Up to summer 2016 reverse pointings were done two to three times per year for tests. After that, the system went to normal operations. Since reverse pointings are only used for prompt GRB follow-ups, such pointings were only done twice in 2017, once during a fire drill for the shift crew and a second time for a GRB follow-up.

Figure 4.15 shows the results of a test of reverse pointing. In the night from the 24th to the 25th of April 2014 the psf was measured at the beginning of the night. Right after that the psf was measured using reverse pointings. The next psf measurement was done 2 h after the beginning of observations and shows an increase in psf size of 6 %. To monitor the normalization process another psf measurement was done at the end of the night, roughly four hours after the reverse pointings. The measured radius R_{80} at 65° elevation is almost compatible with the original value from the beginning of the night. Bad weather prevented another measurement during the next night, but 56 h later the measured psf was back to normal.

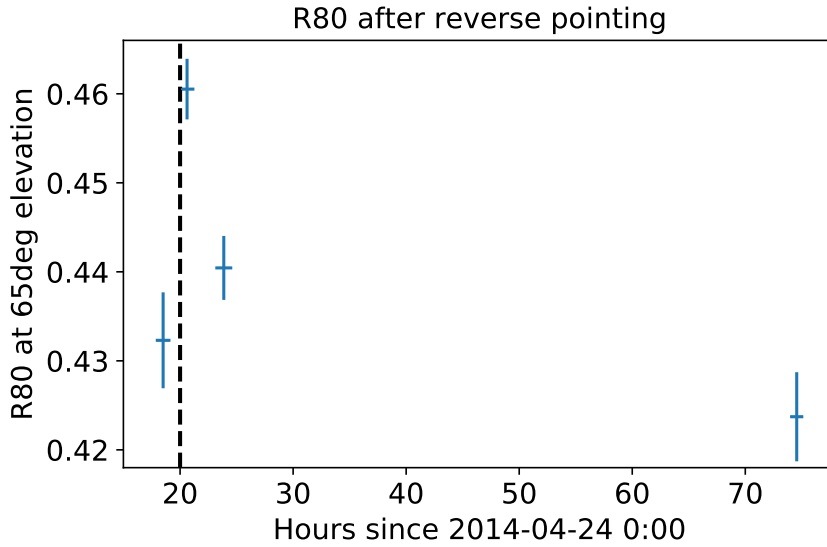


Figure 4.15: Time evolution of the optical psf after a reverse pointing: The plot shows optical psf measurements for normal operations ($\Theta < 90^\circ$) at 65° elevation before and after reverse pointings. The dotted line shows the time of the reverse pointings.

To deliver input for simulating the performance of the telescope, the measurement using reverse pointing was repeated with the final alignment. Equation 4.6 was fitted to the data with frozen $\Theta_0 = 65^\circ$. The results are shown in Figure 4.16.

For $\Theta = 115^\circ$, which is equivalent to an elevation angle of 65°, the optical psf is a factor of two larger than for a normal measurement at 65°.

4.8.3 Impact on the Air Shower Reconstruction

With the measurements of the previous section, S. Ohm performed a simulation of the γ -ray performance of the telescope. A γ -ray simulation at 20° and 45° elevation

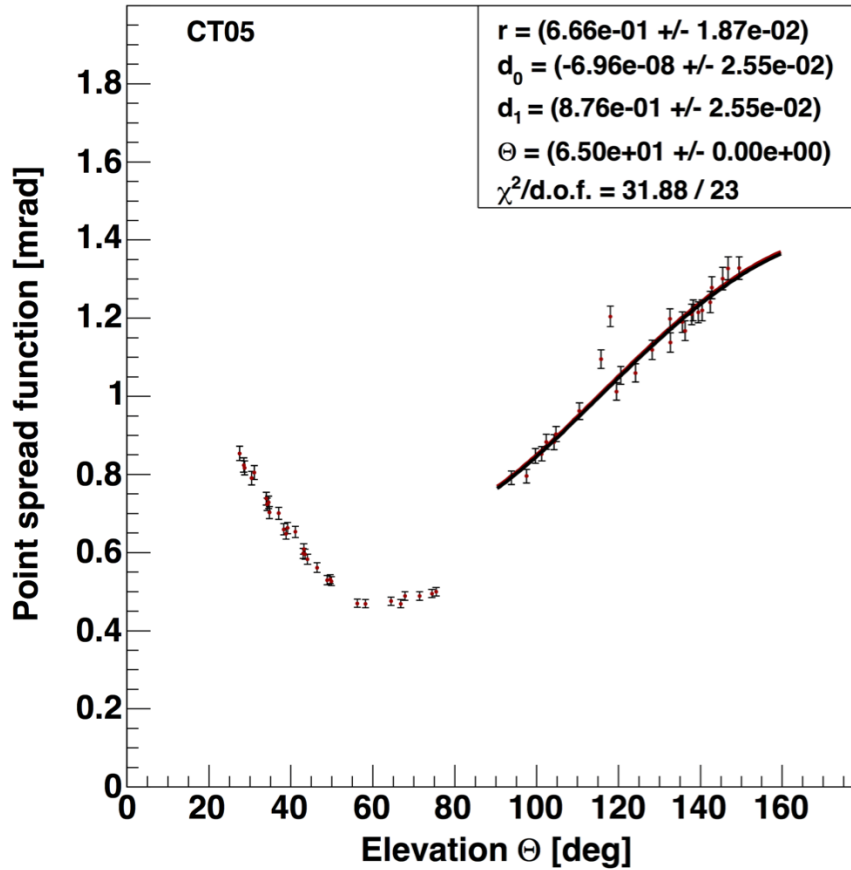


Figure 4.16: Optical psf for reverse pointing: The plot shows optical psf measurements for normal operations ($\Theta < 90^\circ$) and for reverse pointings ($\Theta > 90^\circ$). Equation 4.6 has been fitted to the reverse pointing data points, setting Θ_0 to 65° .

angle was done, once using the normal simulation parameter for the dish matching the measured psf (normal) and a second time adjusting the simulation parameters of the dish to match the measurement from figure 4.16. Figure 4.17 shows the fraction of all events passing the trigger criteria of the instrument (DST) and the analysis cuts for a standard mono analysis (Preselect) over energy. The solid line refers to normal optical simulation parameters and the dashed line to the parameters matching the psf measurement for reverse.

In reverse, the optical psf reaches the same extent as a PMT pixel on-axis. Off-axis, the star light is further widened by aberration. Therefore, low energy showers are distributed over more pixels which leads to low intensity showers not triggering the telescope because of a lack of light in individual pixels. Furthermore, the γ /hadron separation might suffer (independent from the method used) when the shape of the shower can not be measured accurately by the telescope. This effect has not been studied yet.

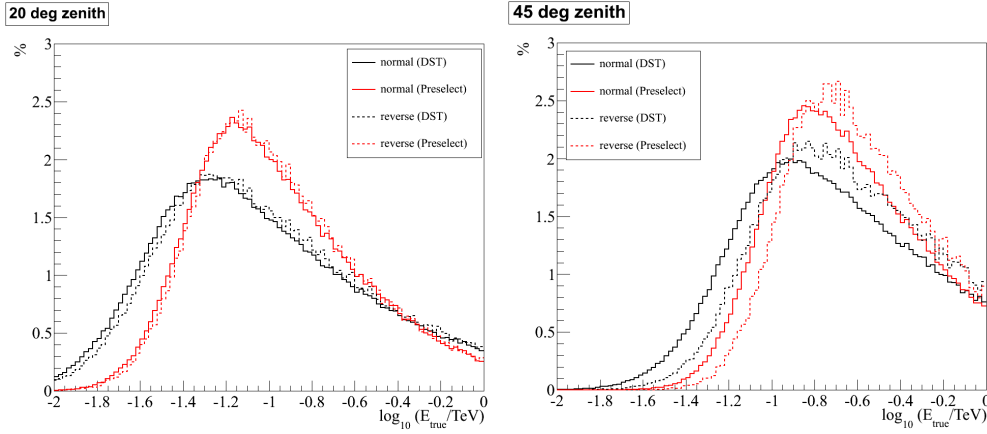


Figure 4.17: γ -ray performance in reverse pointings: The plot shows the fraction of all events, passing the trigger criteria of the instrument (DST) and the analysis cuts for a standard mono analysis (Preselect), over energy. The solid line refers to normal optical simulation parameters and the dashed line to the parameters matching the psf measurement for reverse.

Table 4.5: Increase in energy threshold for reverse pointings

Zenith angle [deg]	Pointing	Level	Energy threshold [GeV]	Increase
20	normal	DST	55	
20	reverse	DST	60	$\sim 9\%$
20	normal	Preselect	70	
20	reverse	Preselect	75	$\sim 6\%$
20	normal	DST	150	
45	reverse	DST	180	$\sim 20\%$
45	normal	Preselect	170	
45	reverse	Preselect	203	$\sim 19\%$

This is a clear tradeoff between performance and response time. The nature of GRBs led to the decision to commission reverse pointings with CT5, but with a limit of 135° which is equivalent to an elevation angle of 45° , to maintain an acceptable performance. This excludes the use of reverse pointing only for some of the events since the minimum elevation angle for a prompt follow-up is 30° in normal mode or 150° in reverse. Assuming that GRBs are distributed isotropically and the telescope is always choosing the smallest angular distance, only 12.5% of all prompt follow-up alerts are excluded from using reverse pointings.

4.9 The 2017 Mirror Exchange of CT3

The optical efficiency of all telescopes declines over time if no maintenance is taking place. This decline is driven by the reflective coating of the Winston cones that funnel the light onto the PMTs, the photocathodes of the PMTs, and the mirrors. The optical efficiency is measured using Cherenkov light from muons passing through the reflective dish of a telescope. Therefore, the measured muon efficiency covers the efficiency of all three components. The technique and optical efficiency applied until 2016 is described by Mitchell (2016). Starting in April 2010 the mirrors of CT1-4 were replaced consecutively. The mirrors of CT3 were replaced first with a new set of mirrors. The used mirrors from CT3 were recoated and then used for CT2. The sequence continued with CT1 and CT4. The mirror exchange caused a downtime of four to six weeks per telescope. One set of spare mirrors was available. It was newly coated before it was put into storage. Since the end of the experiment is approaching and the optical efficiency of the telescopes degraded again, the collaboration decided to use the fifth set of mirrors to exchange the mirrors of CT3. This was the first telescope on which mirrors were mounted and also the first telescope receiving new mirrors in the exchange campaign in 2010. In 2016, the measured optical efficiency of CT3 was lower than the optical efficiency of the other telescopes as it can be seen in figure 4.18. The figure shows the measured muon efficiencies starting in 2004 for all telescopes. The dotted lines mark the first mirror exchange in 2010-2012 (a), the beginning of a PMT camera upgrade (b), and the exchange of Winston cones (c). Smaller increases in optical efficiency are related to cleaning of the Winston cones or rain removing some of the dirt from the mirrors.

The collaboration asked for a downtime of the telescope of less than two shift periods which is roughly two months. Therefore, a maintenance campaign of four weeks was carried out in May/June 2017 to test the entire system as thoroughly as possible without interrupting observations. Although the system was not used for half a decade and the documentation was sparse, the alignment was successfully tested. A few modifications had to be made to account for new CCD cameras and changes in the computer cluster on site. The changes have been documented on web pages of the collaboration. In addition to the test of the entire system and to update to the documentation, a small set of motors were tested for functionality. Only one of 24 motors showed a hardware defect. Based on this, a pessimistic assumption of 20% of motors/actuators that would need service, was used to plan the mirror exchange campaign. The goal was to derive a pessimistic to realistic estimation of the required time. Furthermore, a test setup made of spare parts of the alignment system was constructed to test the actuators under

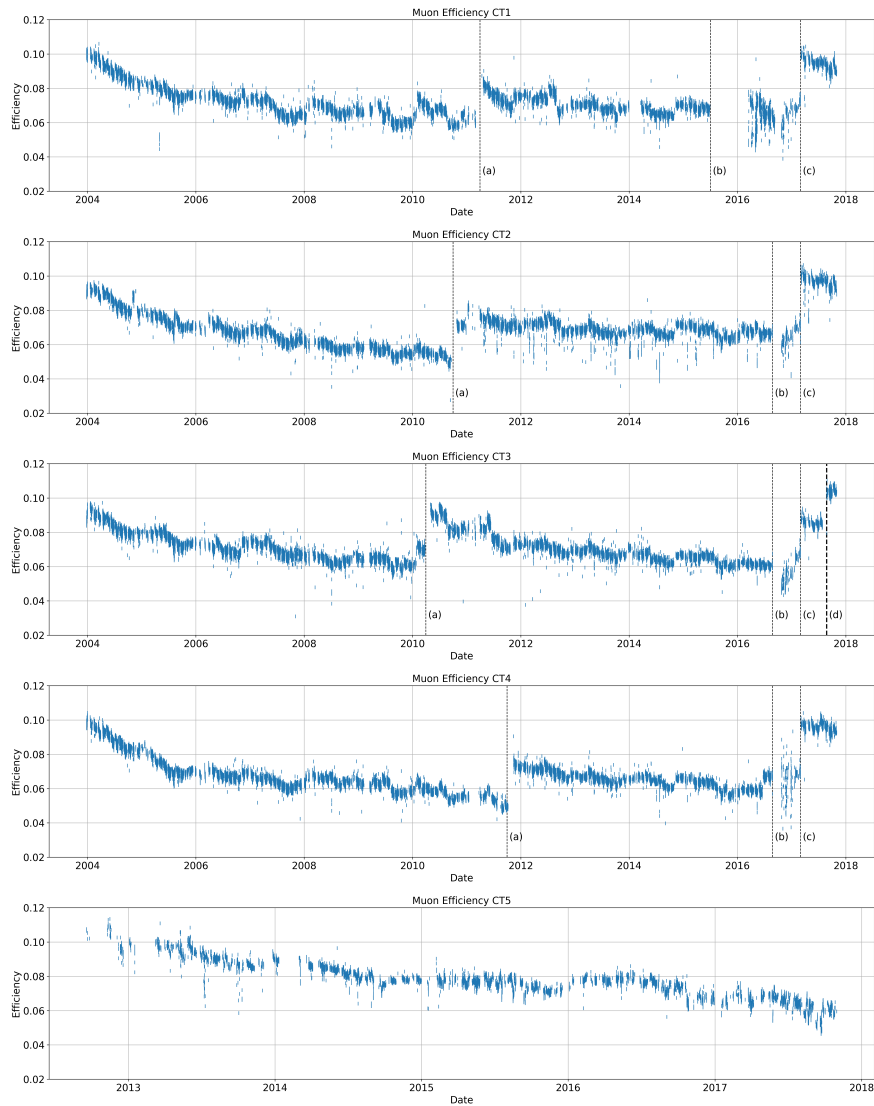


Figure 4.18: Muon efficiency over time: The plots show the measured muon efficiencies since 2004 for all telescopes. The dotted lines mark the first mirror exchange in 2010-2012 (a), the beginning of a PMT camera upgrade (b), and the exchange of Winston cones (c). Smaller increases in optical efficiency are related to cleaning of the Winston cones or rain removing some of the dirt from the mirrors.

realistic conditions before mounting them on the telescope. With this setup 128 mirror mountings could be tested in one night without supervision.

For the campaign 24 days were scheduled, less than half of the acceptable downtime defined by the collaboration board. It was estimated that the exchange of the mirrors would take two weeks, for the alignment one week was scheduled. Before that three days of testing of all actuators in the dish were performed. The goal was to sort out

the broken actuator/motor assemblies. The mirror exchange campaign started on the 27th of July 2017.

At the start of the campaign, the test of all motors in the dish showed that the failure rate was 40%, a factor of two of the assumed one. An analysis of the mirror positions showed that the initial test with 24 motors had been done at the bottom of the dish where the hardware is better protected from rain and sun by the telescope structure. The highest failure rate was observed on top of the dish while the telescope is in parking position. Most actuators or motors were simply stuck and could be recovered easily. A small number of hardware parts needed to be exchanged. This prolonged the mirror exchange by a week.

The alignment was done remotely with the support of the observation shift crew. During the alignment no major problems were discovered. The telescope was aligned within 5 days. Normal operations resumed on the 27th of August 2017, one month after the beginning of the campaign. The resulting optical psf is shown in Figure 4.19.

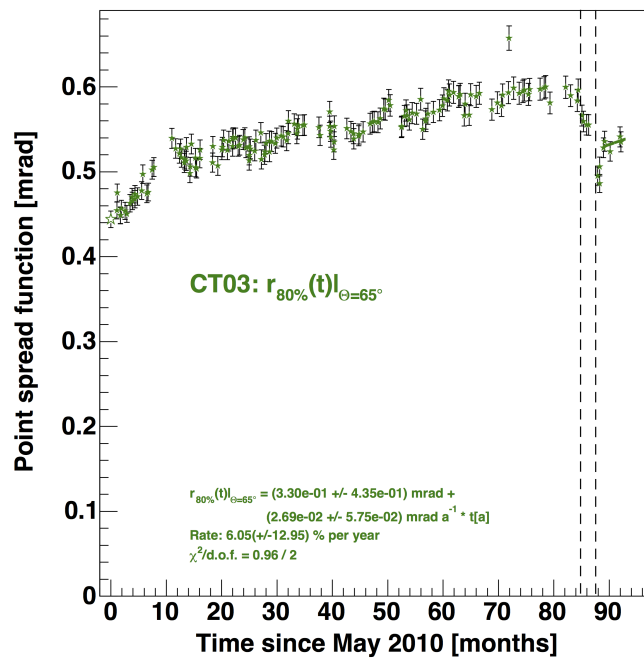


Figure 4.19: Optical psf for CT03: The plot shows optical psf measurements from May 2010 when the previous mirror exchange was done. The first dotted line indicates the time of a focusing of the lens of the CCD camera. The second dotted line shows the time of the mirror exchange presented here.

In conclusion, the quality of the new alignment is better than the alignment right before the mirror exchange. The fact that the psf size of May 2010 was not reached is probably caused by a degradation of the focus of the optics of the CCD camera that is used to monitor the size of the psf. Concerning the rate of increase in size, at this point in

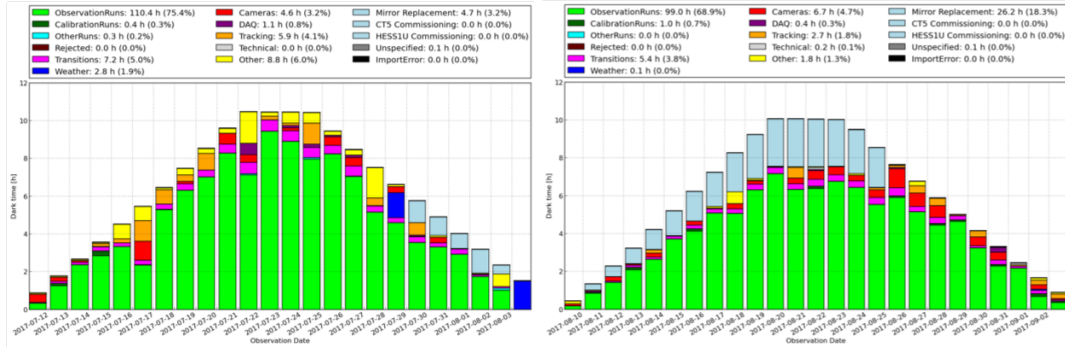


Figure 4.20: Darktime efficiency of the full array during the CT3 mirror exchange campaign.

Table 4.6: Muon efficiency November 2017

Telescope	Muon efficiency
CT1	~ 0.091
CT2	~ 0.093
CT3	~ 0.102
CT4	~ 0.093

time the measurement is not conclusive. More data is needed. Figure 4.20 shows the observation time that was lost due to the mirror alignment. The alignment took place in between two shift periods which minimized the loss of observation time.

Figure 4.21 shows the muon efficiency from the beginning of 2016 until the end of 2017. A clear increase in muon efficiency is visible at the dotted line (c) which indicates the exchange of Winston cones and at the dotted line (d) which indicates the time the mirror exchange presented here took place. An increase in muon efficiency of $\sim 18\%$ was measured. The muon efficiency of the individual telescopes as of November 2017 is listed in table 4.6.

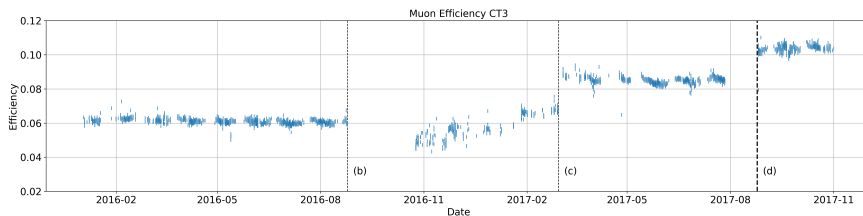


Figure 4.21: Muon efficiency of CT3 over time: The plots show the measured muon efficiencies since the beginning of 2016 until the end of 2017. The dotted lines mark the beginning of a PMT camera upgrade (b), the exchange of Winston cones (c), and the mirror exchange presented here (d).

4.10 Summary

The large number of mirror segments used within the H.E.S.S. experiment required a motorized alignment system. In this work the performance of the mirror alignment and control system of H.E.S.S. phase II has been verified after an extensive study covering measurements at the telescope and simulations. Furthermore, because of unrelated calibration problems a new alignment of CT5, the 28 m telescope, was performed after improving the algorithms to allow for a fast alignment with higher precision. The results of this new alignment fulfill all expectations and have been published by Gottschall et al. (2015). The optical performance of CT5 has been investigated in the so called reverse pointing mode for fast re-positioning. These measurements provided valuable contributions to the further development of the H.E.S.S. transient program. A regular monitoring of all telescopes has been implemented and documented. A mirror exchange of CT3, one of the 12 m telescopes was done including a full new alignment. The hardware was not used for seven years and only partially operational when the preparations for the mirror exchange started. In a maintenance campaign of four weeks the functionality of the hard- and software was restored and the procedures for the mirror exchange prepared. The mirror exchange was carried out without problems and well inside schedule. The telescope CT3 gained $\sim 18\%$ in optical efficiency. This study demonstrates the precision and the reliability of the mirror alignment and control approach of the H.E.S.S. collaboration, both for the 12 m phase I telescopes as well as for the 28 m telescope CT5. Ideally, the imaging performance of the telescopes should be limited by the granularity of the PMT camera and not by the optical properties of the dish. Therefore, according to the study from Bernlöhner et al. (2003) the psf should be smaller than the PMT pixel size of 0.16° on-axis for CT1-4. The 28 m telescope CT5 has a PMT pixel size of 0.067° . Translated to a radius in radian the psf should be smaller than 1.4 mrad for CT1-4 or 0.58 mrad CT5. As this study has shown this is the case for most normal elevation angles for all telescopes. Only when using reverse pointings or low elevation angles with CT5, the measured R_{80} is larger than the pixel size. With the psf measurement of CT5 after the final alignment presented here, the instrument simulation has been adapted to match the measurements. The limited impact of the quality of the alignment on the performance of the instrument does not make regular updates of these parameters necessary. Nevertheless, the quality of the alignment is monitored with long-term psf measurements. The results are presented regularly and are brought to the attention of the simulation experts.

5 A Study of Three TeV Shell Candidates from the H.E.S.S. Galactic Plane Survey with H.E.S.S.

5.1 Introduction and Outline

5.1.1 Introduction

SNRs are the prime candidates for accelerating the bulk of Galactic hadronic CRs and are therefore one of the major science topics of IACTs like H.E.S.S. As discussed in chapter 2, VHE γ -rays are a tracer for very energetic CRs. Identifying SNRs solely based on data from γ -ray instruments, poses several problems due to the angular resolution of the instruments and intrinsic properties of the sources. A distinct feature of young and mid-age SNRs is the shell expanding into the ISM creating VHE γ -ray emission. Resolving this shell with an angular resolution of $\sim 0.8^\circ$ for a typical observation is only feasible for sources with a large apparent extent. Old SNRs no longer accelerate particles and the remaining hadronic CRs diffuse into the ISM. The morphology is no longer a criterion to identify the source type. One example is W 28 (Aharonian et al., 2008c). Supernova remnants usually exhibit a power-law spectrum with an index of $\Gamma = 2.3$ in the VHE band, similar to the spectrum of most Galactic VHE γ -ray sources. In this chapter, a new approach to search for new SNRs in the Galactic plane with H.E.S.S. is introduced. The thereby discovered candidates are presented in an extensive source-by-source study covering sky-maps, energy spectra, morphological study, and search for multi-wavelength (MWL) counterparts.

The large field of view (FoV) and the location in the southern hemisphere makes H.E.S.S. the perfect instrument for a Galactic Plane survey. Thus, two types of observations were initiated when the first phase of the array of telescopes was completed: In addition to pointed observations of known γ -ray emitters like the Crab Nebula (Aharonian et al., 2006b) or prime candidates like RX J1713.7–3946 (Aharonian et al., 2006a), H.E.S.S. started a survey observation. These observations culminated in the publication of the first Galactic Plane survey (Aharonian et al., 2006c). Afterwards,

the survey was continued and also deeper observations of special regions of interest were added to the H.E.S.S. dataset. This led to the final publication of the H.E.S.S. Galactic plane survey (HGPS) (H.E.S.S. Collaboration, 2018d), which includes 10 years of data and covers half of the Galactic plane. When the search for TeV shell candidates started, the preliminary HGPS catalog contained 78 γ -ray sources, 37 of them not firmly identified.

The question was raised whether some of the unidentified sources are in fact shell-like SNRs. Galactic SNRs are usually discovered in other wavebands first and mainly in the radio band. Several sources have been detected first in X-ray surveys with *ROSAT* and *ASCA* (Aschenbach, 1995; Bamba et al., 2003; Pfeffermann et al., 1991; Sugizaki et al., 2001; Bamba et al., 2001; Yamaguchi et al., 2004). These SNRs typically have a low radio surface brightness (e.g. RXJ 1713.7–3946) or are in regions with source confusion. Based on the X-ray detections, the most probable candidates for γ -ray emission have been observed which initiated the discovery of shell-like sources like RX J1713.7–3946 (Aharonian et al., 2006a). Unidentified VHE are usually observed in other wavebands, for example with pointed X-ray observatories like *XMM-Newton* or *Chandra* because of their good sensitivity and the expected synchrotron emission in their energy band. One example is HESS J1731–347, published by the H.E.S.S. collaboration (Aharonian et al., 2008b) as an unidentified source, followed by the discovery of an X-ray and radio counterpart by Tian et al. (2008), which led to the classification as a SNR. The MWL information led to deeper observations with H.E.S.S. which then revealed a shell structure at TeV (H.E.S.S. Collaboration, 2011). These are examples where MWL information leads to the discovery of VHE sources or to the firm identification of VHE sources discovered in a survey. As described in section 2.2, the acceleration of charged particles at a shock front induces both synchrotron emission from leptons covering energies from the radio- to the X-ray-band, and γ -ray emission both from leptons and hadrons. The examples mentioned here are interpreted as young SNRs where the shock speed is sufficient for ongoing particle acceleration. When the shock slows down, the acceleration stops and no new high energy leptons and hadrons are produced. In contrast to leptons, hadrons need more time to cool before they can no longer produce γ -ray emission. One example is known where the protons from the old-age SNRs W 28 diffuse into the ISM and illuminate close-by molecular clouds (Aharonian et al., 2008c). Following this argument, in the case of a γ -ray source only detected at VHE that shows clear evidences of being a shell-like SNR, but without a counterpart in the radio or X-ray band, a possible conclusion is that such a source could be a medium age SNR with much slower shock speeds compared to the young SNRs detected at VHE. In this case, the emission would be dominated by hadronic interaction. This would provide the missing link between young SNRs like RXJ 1713.7–3946 and old SNRs like W28 where

the SNR is no longer accelerating particles, but illuminates nearby dense molecular clouds with CRs diffusing into the ISM. (Aharonian et al., 2008c).

The non-detection of X-ray synchrotron emission can have other reasons. For example an observation can suffer from high absorption or stray light contamination. The existence of a TeV source with shell morphology alone is no immediate proof of the scenario of a mid-age SNR, a spectral energy distribution (SED) modeled with constraining upper-limits from X-ray and radio is needed. Furthermore, the identification as SNR of any age from TeV data alone is not possible. Other astrophysical sources can mimic a shell appearance, for example, because of source superposition or even intrinsically, e.g. in the case of super-bubbles: A VHE γ -ray emitting super-bubble has been found in the Large Magellanic Cloud (LMC) recently (H.E.S.S. Collaboration, 2015).

5.1.2 Outline

For this work, a blind search for shell like morphologies was done with the data product of the HGPS (H.E.S.S. Collaboration, 2018d). From this search four source candidates emerged. In addition two more sources were suggested by collaboration members because the sources were in the field of view of their analysis and appeared shell-like by eye. The HGPS and the blind search is presented in section 5.2.

For these six sources, a source-by-source H.E.S.S. analysis was done to derive sky maps and energy spectra. With the results of this dedicated analysis a morphology study was performed to confirm the results of the systematic search. In this study three of the four candidates of the search showed a significant shell-like morphology. Of the two candidates identified "by eye", none showed a preference of the shell model. The three positively identified sources are called HESS J1534–571, HESS J1614–518 and HESS J1912–101. Although an in depth analysis and morphological study was done on six sources, only the results for the firmly identified SNR candidates are shown here. The other three sources were treated in the same way, up to the morphological study. Based on the conclusions of the study, a MWL search for counterparts was started. The source-by-source analysis is presented in section 5.3. The search for MWL counterparts is presented in section 5.4.

This work is the result of a collaboration of several members of H.E.S.S. and external colleagues. The main focus of the author's work was the source-by-source analysis and part of the search for MWL counterparts, mainly working on the radio continuum emission of HESS J1534–571, the GeV emission with *Fermi*-LAT for HESS J1614–518, and investigating the differences to the study of Aharonian et al. (2008a) concerning

HESS J1912+101, which resulted in a possible PWN scenario at that time. Furthermore, the author carried out several catalog searches in which no additional positive matches were found. For the sake of completeness, the results of the work of the entire task group is presented here. The work of the author is explained in greater detail covering the source-by-source analysis, azimuthal and radial profiles of the TeV data, the spectral analysis, examination the radio continuum emission towards HESS J1534–571, the GeV emission towards HESS J1614–518, re-examination of the PWN scenario for HESS J1912+101, and catalog searches for all three sources.

5.2 Search for New TeV Shell Candidates in the H.E.S.S. Galactic Plane Survey

5.2.1 The H.E.S.S. Galactic Plane Survey

The HGPS is a decade long study using data from the first phase of the H.E.S.S. experiment⁷. It consists of survey observations and pointed observations within a box covering the Galactic longitude range of $l = 250^\circ$ to 60° (including the Galactic center) and the galactic latitude range of $|b| \leq 3.5^\circ$. All data of high quality, taken between 2004 and 2013, were considered in the survey. The total amount of observation time sums up to almost 2700 hours. The strict quality selection of the observational data ensures a high precision of the flux maps created in the study.

The latest HGPS publication (H.E.S.S. Collaboration, 2018d) incorporates high-level sky-maps. This includes correlated γ -ray Excess and Significance maps, a Flux map and a source catalog containing 16 new sources that have been partially announced at conferences, but were not published before. Compared to previous H.E.S.S. publications, four sources are missing. This is not surprising because all of the four sources have a softer spectrum, their non-detection is a consequence of the analysis settings used. To increase the precision of the direction reconstruction and the discrimination power of the γ /hadron separation, a high image amplitude cut was used, which increases the energy threshold of the analysis. One example is W49B with a power law index of $\Gamma = 3.1$ (H.E.S.S. Collaboration, 2018f). The analysis cuts are explained in detail in the upcoming section 5.3 or in H.E.S.S. Collaboration (2018d). The catalog was derived using morphology fitting of Gaussian components to the sky-maps. To increase the stability of the method, known shell-like SNRs and the Galactic center region have been excluded.

⁷H.E.S.S. phase I: September 2004 until July 2012. Phase I ended with the inauguration of CT5, data until 2013 are still considered phase I because of a calibration phase.

In addition to the source catalog pipeline, the low level sky-maps of the HGPS, most importantly *Gamma candidates* and *Gamma exposure* among others, became available within the collaboration. These maps have been used for other studies for example the search method presented in section 5.2.2.

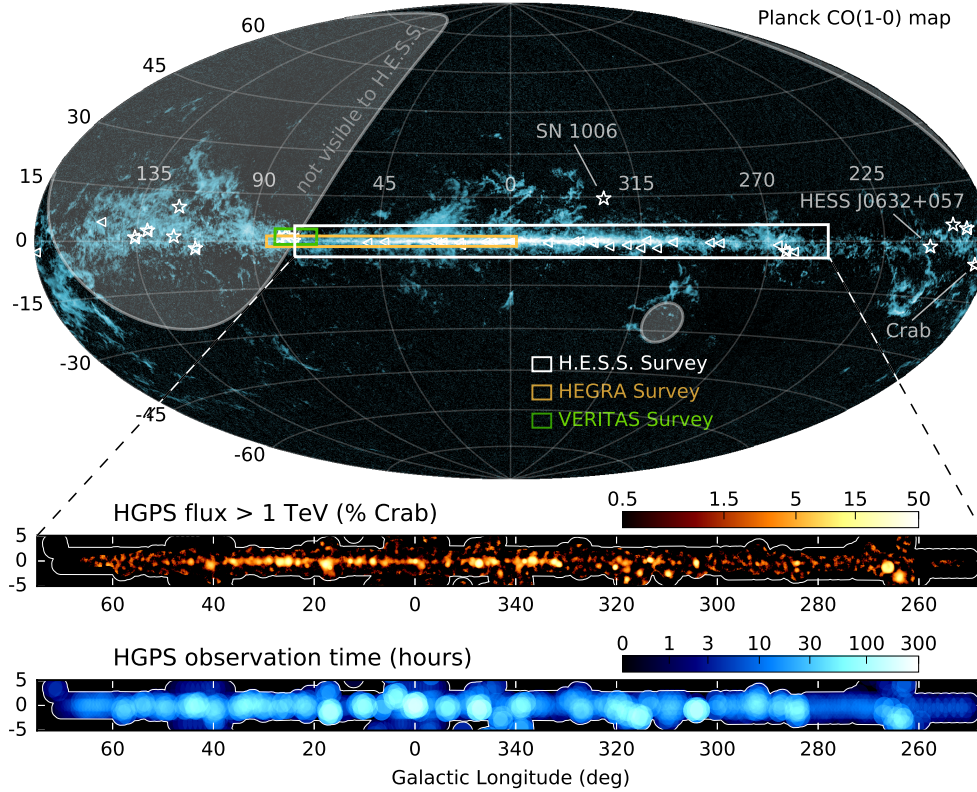


Figure 5.1: Illustration of the HGPS: The top panel shows an all sky image of CO emission measured with the *Planck* satellite. The white stars illustrate 10 known VHE γ -ray emitters outside the survey region. The orange and green boxes show the HEGRA and VERITAS survey regions for comparison. The white box contains the sky region covered by the HGPS, the boxes below show the measured flux above 1 TeV in units of percent of the flux of the Crab Nebula and the amount of observation time in hours (H.E.S.S. Collaboration, 2018d, and reference therein).

5.2.2 Search Method

Within the H.E.S.S. collaboration a discussion on the nature of HESS J1912+101 started in 2011. By eye the source seemed to be shell-like and preliminary statistical tests suggested the same. For the HGPS source catalog, a fit of Gaussian components was done to the resulting γ -ray maps. A Gaussian shape is a good assumption for most VHE γ -ray sources observed with H.E.S.S. Gaussian components are a good

choice because first, they describe a point-like source well, and second, because the most abundant Galactic VHE source class, PWNs, is described very well by a Gaussian model. Nevertheless, these Gaussian components partially needed to be merged into one astrophysical source. For details see H.E.S.S. Collaboration (2018d). Because of its complexity the Galactic center region has been masked as well as known shell-like SNRs. When the settings for the final source catalog were defined, the question was raised whether other sources show a shell-like morphology apart from the already suspected HESS J1912+101. Selecting SNRs from the VHE is a promising approach to potentially reveal sources with previously unknown properties as discussed in the introduction. Therefore, the search was performed using the pipeline of the HGPS, but instead of testing Gaussian component with free parameters, a fixed set of models (shell and Gaussian) with fixed extent have been tested on the grid of the HGPS sky-maps. For this statistical test the Gaussian model is the null-hypothesis (H_0) where the shell model is the hypothesis that is tested (H_1). The grid is defined by the binning of the sky maps which was chosen to be $0.02^\circ \times 0.02^\circ$ (H.E.S.S. Collaboration, 2018d). The binning is smaller than the angular resolution of the dataset of 0.08° but limits the number of trials for the source detection algorithm or the shell search method. Only the normalization of the models could be varied. This was done to save computing time for the fitting and to avoid cases in which the fit would not converge. The model parameters are listed in table 5.1.

The Gaussian model for the search was defined as

$$S_{\text{Gauss}}(r|\Phi, \sigma) = \Phi \frac{1}{2\pi\sigma^2} \exp\left(-\frac{r^2}{2\sigma^2}\right). \quad (5.1)$$

To model a possible SNR, a description was chosen that models the emission in a three dimensional shell projected to two dimensions. It was assumed that the source is emitting γ -rays homogeneously between the outer and inner radius of the shell. This is a fair assumption for a SNR expanding with supersonic speed into the ISM accelerating CRs at the shock front. The known TeV SNR shells are described well by this model (c.f. table 5.3). Mathematically this is defined as

$$M(r) = A \times \begin{cases} \sqrt{R_{\text{out}}^2 - r^2} - \sqrt{R_{\text{in}}^2 - r^2} & , \quad r < R_{\text{in}} \\ \sqrt{R_{\text{out}}^2 - r^2} & , \quad R_{\text{in}} < r < R_{\text{out}} \\ 0 & , \quad r > R_{\text{out}} \end{cases} \quad (5.2)$$

From the HGPS a map of so called *Gamma candidates* is available containing all events passing the γ /hadron separation. Furthermore, a *Background* map is available created

exploiting the adaptive ring method. From Monte-Carlo simulations an *Exposure* map was created by stacking the radial acceptance for simulated γ -rays for individual runs. Also from simulations the psf of the experiment is derived, first for the specific observation run and then stacked to one psf for a specific observation position. For a detailed description of event reconstruction, background separation, background estimation and simulations see chapter 3. The γ -ray simulations are done for a fixed power-law energy spectrum. To derive the correct exposure and psf, the number of simulated events per energy is weighted with a power law. For the HGPS an assumed index of $\Gamma = 2.3$ was used. During the fitting procedure the number of Counts (*Gamma candidates*) is modeled as

$$\text{Counts} = \text{Background} + \text{PSF} \times (\text{Model} \cdot \text{Exposure}). \quad (5.3)$$

Following Cash (1979) by using the *cstat* implementation in *XSPEC* the likelihood fit used maximizes the so called *Cash* statistics:

$$C_S = 2 \sum_i (M_i - D_i \log M_i). \quad (5.4)$$

The model M_i is equivalent to the expected number of counts per bin i according to equation 5.3. D_i is the measured number of counts per bin after γ /hadron separation (*Gamma candidates*). The sum is taken over all bins of the region of interest.

To test the statistical significance of the fit, C_S is compared to the statistics of a pure background model C_0 . Taking the difference of the test statistics of the two models, a likelihood-ratio test statistic is calculated:

$$TS = C_S - C_0. \quad (5.5)$$

According to the Wilks' theorem the TS is asymptotically distributed like a χ_N^2 distribution where N is the number of free parameters. This means that for a large number of counts the square root of TS corresponds to the statistical significance. For a given model, for example a Gaussian model with a fixed width at the positions of the sky map grid tested against a pure background, the significance of the emission at a given grid position can be calculated:

$$S = \text{sign}(\Phi) \sqrt{TS}. \quad (5.6)$$

Table 5.1: List of tested Gaussian (H_0) and shell (H_1) parameters for the grid search; shell width w is defined as $w = R_{\text{out}} - R_{\text{in}}$.

Shell (H_1) parameters	
R_{in}	$0.1^\circ, 0.2^\circ, 0.3^\circ, 0.4^\circ, 0.5^\circ, 0.6^\circ, 0.7^\circ, 0.8^\circ$
width w	$10^{-5} \times R_{\text{in}}, 0.1 \times R_{\text{in}}, 0.2 \times R_{\text{in}}$
Gaussian (H_0) parameters	
σ	$0^\circ, 0.05^\circ, 0.1^\circ, 0.2^\circ, 0.4^\circ$

Table 5.2: List of candidates from the search and "by eye" candidates: The sources are sorted by their HESS source identifier. The best model parameters for the Gaussian and the shell model is given together with the position in Galactic longitude and latitude and the maximum TS_{diff} . HESS J1458–608 and HESS J1908+063 did not show up in the search.

Name	l	b	σ	R_{in}	w	TS_{diff}
	[$^\circ$]	[$^\circ$]	[$^\circ$]	[$^\circ$]	[$^\circ$]	
HESS J1023–577	284.19	–0.40	0.2	0.2	$0.2 \cdot R_{\text{in}}$	24
HESS J1458–608	317.75	–1.70	-	-	-	-
HESS J1534–571	323.72	–0.90	0.2	0.3	$1 \times 10^{-5} \cdot R_{\text{in}}$	23
HESS J1614–518	331.41	–0.63	0.2	0.3	$0.2 \cdot R_{\text{in}}$	57
HESS J1908+063	40.39	–0.70	-	-	-	-
HESS J1912+101	44.45	–0.12	0.4	0.4	$1 \times 10^{-5} \cdot R_{\text{in}}$	50

In this case the amplitude Φ is the only free parameter. It can assume negative values corresponding to negative fluctuations in the background. By taking the sign of the amplitude negative significance is realized (H.E.S.S. Collaboration, 2018d).

For this search the goal was to find sources for which the shell model is preferred over a Gaussian model assumption. Hence, the Gaussian model is representing the null-hypothesis H_0 and the shell model the hypothesis H_1 that needs to be tested. The difference in TS between the two hypotheses was used as a measure on whether and how much H_1 is preferred over H_0 :

$$\Delta TS = TS_{H_1} - TS_{H_0} \quad (5.7)$$

For every grid position of the HGPS, the fit of the two models is done and the difference in TS , ΔTS , is filled into an empty sky map of the same size.

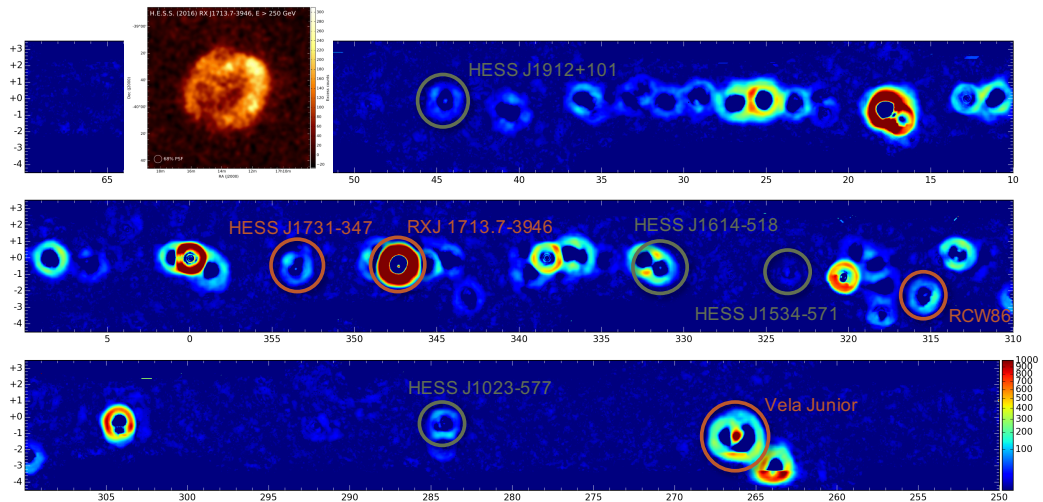


Figure 5.2: Difference in test statistics ΔTS , Shell versus Gaussian hypothesis: For every pixel in the HGPS the difference in TS between the best shell model H_1 and the best Gaussian model H_0 is plotted. For the parameter spaces shown in table 5.1, the parameters with the highest TS were chosen. In a ring around an emission region the shell model is picking up the emission as part of the modeled shell. Therefore, an excess in ΔTS is shown around all sources which is considered an artifact. If a source has a Gaussian morphology, the TS_{H_0} is larger than TS_{H_1} , therefore, a negative excess is seen at the center of the source. If the source is showing a shell-like morphology a peak in the center of the rings is seen due to $TS_{H_1} > TS_{H_0}$. Consequently the sky map is evaluated close to or at the centroid of significant emission (positions of the Gaussian components of the HGPS source catalog) for a ring artefact with a peak in the center. A prominent example of a young SNR with a shell morphology is RXJ 1713.7–3946 (H.E.S.S. Collaboration, 2018e), shown here with an orange circle. For comparison, a TeV sky map was put to the top left of the plot. The other orange circles are known shell SNRs, all of them with a clearly visible peak in the center (H.E.S.S. Collaboration, 2011, 2018b,c). The candidates emerging from this search are circled in green. A list of the candidates can be found in table 5.2, the already known sources in table 5.3.

5.2.3 Results

The resulting map was evaluated at the positions of known sources either at the published position of the known shell-like sources or at the positions of the HGPS catalog. Around an emission region the shell model is picking up the emission as part of the model and therefore creating a positive ΔTS . This in turn is creating a ring artifact around all sources independently of the morphology. In case of a source with a Gaus-

Table 5.3: List of known shell-like SNRs in the survey region: The sources are sorted by their HESS source identifier. The common name and maximum TS_{diff} are given in this table.

Name	Common name	TS_{diff}
HESS J0852–463	Vela Jr.	1778
HESS J1442–524	RCW 86	42
HESS J1713–397	RXJ 1713.7-3946	946
HESS J1731–347	-	68

sian morphology, the method creates negative values within the ring artifacts because the test statistics of the best Gaussian model at that position is better than the test statistics of the best shell model at the same position $TS_{\text{MaxShell}} < TS_{\text{MaxGauss}}$. If the source is shell-like, the ΔTS becomes significantly larger than 0 in the center of the ring artifact. Figure 5.2 shows the ΔTS -map covering the HGPS region. Orange circles are used to highlight the known TeV shells HESS J1731–347, RCW 86 and Vela Junior (H.E.S.S. Collaboration, 2011, 2018b,c). In the case of RXJ 1713.7–3946, in addition to the orange circle, the H.E.S.S. γ -ray excess sky map from H.E.S.S. Collaboration (2018e) is shown for a comparison. In addition to these four known sources that were expected to show up as positive results in the search, four candidates have been identified. A list of the candidates and the known sources can be found in table 5.2 and in table 5.3 including the ΔTS . In addition to the candidates from this search two other sources have been tested in the following source-by-source study. These sources are also listed in table 5.2.

The known sources with shell morphology have been reproduced with high significance, while for the shell candidates it is not straightforward to evaluate the significance of the shell detection. In either case it is important to understand what the limitations of this approach are:

- Only the two hypotheses, Gaussian and shell model, are fitted at the grid position while, apart from the background, the remaining emission is not modeled. The tested hypotheses might be biased towards the emission not modeled.
- The parameter space for the models is limited to save computing time.
- It is assumed that the center of the shell and the Gaussian model are at the same position to calculate the TS_{diff} . The Gaussian model might have a larger TS at a different position compared to the shell model.

These problems might lead to both, wrongly identified shell-like sources or sources that are missed. Especially in crowded regions it is likely that low significance cases are

overlooked. Another significant problem is that the models are compared at the same position. The Gaussian model might have a larger TS at a different position compared to the shell model. Therefore the ΔTS , which is basically a measurement of how much the shell is preferred over the Gaussian model, might be overestimated significantly. Because of the limited parameter space of the models and the other caveats, it was decided to test the four candidates and two sources suggested by colleagues in the collaboration on a source-by-source case instead of improving the search method and study the sensitivity and caveats further. The details of the source-by-source analysis are described in section 5.3.

5.3 Source-by-Source Analysis

In this section the analysis approach for the six candidates is described from selecting the observations to creating the high level maps for the morphology study. As mentioned in the introduction, only the results of three of the sources are shown. The advantages of using a dedicated data selection and analysis setting instead of working with the HGPS result is that the settings could be optimized to the sources of interest. For example more data have been included, partially because more data were taken after the dataset for the HGPS had been frozen. Furthermore, the requirement on the quality of the data for this study has been set to the standard settings for source detection instead of the stricter spectral quality cuts. These changes resulted in higher statistics in the γ -*candidate* map and the exposure on the source region became flatter compared to the HGPS sky-maps due to the additional data, the different quality cuts, and the larger run offset.

In addition the extraction of the energy spectra of the sources is discussed. In the last subsection the more general approach used for the morphology study is presented.

The author of this work was fully responsible for the input for the morphology study briefly described in section 5.3.3. The morphological study itself was led by another member of the task group.

All results presented here have been cross-checked with an independent calibration, simulation, and analysis framework (de Naurois & Rolland, 2009). This is a standard procedure of the H.E.S.S. collaboration.

5.3.1 Analysis of Available H.E.S.S. Data

5.3.1.1 Run Selection

As described in section 3.3.8 one observation run takes 28 min of observation time on a given position in the sky. During these 28 min it is assumed that the response of the instrument can well be represented by a constant function averaged over the observation parameters like the zenith angle. Since most of the sources described in this work have been observed as part of observations targeting other sources or survey observations, the exposure on and around a single sources is not homogeneous over the region of interest. Therefore, surface brightness maps in physical units are presented here which take the effective area into account and not, for example, simpler excess or significance maps. The error on the effective area look-ups created from simulations grows for large off-sets from the camera center, therefore a maximum run offset of 3.0° to the center of the source of interest was chosen. For the spectral analysis this offset was reduced to 1.5° . This is motivated by the limited statistics in the simulations for large offset events and the fact that small variations in the atmosphere or instrument parameters have an impact on the effective area. Furthermore, events with large offsets to the camera center are getting truncated, which has a negative impact on the reconstruction. In addition the canonical quality cuts for detection were applied as discussed by Aharonian et al. (2006b). Most notable from the criteria discussed by Aharonian et al. (2006b) is the stability of the array's trigger rate. Large variations in the trigger rate are an indication of bad weather or hardware problems. Furthermore, for the spectral analysis the expected trigger rate should not deviate much from the measured one. This is a measure of the optical transparency of the atmosphere. Since the publication of Aharonian et al. (2006b), the method has been updated: an optical transparency coefficient is now calculated based on the expected and measured trigger rates (Hahn et al., 2014). Only runs with optical transparency coefficients above 0.8 were taken into account for the spectral analysis. As an input for the run offset the position taken from the internal H.E.S.S. database was used. This database is either filled with the position used in the most recent publication or from the most recent study. Table 5.4 lists the number of runs and the total observation time on the sources for the morphology study. Table 5.5 shows the number of runs, and observation time used for the spectral analysis for the candidates confirmed by the dedicated morphology study. Please note that due to the dropping acceptance for larger offsets the actual exposure on the source is not reflected by the total observation time. An exposure time corrected for acceptance is calculated during the analysis. This number is quoted in the next section.

Table 5.4: Number of observation runs and observation time: For the search for observations the position of the H.E.S.S. database was used. All observation runs within 3.0° are taken into account.

Name	Number of runs	Observation time
HESS J1534–571	156	49.09 h
HESS J1614–518	87	39.33 h
HESS J1912+101	291	130.10 h

Table 5.5: Number of observation runs and observation time: For the search for observations the position of the database H.E.S.S. database was used. All observation runs within 1.5° are taken into account.

Name	Number of runs	Observation time
HESS J1534–571	69	30.83 h
HESS J1614–518	33	14.32 h
HESS J1912+101	189	84.13 h

5.3.1.2 Event Reconstruction and γ /hadron Separation

The first step in the event reconstruction is the image cleaning as described in section 3.3.9. In this case a standard 5 pe, 10 pe image cleaning was used, which means that a pixel has to be above a threshold of 5 photo-electrons and at least one neighboring pixel above 10 photo-electrons. This removes pixels that mainly contain night sky background and electronic noise. After image cleaning the Cherenkov showers can be parametrized as an ellipse. The parameters used here are called Hillas parameters following Hillas (1985), namely the length, the width, distance to the camera center, and the image amplitude of the shower. A detailed description can be found in section 3.3.9. The image amplitude of the shower is corrected using the so-called muon correction. Muons create a ring on the PMT-cameras of the telescopes. The light seen in the camera comes from only one particle. The radius of the image of the Cherenkov cone is directly correlated to the energy of the muon. When simulating those muons with the instrument response there is a measure of the expected light in the ring in relation to the energy that can be obtained. By dividing the expected light by the measured light, a muon correction factor is calculated. The small differences between the simulated instrument and the real instrument can be corrected by applying this factor to the image amplitude. This correction factor is usually of the order of 1 ± 0.05 (Bolz, 2004). A few runs from the very beginning of the experiment had to be excluded because no calibration phase with fitting optical efficiencies was available. The observations are grouped into a number of muon phases. One muon phase usually lasts for 6 to 12 months or up to a major hardware change. For a muon phase, simulations are done with a fixed

optical efficiency to create the look-up tables for various parameters like effective areas or the psf. Remaining differences are corrected with the muon correction factor. This was discovered due to a muon correction larger than expected. An issue with the muon correction is that it only shifts the instrument response function in the effective area. A grossly wrong optical efficiency also changes the shape of the function. The muon correction should not exceed 10%⁸.

Depending on the aim of the analysis, a cut on the image amplitude is applied. For the morphology study presented here a cut of 160 pe is used. This cut is optimized for point sources with a presumed hard spectrum with an index of around $\Gamma = 2.3$ and a flux of around 10% of the flux of the Crab Nebula. This pulsar wind nebula is the brightest steady source at 1 TeV. It is worth mentioning that a variable flux has been reported for this source in other wavebands, but so far not at TeV-energies. Another side effect of this cut set is an improved angular resolution of the analysis and a more powerful γ /hadron separation compared to the standard cut set which is more sensitive to softer sources and offers a lower energy threshold. The resulting energy threshold of the analysis cut for hard sources increases the energy threshold of this analysis to ~ 500 GeV. As described in section 3.3.9, in hadronic EAS the secondary showers widen the image of the EAS compared to electromagnetic EAS where the light distribution is narrower. When filtering out low energy showers by applying the cut on the image amplitude, more pixels participate in one shower which makes it easier to distinguish electromagnetic from hadronic showers. For the spectral analysis of HESS J1534–571 and HESS J1614–518 the cut was reduced to 60 pe to lower the energy threshold. For HESS J1912–101 this was not possible due to systematic effects in the background determinations. Details are discussed in section 5.3.4.

After the parametrization of the shower, a separation of electromagnetic and hadronic showers is done. This is achieved by using BDTs following the description of Ohm et al. (2009). A parameter ζ based on the mean scaled width of the showers is derived. A cut on this value is applied which discards most of the hadronic events. The remaining events are classified as γ -candidates which still contain a fraction of hadronic events and also events induced by leptons which can not be distinguished from events induced by γ -rays. For the reconstruction the information two or more telescopes are taken into account⁹. As described in section 3.3.9, the Hillas parameterization provides a direction reconstruction for a single shower. To reduce the error on the direction reconstruction and also to improve the energy reconstruction, only events with at least two telescope images are reconstructed. In fact, events from the 12m telescopes are only recorded

⁸Private communication with the calibration expert V. Marandon

⁹Although at least three telescopes participate in the observation runs for this analysis, some events are only present in two telescopes

when two telescopes trigger at the same time (section 3.3.5). The intersection of the major axis of the showers' images provides a more accurate direction reconstruction compared to a monoscopic reconstruction. In addition, hardware problems in a single telescope are less problematic because the image in the second telescope often is in a good shape. The resulting direction reconstruction is filled into a 2D histogram in sky coordinates, the so called ON map or γ -*candidate map*. The binning of this map is adjustable. For this study a binning of $0.01^\circ \times 0.01^\circ$ was used.

5.3.2 Sky Maps

5.3.2.1 Low Level Maps

For every run the instrument response is evaluated using look-up tables generated with Monte Carlo simulations (for γ -rays) with matching instrument parameters and from extragalactic AGN observations where the point source is masked (for the background acceptance). A map with the radial acceptance for background events, the so-called *OnExposure map*, and a map with the exposure for γ -rays is filled from the look-up tables with matching observation parameters. Details on the instrument response are described in section 3.3.7.

Under ideal conditions, the background could be derived from the background acceptance map (*OnExposure map*) so that all information is available to create high-level maps such as surface brightness maps. Since the observations from which the background acceptance was taken are not identical to the observation runs analyzed, the acceptance is assumed to be radially symmetric, and sub-threshold sources might contribute to a diffuse γ -ray background, the background is determined in a different way, for example with the Ring Background method following Berge et al. (2007). The method has been refined using an adaptive ring size to estimate the background for complex regions with extensive exclusion regions (H.E.S.S. Collaboration, 2018d). A description of the method can be found in section 3.3.10. The basic idea is that around each pixel a ring is placed. Taking into account exclusion regions that mask known γ -ray emission, the counts within the ring on the γ -*candidate map* is summed up and filled into a new map at the position of the center of the ring. This map is called *OFF map*. At the same time, the ratio of the background acceptance (OnExposure) of the pixel in the center and the background acceptance of the ring (OffExposure) is filled into a map called *Alpha map*:

$$\alpha_i = \frac{\text{ONExposure}_i}{\text{OFFExposure}_i}. \quad (5.8)$$

The product of *Alpha map* and the *OFF map* provides a *Background map*:

$$Bkg_i = \alpha_i OFF_i. \quad (5.9)$$

The γ -ray excess is calculated as:

$$Excess_i = ON_i - Bkg_i. \quad (5.10)$$

In addition to these basic maps an expected γ -ray map is filled (*ExpGammaMap*). This map contains the number of expected γ -rays for a certain energy range assuming a power law:

$$\Phi_{\text{ref}}(E) = \Phi_0(E/E_0)^{-\Gamma} \quad (5.11)$$

with an index of $\Gamma = 2.3$ and a normalization of $\Phi_0 = 1 \text{ TeV}^{-1} \text{ m}^{-2} \text{ s}^{-1}$. Using this, the number of expected counts is calculated based on the effective Area A_{eff} obtained from Monte Carlo simulations and the duration of the run as:

$$N_{\text{exp}} = \sum_{\text{Reruns}} T_{\text{R}} \int_{E_{\text{min}}}^{\infty} \Phi_{\text{ref}}(E_{\text{rec}}) A_{\text{eff}}(E_{\text{rec}}, q_{\text{R}}) dE_{\text{r}}. \quad (5.12)$$

The effective area A_{eff} depends on the reconstructed energy E_{rec} and the observation parameters q_{R} (zenith angle, distance to the center of the field of view and azimuth angle, participating telescopes, and optical efficiency). The integral has to be scaled to the observation time and is therefore multiplied with the run duration T_{R} . The minimum energy E_{min} is the energy threshold of the observation run which is defined by a maximum energy bias in the reconstruction of 10 %. This energy is derived from simulations as well. N_{exp} is calculated for each position in the sky. This map is later used for the morphology fitting as exposure and to calculate a surface brightness for different regions in the sky.

5.3.2.2 Sanity Check

To verify the integrity of the maps, a set of checks were done. The significance of the emission is tested using Equation 17 of Li & Ma (1983). This calculation is suitable for low numbers of counts. This was done for the entire map summing up the ON-counts, OFF-counts, and Alpha within a correlation radius R . In this case a correlation radius

of 0.1° was chosen. This value is slightly larger than the typical psf of the instrument (0.07°) and hereby ensures a reasonable number of ON-counts for the significance calculation. Another test that can be done with this map is applying masks to exclude known emission regions in the field of view and then check for hot-spots in the map. Such hot-spots either point to a problem with the analysis or to emission regions not masked. When looking at the distribution of significance entries from the background regions (significance map with exclusion regions), the distribution should follow a normal distribution with a mean of 0 and a width of 1. These three significance plots are shown in figure 5.3 for all four sources. On the y-axis of the significance distribution a logarithmic scale is used, which visualizes even small deviations from a normal distribution plotted as a red curve. As a final check a Gauss function defined as:

$$f(x) = \frac{1}{\sqrt{2\pi\sigma^2}} e^{-\frac{(x-\mu)^2}{2\sigma^2}} \quad (5.13)$$

with μ being the mean of the distribution and σ being the standard deviation has been fitted to the background distribution. The results are shown in table 5.6. The fit results are close to a perfect distribution, deviations can be caused by hardware problems and/or insufficient exclusion regions. If the latter are chosen too big, the uncertainty of the background estimation increases until no background regions are available anymore. While the results show a slight deviation from a perfect normal distribution, the exclusion regions used here are in a good balance between available background regions to create a background map and masking most of the emission regions.

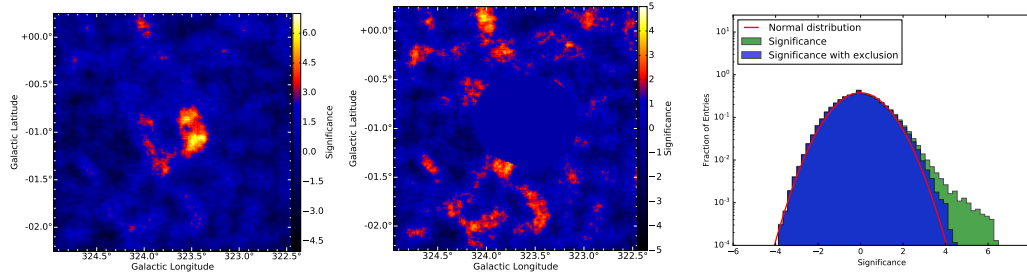
Table 5.7 summarizes the statistics for a test region placed at the source position with an extent that fully encloses the source. The test region was defined according to the HGPS pipeline results. All the sources are detected significantly between 9 and 25σ over the background. Also the background control regions for these evaluations are at least 3 times larger than the area of the test region. The lower livetime compared to the observation time listed in table 5.4 originates from the fact that the livetime is corrected for the dropping acceptance of larger run offsets.

5.3.3 Morphology Study

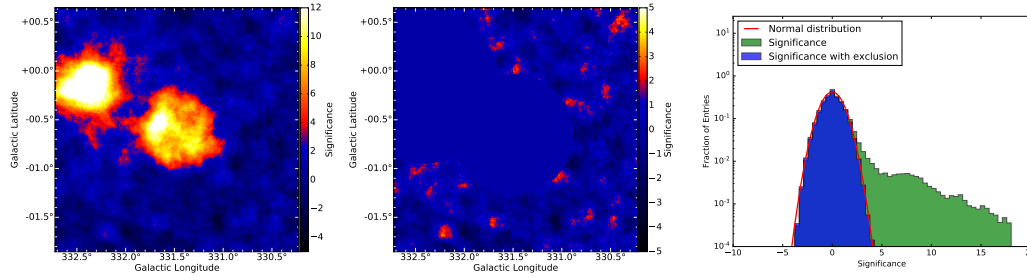
5.3.3.1 Model Comparison

For the morphology study, a shell model, defined as a sphere emitting homogeneously between R_{in} and R_{out} projected to two dimension (c.f. equation 5.2), is compared to a Gaussian model (c.f. equation 5.1). In contrast to the shell search as described in section

HESS J1534–571



HESS J1614–518



HESS J1912+101

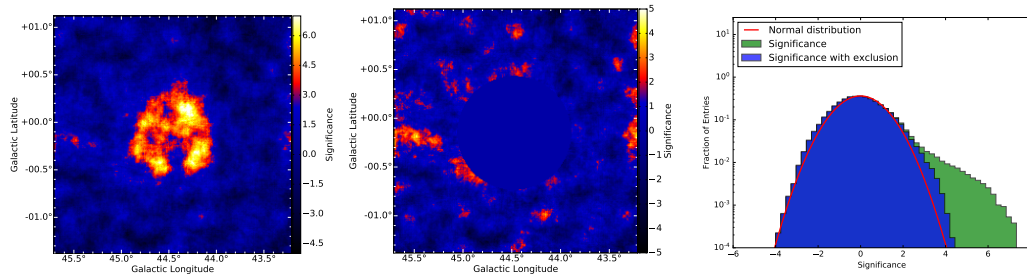


Figure 5.3: Significance maps: From top to bottom the three candidates that emerged from the systematic search on the HGPS are shown. On the left a significance map is shown followed by a significance map with exclusion regions. The plots on the right show a distribution of these two maps compared to a normal distribution. The significance is calculated on the low-level data within a correlation radius of 0.1° per pixel using Equation 17 of Li & Ma (1983).

5.2.2, all parameters can vary freely during the fit, as a set of starting parameters a best guess was used. The modeling of background and signal as well as the statistical methods described in section 5.2.2 were used. For HESS J1534–571 and HESS J1912–101 only the shell model and the Gaussian model were tested.

In the case of HESS J1614–518, an additional Gaussian component had to be added to account for the neighboring source HESS J1616–508 (c.f. Aharonian et al., 2006c). Even then, a clear excess was visible in the residuals at the position of the bright

Table 5.6: Fit parameter to the significance with exclusion distribution: A Gaussian distribution has been fitted to the distribution of significance with exclusion shown in figure 5.3. For a Poissonian background, which should be the case here, the distribution should have a mean of 0 and a width of 1. Deviations to that indicate insufficient exclusion regions and/or hardware problems. Considering the complex region around HESS J1534–571 and around HESS J1912+101 the results are acceptable.

Source	Fitted mean	Fitted standard deviation
HESS J1534–571	-0.02 ± 0.32	1.05 ± 0.21
HESS J1614–518	$\pm 0.00 \pm 0.30$	1.00 ± 0.21
HESS J1912+101	-0.04 ± 0.33	1.10 ± 0.20

Table 5.7: Acceptance-corrected livetime and statistics: In this table the acceptance-corrected livetime calculated during event reconstruction, the total number of ON, OFF and Excess counts within a test region, the ratio of test region size to background region size called α , the signal to background ratio, and the significance of the emission within the test region (Equation 17 of Li & Ma (1983)) are shown. The test region is a circle, its position and size was chosen based on the HGPS results.

Source	Livetime	ON	OFF	α	Excess	S/B	σ
HESS J1534–571	61.8 h	2549	11084	0.19	479.0	0.23	9.3
HESS J1614–518	34.2 h	2570	4003	0.33	1236.6	0.93	25.2
HESS J1912+101	121.1 h	9149	24373	0.30	1779.6	0.24	17.3

part of HESS J1614–518 towards HESS J1616–508 after the fit. It was tested whether another Gaussian model would counter the effect, but it led to an only marginally improved test statistic. Furthermore, the results for the additional component (position, extend, and amplitude) could not be reproduced in the cross-check analysis, even though also some not modeled residuals are visible when modeling HESS J1614–518 with only a shell model. Hence, the additional Gaussian component has not been explored further. To model the region of interest around HESS J1614–518, a shell model for HESS J1614–518, and a Gaussian model for HESS J1616–508 was used.

As described in section 5.2.2 the difference in test statistic is a measure of the quality of one model compared to the other. This difference behaves asymptotically like a χ^2 distribution. Even so, one has to be careful because this is not true for border cases as stated by Eadie (1971). Consequently the theorem can only be applied for nested models in which the continuous variation of one parameter leads from the hypothesis to the null-hypothesis. For the models compared here, this is not the case. Thus a likelihood ratio test (LRT) can not be applied (Wilks, 1938). This is a purely numerical problem, a higher TS of the hypothesis still means it is better compared to the null-

hypothesis, but the power of this improvement is unclear. Therefore the Akaike criteria (Akaike, 1974) was applied which is defined as:

$$AIC = 2k - 2 \ln (\mathcal{L}_{ML}) \quad (5.14)$$

where k is the number of parameters and \mathcal{L}_{ML} the maximum likelihood value for that model. In consequence to test a model against another model, following Burnham & Anderson (2013), a relative strength of a model i against the best available model can be calculated as:

$$\mathcal{L}_{AIC,i} = C \cdot \exp \left(-\frac{AIC_i - AIC_{\min}}{2} \right). \quad (5.15)$$

To test how this value relates to the probability that the preference of the shell model over the Gaussian model is not caused by statistical fluctuations, a limited set of simulations was done using the parameters retrieved from HESS J1534–571. The calculated relative strength behaves like a statistical probability. For a detailed description see H.E.S.S. Collaboration (2018a). The results of the three sources are shown in table 5.8. Even though HESS J1534–571 is the source with the highest probability of $\mathcal{L}_{AIC,H_0} = 5.9 \times 10^{-3}$ that the finding is due to fluctuations, as shown in section 5.4.1.1, at the source position a radio SNR candidate is found with a good morphology match to this source. For the other two sources the statistical probability that they are shell-like is much higher. At this point in the study these three sources are classified as SNR candidates from the VHE information alone. This is the first successful attempt to classify unidentified VHE sources as SNR candidates.

5.3.3.2 Azimuthal and Radial Profiles

To verify the morphological results shown here and to quantify possible deviations, azimuthal and radial profiles of the sources were derived. For the azimuthal profile the sources have been divided into eight wedges. The first wedge is centered at $\Theta = 0$ which corresponds to the direction of positive Galactic latitude. Following wedges are placed counterclockwise. As outer radius, the R_{out} of the best fit was used and the center of the sources was masked with a circle with a radius slightly smaller than R_{in} . This was done to focus on the bright part of the shell which extends further in than R_{in} because of the projection of the three-dimensional sphere onto two dimensions. The optimization was done ad hoc on the radial profiles.

Table 5.8: Results of the morphology study of the three significant candidates: For all sources the discovery status (^a) is listed. HESS J1534–571 is a special case because the source has no peer reviewed paper yet, therefore, the results of the HGPS pipeline is shown. In addition the source detection significance (^b) inside R_{out} , following Li & Ma (1983), is listed. $\mathcal{L}_{\text{AIC},H_0}$ (^c) gives a measure whether the fit improvement of the shell (H_1) over the Gaussian (H_0) is due to fluctuations using the *Akaike Information Criterion*. Please note that this is not the probability for the source over a background. The best fit parameters are given in Galactic longitude l and latitude b , in addition the inner and outer radius of the shell is shown (^d).

	HESS J1534–571	HESS J1614–518	HESS J1912+101
Discovery ^a	$TS_{\text{diff}} = 39$	(1)	(2)
Excess ^b	9.3σ	25.2σ	17.3σ
$\mathcal{L}_{\text{AIC},H_0}$ ^c	5.9×10^{-3}	3.1×10^{-6}	1.7×10^{-6}
l_0 ^d	$323.70^{+0.02^\circ}_{-0.02^\circ}$	$331.47^{+0.01^\circ}_{-0.01^\circ}$	$44.46^{+0.02^\circ}_{-0.01^\circ}$
b_0 ^d	$-1.02^{+0.03^\circ}_{-0.02^\circ}$	$-0.60^{+0.01^\circ}_{-0.01^\circ}$	$-0.13^{+0.02^\circ}_{-0.02^\circ}$
R_{in} ^d	$0.28^{+0.06^\circ}_{-0.03^\circ}$	$0.18^{+0.02^\circ}_{-0.02^\circ}$	$0.32^{+0.02^\circ}_{-0.03^\circ}$
R_{out} ^d	$0.40^{+0.04^\circ}_{-0.12^\circ}$	$0.42^{+0.01^\circ}_{-0.01^\circ}$	$0.49^{+0.04^\circ}_{-0.03^\circ}$

References. (1) Aharonian et al. (2006c); (2) Aharonian et al. (2008a).

A surface brightness was calculated using the number of measured excess divided by the area of the wedge A and the number of expected counts following Equation 5.12. This value was weighted with the integral of a reference spectrum between 1 TeV and infinity, in this case a power law with an index of $\Gamma = 2.3$ and a normalization of $\Phi_0 = 1 \text{ TeV}^{-1} \text{ m}^{-2} \text{ s}^{-1}$. The normalization is the same used in the definition of N_{exp} (c.f. Equation 5.12) and therefore cancels out. It is important to note that even though the integrated surface brightness is shown from 1 TeV, the entire number of excess counts is taken into account to weight the reference spectrum:

$$S = \frac{N_\gamma}{N_{\text{exp}}} \int_{1 \text{ TeV}}^{\infty} \Phi_{\text{ref}}(E) dE \cdot \frac{1}{A} \quad (5.16)$$

As already visible in the significance sky maps, the azimuthal profile of HESS J1534–571 shows a positive trend towards top right, the profile of HESS J1614–518 shows a bipolar structure whereas HESS J1912–101 is flat. A constant has been fitted to the profiles and a probability has been calculated as to how much the sources deviate

from a flat distribution. The deviations are not significant for HESS J1534–571 and HESS J1912–101. For HESS J1614–518, the azimuthal profile is significantly different from a flat distribution. The azimuthal profiles were not only created from real data, but also from the fitted 2D models. To achieve that, a sky map from the model was calculated and the same wedges were applied, the resulting two profiles per source are shown in figure 5.4. This is also a good test for how much HESS J1616–508 is contaminating HESS J1614–518, a factor that can become relevant in the spectral analysis. Whereas for HESS J1534–571 and HESS J1912–101 the model curve is completely flat, as expected from the mathematical definition, a marginal excess is visible for HESS J1614–518 towards HESS J1616–508 though the effect is negligible for the subsequent studies.

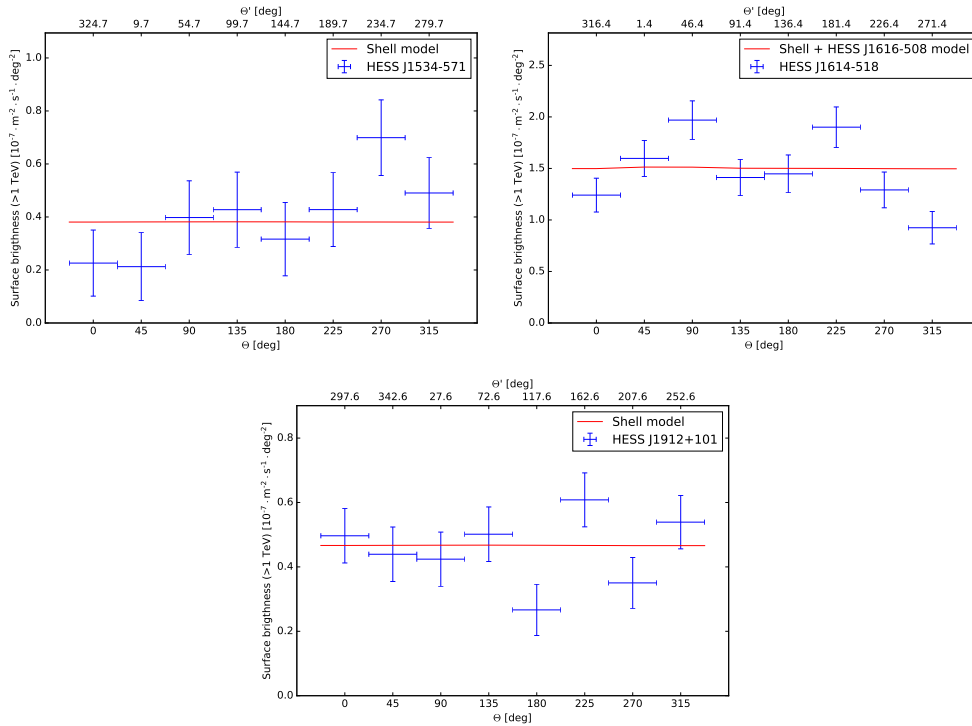


Figure 5.4: Azimuthal profiles for HESS J1534–571, HESS J1614–518, and HESS J1912+101: To derive the profiles, the sources were divided into eight wedges of equal size with outer radius R_{out} and inner radius smaller than R_{in} to focus on the bright emission. Θ is the angle with respect to the Galactic latitude. The first wedge is at $\Theta = 0^\circ$, following wedges are added counter-clockwise. Θ' is the angle with respect to North in equatorial coordinates. From the fitted models, maps were created and the profiles were extracted. The models are shown in red. As expected the models are azimuthally flat with the exception of HESS J1614–518, where a small excess towards HESS J1616–508, modeled as a Gaussian component, is visible.

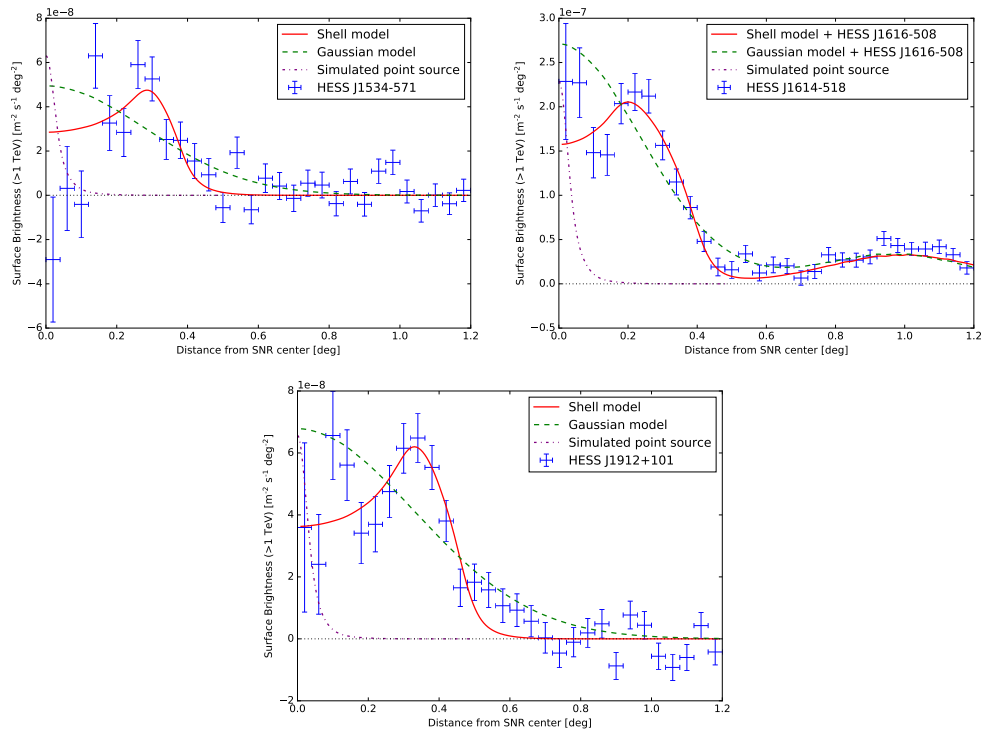


Figure 5.5: Radial profiles for HESS J1534–571, HESS J1614–518, and HESS J1912+101: To derive the profiles, the surface brightness was calculated for radial annuli around the best fit position of the shell model with a width of 0.04° . The same was done for the shell model and the Gaussian model, but with a finer annulus size. A continuous line was drawn through the data points. The simulated point source was normalized to the maximum of the radial profile of the data. In the case of HESS J1614–518, HESS J1616–508 is clearly visible in the data, the shell model, and the Gaussian model. For all three sources, visually, the shell model agrees best with the data.

Using the same approach, radial profiles were calculated for the data, the best shell model, and a simulated point source. Note that the profiles have been normalized to the maximum of the radial profile of the data. The annuli are centered around the best fit position of the shell model and have a width of 0.04° on the data. For the models a finer annulus size has been used and a continuous line was drawn through the data points. HESS J1614–518 is a special case because both the Gaussian model and the shell model contain a second component, namely HESS J1616–508 which is clearly visible in the data as well as in the Gaussian model and in the shell model. In all three cases, the shell model agrees better with the data than the Gaussian model. The results are shown in figure 5.5.

Table 5.9: Acceptance-corrected observation time for the spectral analysis.

Name	Observation time
HESS J1534–571	25.4 h
HESS J1614–518	10.0 h
HESS J1912+101	43.2 h

5.3.4 Spectral Analysis

The spectral analysis was also done for the firmly identified SNR candidates only. To reduce systematic errors caused by large event offsets, for the run selection the offset of the pointing position to the center of the sources was reduced to 1.5° . This ensures that the event offset in the analysis is not much larger than 2° . The maximum event offset consists of run offset plus the radius of the extraction region. In addition, stricter cuts on the data quality were applied, mainly the atmosphere’s transparency coefficient ($0.8 < c < 1.2$), the number of broken pixels (< 120), and the trigger rate fluctuation. Applying these cuts, the available observation time shrinks to the numbers listed in table 5.5 (Aharonian et al., 2006b; Hahn et al., 2014).

The extraction region was defined as $R_{\text{out}} + R_{68\%}$ where $R_{68\%}$ is the 68 % containment radius of the psf. This ensures that almost all events are within the test region.

For the background determination, reflected background regions have been used (Berge et al., 2007). One or more background regions, identical to the test region, are placed with the same offset to the observation position. The number of background regions is determined automatically depending on the available space. The background regions cannot overlap with the exclusion region that masks significant excess. Also the test region cannot overlap with the pointing position of the telescope. One effect of this background technique is that observation runs are discarded if no background regions can be placed. This happens when the pointing position overlaps with the test region or if no background region can be placed because of large exclusion regions. Because of this, almost 50 % of the observation runs passing quality cuts had to be discarded for HESS J1912+101. Table 5.9 lists the acceptance-corrected observation time. That is the observation time after observation runs were discarded because of insufficient background region and the remaining observations were dead-time-corrected as well as corrected for acceptance change depending on the off-optical axis angle and normalized to a standard offset of 0.5° .

Since the acceptance of the instrument is radially symmetric, the test region and the background regions have the same instrument response. In contrast to a point source analysis where typically (for an event offset of 0.5°) at least five background regions can

be placed, the spectral analyses of these sources suffer from the problem that the test region is large (radius larger than 0.5°) with a mean run offset of about 0.7° . This, combined with the large exclusion regions within the Galactic plane, leads to a ratio of test region over background region of almost only one. Therefore, besides the reduction of background statistics, the background determination suffers from increased systematic uncertainties compared to a standard point source analysis. For larger event offsets, the background determination also suffers from another problem: While to first order the assumption is allowed that the response of the instrument is radially symmetric, second order effects exist. To counteract this, observations are usually taken in a so called wobble strategy: The observations are taken in alternating declination and right ascension offsets to cancel out this effect. The observation strategy for the three sources was not optimized in this way because the runs were partially taken as survey observations or focused on another near-by source. Furthermore, the best-fit positions of the sources differ significantly from the discovery position, especially for HESS J1534–571 and HESS J1912–101. In a few cases the observation position overlapped with the test region of the spectral analysis.

To understand the systematic effects of this analysis, the analysis was repeated with different analysis cuts. This included changes in the size of the test region, the image amplitude cut and a stricter run selection. Also results from a cross-check analysis were taken into account. These tests led to the following conclusions:

- For a power-law model (see equation 5.17) the systematic error was estimated to be $\Gamma = 0.2$ and 30% on the flux normalization N_0 .
- For the spectral analysis of HESS J1912–101 a stricter cut on the image amplitude was adopted.

Aharonian et al. (2006b) estimated the error of a standard H.E.S.S. analysis to be 0.1 on the index and 20% on the flux normalization. This estimate was based on a study of multi-year H.E.S.S. observations on the Crab Nebula. It was mainly driven by run-by-run variability, but also by the accuracy of the Monte Carlo simulations. Also the Background estimation was discussed, but the impacts were considered to be minor, due to the fact that the wobble strategy cancels out most of the effects. Since this is not true for these analyses, the estimate seems to be reasonable. Independent from this study, task groups for other publications of extended sources for example in the HGPS (H.E.S.S. Collaboration, 2018d) or in the case of RX J1713.7–3946 (H.E.S.S. Collaboration, 2018e) adopted a systematic uncertainty of 30% on the flux normalization and 0.2 on the index after studying the uncertainty in the background estimation.

HESS J1912–101 is a special case. It is a very faint source with a flux of roughly 10 % of the flux of the Crab Nebula (Meyer et al., 2010), but spread out over an area of 1.9 deg^2 (for comparison the moon has an apparent area in the sky of 1.5 deg^2). The outer radius of the fitted shell model of HESS J1912–101 is 20 % larger compared to the other two sources. This makes the source one of the faintest sources detected with H.E.S.S. in terms of surface brightness. To complicate the spectral analysis further, the sky region is very complex which leads to very large exclusion regions. In addition, the data was taken over almost all periods of the experiment. Applying the same procedure used for the other two sources led to an unstable spectral result: Close to the threshold of the analysis the emission drops to zero which is hard to justify from a physical point of view, it was not seen in the cross-check analysis with a similar threshold, and the energy of the break depended on settings like the size of the exclusion regions and limiting the data set to runs that were taken in the correct wobble offset strategy. Although many attempts were made to understand this effect, no firm conclusion was reached. The most probable explanation is that the background estimation is contaminated by diffuse emission or emission from unresolved sources. This also explains why the cross-check analysis did not have the same problem because it is less sensitive to diffuse emission. In conclusion, the analysis cuts for HESS J1912–101, especially the image amplitude cut, remained at the level used for the morphology study to reduce errors on the background estimation. This leads to a higher threshold in the analysis compared to the other two sources.

The spectral fitting was done on the *ON*- and *OFF*-data separately taking into account the instrument response. To achieve this, the data and the instrument response were filled run-wise into a histogram with 25 bins per energy decade. For this forward folding fit, a likelihood maximization was used. The models tested are a power-law model defined as:

$$\frac{dN}{dE} = N_0 \left(\frac{E}{E_0} \right)^{-\Gamma} \quad (5.17)$$

and an exponential cut-off power-law model defined as:

$$\frac{dN}{dE} = N_0 \left(\frac{E}{E_0} \right)^{-\Gamma} \exp(-\lambda E). \quad (5.18)$$

In both models E stands for the energy, N for the number of counts, N_0 is the normalization at E_0 which is the pivot energy where N_0 and Γ are least correlated, and Γ is the spectral index. The parameter λ is defined as $\frac{1}{E_{\text{cut}}}$ and defines the cut-off energy E_{cut} . A LRT was done for the two models and the three different sources, the

exponential cut-off power law is preferred with 3σ to 4σ for HESS J1614–518 and HESS J1912–101. The large systematic errors also affect the curvature parameters. In particular when the effective areas for high energies exhibit a small error, the impact on the curvature of the spectrum is significant. For HESS J1912–101 the preference for the exponential cut-off power law could not be confirmed by the cross-check. We adopted the threshold of $TS \geq 16$ (equivalent to 4σ) used by the *Fermi*-LAT for their catalogs (e.g. Ackermann et al., 2016). Therefore, in table 5.10 only the results of the power-law model is quoted.

Table 5.10: Spectral fit results from the power-law fits to the H.E.S.S. data: Both statistical and systematic errors are given for the fit parameters. The systematic uncertainties result from deviations from the nominal parameters of the simulations of the instrument, non-optimized observation strategy, and the large size of the sources which lead to substantial susceptibility of the spectral results to potential errors in the background estimation. For source comparison the normalization at 1 TeV, $N_{0,1 \text{ TeV}}$, and the energy flux from 1 TeV to 10 TeV are given as well.

Source	E_{\min} [TeV]	E_0 [TeV]	N_0 [$\text{cm}^{-1} \text{s}^{-2} \text{TeV}^{-1}$]	Γ
J1534–571	0.42	1.40	$(1.29 \pm 0.12_{\text{stat}} \pm 0.39_{\text{syst}}) \times 10^{-12}$	$2.51 \pm 0.09_{\text{stat}} \pm 0.20_{\text{syst}}$
J1614–518	0.32	1.15	$(5.86 \pm 0.34_{\text{stat}} \pm 1.76_{\text{syst}}) \times 10^{-12}$	$2.42 \pm 0.06_{\text{stat}} \pm 0.20_{\text{syst}}$
J1912+101	0.68	2.25	$(4.82 \pm 0.43_{\text{stat}} \pm 1.45_{\text{syst}}) \times 10^{-13}$	$2.56 \pm 0.09_{\text{stat}} \pm 0.20_{\text{syst}}$

Source	$N_{0,1 \text{ TeV}}$ [$\text{cm}^{-1} \text{s}^{-2} \text{TeV}^{-1}$]	energy flux (1 – 10 TeV) [$\text{erg cm}^{-1} \text{s}^{-2}$]
J1534–571	$(2.99 \pm 0.30_{\text{stat}} \pm 0.90_{\text{syst}}) \times 10^{-12}$	$(6.5 \pm 0.7_{\text{stat}} \pm 2.0_{\text{syst}}) \times 10^{-12}$
J1614–518	$(8.33 \pm 0.49_{\text{stat}} \pm 2.50_{\text{syst}}) \times 10^{-12}$	$(2.0 \pm 0.2_{\text{stat}} \pm 0.6_{\text{syst}}) \times 10^{-11}$
J1912+101	$(3.89 \pm 0.45_{\text{stat}} \pm 1.17_{\text{syst}}) \times 10^{-12}$	$(8.1 \pm 0.7_{\text{stat}} \pm 2.4_{\text{syst}}) \times 10^{-12}$

To represent the spectra an adaptive rebinning was used to reach 2σ per bin. The spectra are plotted in a SED representation in figure 5.6.

5.4 Search for Multi-Wavelength Counterparts

Although all sources exhibit a shell-like structure and a spectrum that is in good agreement with the interpretation as a SNR, there are other possible explanations. The spectra themselves are typical for almost every Galactic VHE source and do not constrain the nature of the sources. The shell-like morphology is a much stronger indication, but

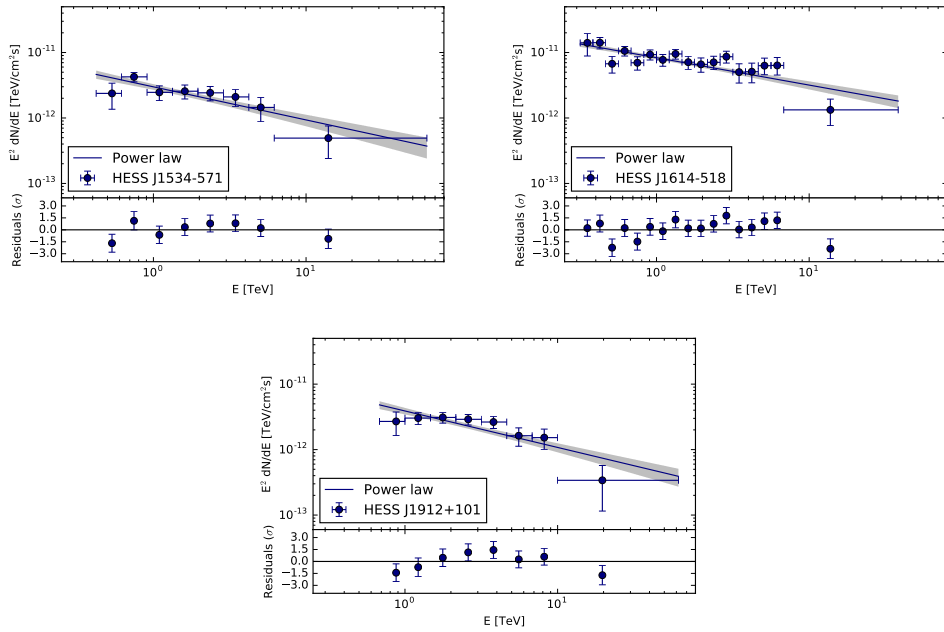


Figure 5.6: Flux points and power-law models with H.E.S.S.: The upper boxes show the H.E.S.S. energy flux spectra of HESS J1534–571, HESS J1614–518, and HESS J1912+101 (blue data points with 1σ statistical uncertainties), respectively. The bin size is determined by the requirement of at least 2σ significance per bin. The solid blue lines with grey butterflies (1σ error of the fit) show the best fit power law models from table 5.10. The bottom boxes show the deviation from the respective model in units of sigma, calculated as $(F - F_{\text{model}})/\sigma_F$. Systematic uncertainties do not permit the application of more complex models to describe the data. (Plots taken from H.E.S.S. Collaboration (2018a).)

there are other explanation like a super-bubble in which a series of supernova explosions have formed a common bubble. Emission in the TeV band from one representative of this source class was detected recently in the LMC (H.E.S.S. Collaboration, 2015). Another explanation that should not be underestimated is source confusion. Although great care was taken in the morphology study, it can not be neglected.

A search in all relevant MWL catalogs was performed and the surroundings of the candidates were studied using radio surveys. In addition, X-ray observations with *Suzaku* and *XMM-Newton* were analyzed.

The MWL studies were performed by a large team within the H.E.S.S. collaboration. In the following, all results are briefly summarized, for more details see H.E.S.S. Collaboration (2018a). Special emphasis is given to contributions of the author of this thesis, especially the radio continuum emission in the direction of HESS J1534–571, the GeV emission measured with *Fermi-LAT* in the direction of HESS J1614–518, and

the pulsar wind nebula scenario for HESS J1912+101. At the beginning of each section, a surface brightness map of the respective source is presented together with the associations found. The surface brightness maps were created following the approach outlined in section 5.3.3.2. Following the equations presented there, the surface brightness is calculated for each pixel in the sky map using a correlation radius of 0.1° ; a mild smoothing with a Gaussian function with a kernel size of 0.01° was applied as well. The resulting maps are corrected for the exposure for γ -rays and the surface brightness is given in physical units. The color scale is truncated excluding negative entries from the dynamic range.

5.4.1 HESS J1534–571

5.4.1.1 Radio Continuum Emission

RX J1713.7–3946 and RX J0852.0-4622 (Vela Jr.) are bright non-thermal X-ray and TeV-emitting SNRs with a shell-like morphology having only a weak radio counterpart (c.f. e.g. Dubner & Giacani, 2015). Since the radio counterparts might have a very low surface brightness, it is possible that Galactic background variations and confusion with thermal emission may prevent the detection of radio counterparts for the new SNR candidates. Publicly available radio catalogs and surveys were investigated for all candidates, but only for HESS J1534–571 a counterpart was found. From the Second Epoch Molonglo Galactic Plane Survey (Murphy et al., 2007), Green et al. (2014) published a catalog of new SNR candidates including the candidate G323.7–1.0. The survey was done at a frequency of 843 MHz and a beam size of $45'' \times 45'' \cos \text{sec}|\delta|$ where δ is the declination (Green et al., 2014).

As seen in Fig. 5.7 the radio data (right panel) reveals a very weak source with a morphology similar to HESS J1534–571. On the TeV surface brightness map (left panel), the outer boundaries and the position of G323.7–1.0 is plotted in green following the description in Green et al. (2014). The position angle was not available from the publication and was derived from the radio map manually. The sources match very well. To not only compare position and extent but also the shape of the emission on a qualitative level, profiles from both the TeV emission and the radio emission were extracted and compared. Since the best fit position of HESS J1534–571 and G323.7–1.0 are in agreement within statistical uncertainties and the MGPS-2 has the superior angular resolution, elliptical annuli with a ratio of minor to major axis and the center position from Green et al. (2014) were used for both maps. The angle of the ellipse was estimated to be 100° of the major axis with respect to North. The width of the annuli was chosen to be 0.8° . To match the angular resolution the MGPS-2 images were convolved

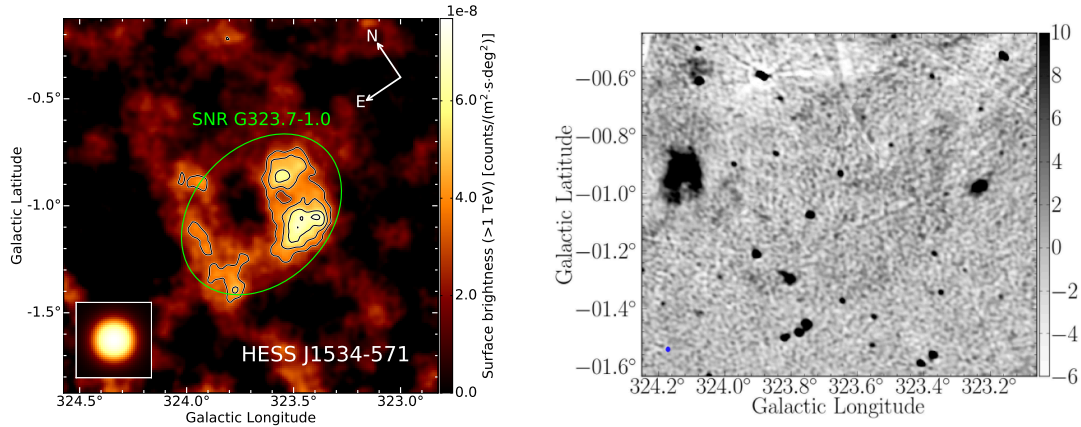


Figure 5.7: **Left:** Map of TeV surface brightness above 1 TeV of HESS J1534–571 in Galactic coordinates. A correlation radius of 0.1° was used to calculate the map and an additional Gaussian smoothing with $\sigma = 0.01^\circ$ was applied to remove artifacts. To calculate the number of expected counts a power law with an index of $\Gamma_{\text{ref}} = 2.3$ was used. The inset shows the point spread function of the observation with the same correlation radius and smoothing applied. The green ellipse illustrates the outer boundaries of the SNR candidate G323.7–1.0 from Green et al. (2014). Contours are 3, 4, 5, 6 σ significance contours. **Right:** Radio images of G323.7–1.0 in Galactic coordinates in mJy beam^{-1} . The blue circle in the bottom-left corner shows the beam size of the observation. (TeV map taken from H.E.S.S. Collaboration (2018a).)

with the H.E.S.S. psf before extracting the profiles. To match the profiles they were normalized to have the same integral value. The result is shown in Fig. 5.8. Visibly the profiles agree well, but to obtain a more quantitative measure the differences between the two curves were evaluated quantitatively. The difference of the two data points at the same semi major axis was calculated and divided by the quadratic sum of the statistical uncertainties:

$$\sigma = \frac{S_{\text{R}} - S_{\gamma}}{\sqrt{\sigma_{\text{R}}^2 + \sigma_{\gamma}^2}} \quad (5.19)$$

The resulting pull distribution was fitted with a standard distribution whose parameters are in agreement with normally distributed deviations as expected in case the two sources have the same morphology. Therefore, it is confirmed that G323.7–1.0 and HESS J1534–571 are associated. To summarize, the TeV SNR candidate has a corresponding detection in another waveband which is also classified as a SNR candidate. With this findings the source was classified as a SNR in H.E.S.S. Collaboration (2018a).

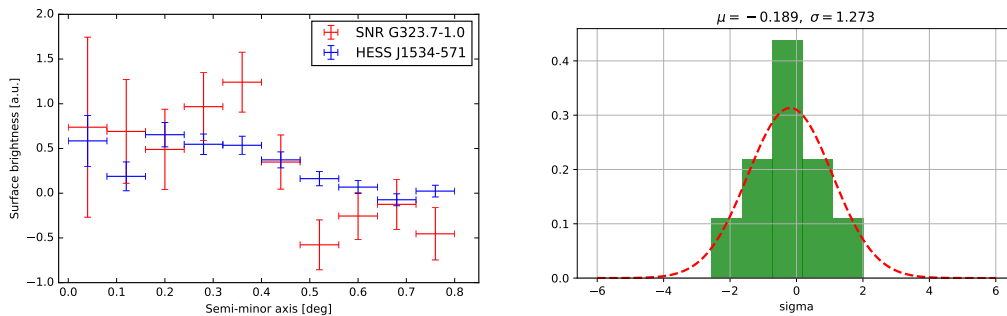


Figure 5.8: **Left:** Elliptical profiles of HESS J1534–571 and G323.7–1.0: The profiles were extracted using elliptical annuli with parameters taken from Green et al. (2014). The angle of the major axis with respect to North was estimated to be 100° . The width of the annuli was chosen to be 0.8° . To match the angular resolution, the MGPS-2 images were convolved with the H.E.S.S. psf before extracting the profiles. To match the profiles they were normalized to have the same integral value. **Right:** Pull distribution: The deviation between the two profiles in terms of the combined uncertainty is filled into a histogram with 5 bins. A fit of a Gaussian distributions was applied to the not rebinned data. The result is compatible to statistical fluctuations. (Elliptical profile taken from H.E.S.S. Collaboration (2018a).)

The total flux of G323.7–1.0 is measured to be (0.49 ± 0.08) Jy, compatible with the flux lower limit of 0.61 Jy reported by Green et al. (2014). The difference is caused mainly by the fact that there are two additional sources within the shell that have been masked for this work. Note that the measured flux values are only a lower limit because the Molonglo Observatory Synthesis Telescope (MOST) is not able to measure structures larger than $25'$. Nevertheless, with this flux values, a rough estimate of the distance of the SNR was done using an empirical relation between surface brightness and source diameter ($\Sigma - D$). Using the surface brightness of $S_{843 \text{ MHz}} = 0.49$ Jy and the relation $\Sigma_{1 \text{ GHz}} = 2.07 \times 10^{-17} \times D [\text{pc}]^{-2.38} \text{ W m}^{-2} \text{ Hz}^{-1} \text{ sr}^{-1}$ (omitting the errors on the parameters) from Case & Bhattacharya (1998) a distance of 20 kpc is estimated. The error estimated by Case & Bhattacharya (1998) is 40%, moreover the measured surface brightness is only a lower limit. But even for a distance at 10 kpc, HESS J1534–571 would imply a TeV luminosity exceeding the values of the known TeV SNRs significantly.

5.4.1.2 Other Wavebands

The catalogs for hard sources, 2FHL (Ackermann et al., 2016), and regular sources, 3FGL (Acero et al., 2015), of the *Fermi-LAT* (Atwood et al., 2009) reveals no source at the position of HESS J1534–571. A source template, derived from the surface brightness

map presented here, has been shared with the *Fermi-LAT* collaboration. Based on a conference proceeding of this work (Gottschall et al., 2017), Araya (2017) carried out an analysis of the public *Fermi-LAT* data set which yielded a clear detection in the energy range 5 GeV to 500 GeV with a test statistic of $TS = 57.4$. The source is fitted best with a disc model, position and extent are compatible with HESS J1534–571. In the GeV-band the source is more luminous in the eastern part than in the western part of the radio SNR whereas HESS J1534–571 shows the opposite. The spectrum is fitted best with a power-law model with an index of $\Gamma = 1.35$, the flux points agree reasonably well. Araya (2017) concludes from a broad-band SED modeling that a leptonic scenario fits best, and the energy budget is reasonable for an object at 5 kpc.

X-ray data would be extremely helpful to further constrain the emission processes in a SED modeling. Soon after the discovery of significant TeV emission from the position of HESS J1534–571, the source was observed with *Suzaku XIS* (Mitsuda et al., 2007; Koyama et al., 2007) in four pointings (observation IDs 508013010, 508014010, 508015010, 508016010, respectively, PI A. Bamba). Only part of the source is covered, further pointings were planned to finish the coverage, but due to the decommissioning of the telescope the observations were not carried out. No emission was detected. For details on the analysis confer further H.E.S.S. Collaboration (2018a). In the 2 keV to 12 keV band, an upper limit scaled to the area of the radio SNR of 2.4×10^{-11} erg cm⁻² s⁻¹ for a power-law model with $\Gamma = 2$, and 1.9×10^{-11} erg cm⁻² s⁻¹ for a power-law model with $\Gamma = 3$ was derived. Araya (2017) predicts from his modeling an X-ray flux of 2.7×10^{-14} erg cm⁻² s⁻¹ with a very steep index of $\Gamma = 3.1$ in the 2 keV to 10 keV band. Hence, the measured upper limits are not constraining that model.

In addition, a catalog search for PWNs and pulsars was carried out, no notable counterpart was found. Also archival infrared images from Midcourse Space Experiment (MSX) (Price et al., 2001) were examined. In this case, again nothing was found that helps understanding the nature of HESS J1534–571. Details can be found in H.E.S.S. Collaboration (2018a).

5.4.1.3 Atomic and Molecular Gas Density

Atomic and molecular gas densities from radio line emission towards HESS J1534–571 were investigated using Columbia CO(1-0) data (Dame et al., 2001) for the large-scale Galactic structure, Nanten CO(1-0) data (Matsunaga et al., 2001) with an angular resolution of $3'$, and Southern Galactic Plane Survey (SGPS) (McClure-Griffiths et al., 2005) HI data. No unambiguous association with features like HI voids (pointing towards the bubble of a high mass progenitor star), clouds with asymmetric velocity profiles (pointing towards shocked clouds), or dense clumps correlated to the bright

TeV emission were found. From the Columbia CO(1-0) data possible Galactic arms hosting the SNR and their distance were derived. The source is in projection with the Sagittarius-Carina, Crux-Centaurus and Norma-Cygnus arm. Due to the $\Sigma - D$ relation, the Sagittarius-Carina arm, which is closest, is unlikely. Remaining are the Scutum-Crux arm at a distance of 3.5 kpc and the Norma-Cygnus arm at 8 kpc (Vallée, 2008, 2013). For these two distances the total gas parameters were extracted for the discussion in Sect. 5.5.

5.4.2 HESS J1614–518

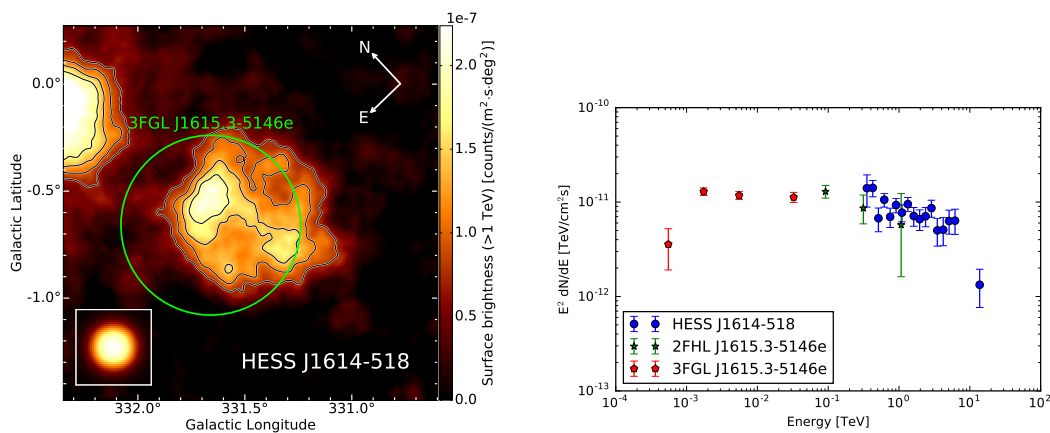


Figure 5.9: **Left:** Map of TeV surface brightness above 1 TeV of HESS J1614–518 in Galactic coordinates. A correlation radius of 0.1° was used to calculate the map and an additional Gaussian smoothing with $\sigma = 0.01^\circ$ was applied to remove artifacts. To calculate the number of expected counts, a power law with an index of $\Gamma_{\text{ref}} = 2.4$ was used. The inset shows the point spread function of the observation with the same correlation radius and smoothing applied. The green circle illustrates the outer boundaries of the *Fermi-LAT* sources 2FHL/3FGL J1615.3-5146e (Acero et al., 2015; Ackermann et al., 2016). Contours are 5, 7, 9, 11 σ significance contours. **Right:** SED of 2FHL/3FGL J1615.3-5146e and HESS J1614–518 as measured with *Fermi-LAT* and H.E.S.S. (Plots taken from H.E.S.S. Collaboration (2018a).)

5.4.2.1 GeV Emission with *Fermi-LAT*

3FGL J1615.3-5146e, a source in the third *Fermi-LAT* catalog (Ackermann et al., 2016), and 2FHL J1615.3-5146e, a source in the second *Fermi-LAT* catalog for hard sources (Acero et al., 2015), are modeled best with a disc model with matching extent and position. These source properties also agree well with the TeV emission as seen in figure 5.9. The *Fermi-LAT* source 3FGL J1615.3-5146e is shown as a green circle. The

energy range of the 3FGL is overlapping with the one of the 2FHL, which again is overlapping with the energy range of the H.E.S.S. observation. Consequently, a SED plot has been created (see Fig. 5.9). The source's spectra agree well and a break is visible from a power-law model with an index of 2 in the GeV range to an index of 2.4 in the TeV range. From the *Fermi-LAT* source, no conclusion on the source class can be drawn. Since additional conclusive MWL-data is missing, no constraints on the classification of HESS J1614–518 can be made.

5.4.2.2 Other Wavebands

A search for radio continuum emission was done, with the conclusion that no cataloged radio SNR exists. Furthermore, data from the SGPS (Haverkorn et al., 2006) and from the MGPS-2 (Murphy et al., 2007) were inspected without finding any obvious features. This is consistent with the findings of Matsumoto et al. (2008).

Also for this source a search in pulsar and PWN catalogs was performed without any match. Details can be found in H.E.S.S. Collaboration (2018a).

Infrared images from Spitzer in the 24 μm (Carey et al., 2009), 8 μm , and 2.4 μm (Churchwell et al., 2009) band were investigated (see Fig. 5.10) to search for HII emission regions. These could consist of stellar wind material of star forming regions (Kothes & Dougherty, 2007) which then may be a host of the progenitor star. Such a correlation was not found, but the open stellar cluster Pismis 22 is located close to the center of HESS J1614–518. The open stellar cluster could be a host of the progenitor star if the SNR scenario was confirmed. The age is estimated to be (40 ± 15) Myrs at a distance of (1.0 ± 0.4) kpc. H.E.S.S. Collaboration (2018a) discussed the luminosity of the cluster, and whether this luminosity is sufficient to explain the TeV emission. A fraction of the cluster's luminosity would be sufficient, but due to the lack of observational evidence this is purely hypothetical.

HESS J1614–518 was observed with *Suzaku* and *XMM-Newton* after its discovery (Aharonian et al., 2006c). Several pointings were carried out with both satellites. The pointings were focused on the northern, southern and central part because the TeV source is brightest there. Matsumoto et al. (2008) and Sakai et al. (2011) reported a central source, first the extended source *Suzaku* J1614–5152 which then was resolved in several point sources with *XMM-Newton* including the strongest source XMMU J161406.0–515225. This source is relevant because it is only 1' away from the center of HESS J1614–518. Matsumoto et al. (2008) argued that it could be an anomalous X-ray pulsar related to the TeV object. From the temperature of the fitted black-body model ($T \simeq 0.4$ keV), the source could also be a central compact object (CCO)

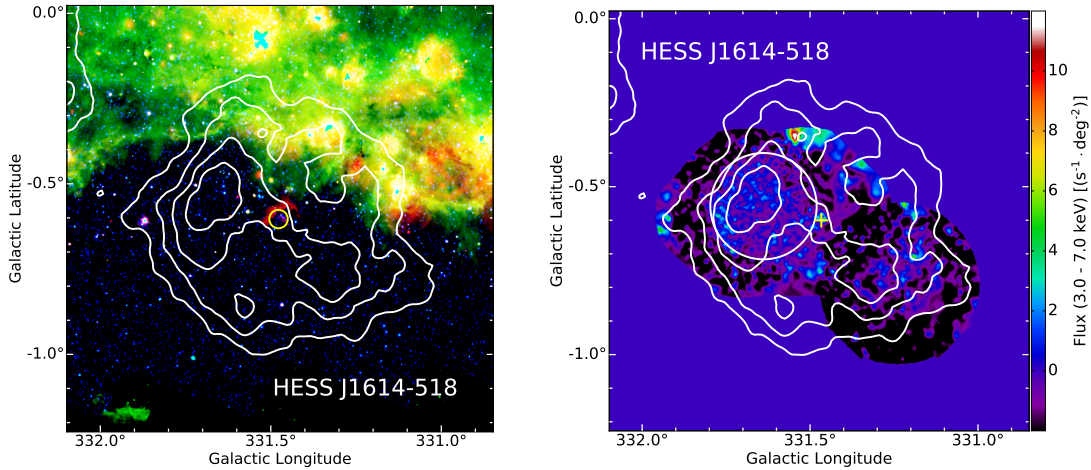


Figure 5.10: **Left:** IR composite image from Spitzer: The $24\ \mu\text{m}$ (Carey et al., 2009), $8\ \mu\text{m}$, and $2.4\ \mu\text{m}$ (Churchwell et al., 2009) band was combined into an RGB image. The colorscale was adjusted individually. HESS J1614–518 is displayed using surface brightness contours in white. The yellow circle close to the center of HESS J1614–518 highlights the open stellar cluster Pismis 22 (Morales et al., 2013). **Right:** *XMM-Newton* hard band: The skymap shows the X-ray emission in the 3 keV to 7 keV band (H.E.S.S. Collaboration, 2018a). The yellow cross shows the position of XMMU J161406.0–515225 and the white circle shows the extended diffuse emission northeast from the center of HESS J1614–518. (Plots taken from H.E.S.S. Collaboration (2018a).)

of a possible SNR. However, XMMU J161406.0–515225 has an optical point source counterpart as reported by Landi et al. (2006), and it was classified as a star candidate by Lin et al. (2012). In addition to the X-ray source XMMU J161406.0–515225, Matsumoto et al. (2008) reported the extended source Suzaku J1614–5141 which coincides with the north-eastern part of HESS J1614–518. The column density of this source and the aforementioned point source are similar and could therefore be at the same distance and related to the TeV source. Estimating the distance from the column density results in an estimate of the order of 10 kpc. H.E.S.S. Collaboration (2018a) reevaluated the entire *XMM-Newton* data set (see Fig. 5.10).

An estimation of the flux of the X-ray emission was attempted, but because of the stray-light contamination the systematic errors are large. Due to the complexity of the analysis and the limited impact on the source interpretation, an extensive assessment was not done for H.E.S.S. Collaboration (2018a) or for this work.

5.4.2.3 Atomic and Molecular Gas Density

The same radio surveys for atomic and molecular gas (CO(1-0) and HI) were examined towards HESSJ1614–518 as for HESS J1534–571 before. In the direction of the source lie the Galactic spiral arms Sagittarius-Carina, Scutum-Crux, and Norma-Cygnus. The only interesting feature on the line of sight is an HI void with a velocity of $v_{\text{lsr}} = -15 \text{ km s}^{-1}$ to -22 km s^{-1} which correspond to a distance range of 1.2 kpc to 1.5 kpc. The gas densities were estimated for the discussion of a possible hadronic emission process (Sect. 5.5) for two different distances: For a distance of 1.5 kpc which coincides with the Sagittarius-Carina spiral arm (Vallée, 2008), the HI void, and Pismis 22 (Piatti et al., 2000) and for 5.5 kpc which coincides with the Norma-Cygnus spiral arm (Vallée, 2008), and which is consistent with the X-ray column density.

5.4.3 HESS J1912–101

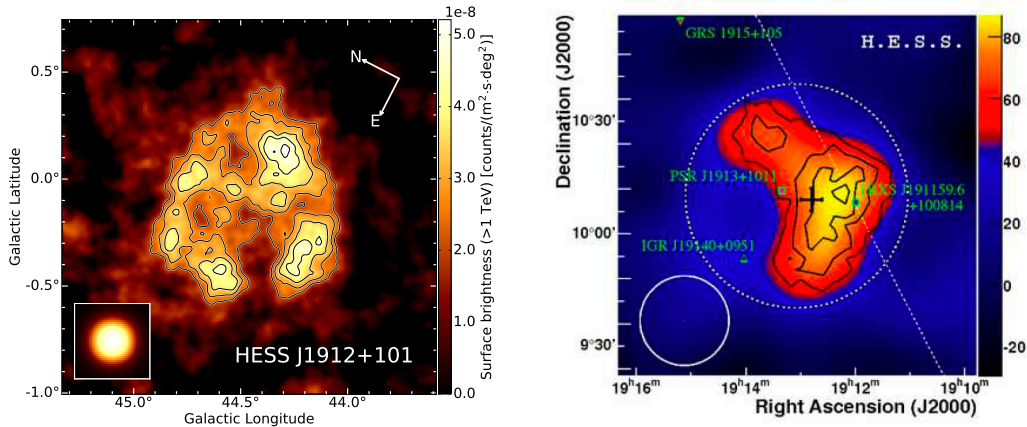


Figure 5.11: **Left:** TeV surface brightness above 1 TeV map of HESS J1912–101 in Galactic coordinates. A correlation radius of 0.1° was used to calculate the map and an additional Gaussian smoothing with $\sigma = 0.01^\circ$ was applied to remove artifacts. To calculate the number of expected counts, a power law with an index of $\Gamma_{\text{ref}} = 2.5$ was used. The inset shows the point spread function of the observation with the same correlation radius and smoothing applied. Contours are 3, 4, 5, 6, 7 σ significance contours. **Right:** H.E.S.S. excess map from Aharonian et al. (2008a). A Gaussian smoothing with $\sigma = 0.13^\circ$ was applied. The contours show 3.5, 4.5, 5.5 and 6.5 σ . Among other sources the pulsar PSR J1913+1011 is marked in the map. (Surface brightness map taken from H.E.S.S. Collaboration (2018a).)

5.4.3.1 The Pulsar Wind Nebula Scenario

HESS J1912–101 was detected and published by the H.E.S.S. collaboration (Aharonian et al., 2008a). The resulting sky map from the detection data set which was significantly smaller than the current data set (20.8 h versus 121 h, both acceptance corrected for an offset of 0.5°), led to a different interpretation. First, as seen in Fig. 5.11, the excess map of Aharonian et al. (2008a) reveals a different morphology. The source is extended with a clear maximum to the west. Although the large correlation radius and the sharp break in the color bar at 3σ might be masking a more complex morphology, the result seemed to be compatible to a PWN scenario. Second, close to the centroid of the source, the powerful radio pulsar PSR J1913+1011 is located. The spindown power of the pulsar is $\dot{E} \simeq 2.9 \times 10^{36} \text{ erg s}^{-1}$. A characteristic spindown age of 1.7×10^5 years, a spin period of 36 ms, and a distance estimated from the dispersion measurement of 4.5 kpc was derived. As estimated by Aharonian et al. (2008a) the pulsar is powerful enough to be the origin the emission reported in 2008, but a PWN was not detected in any other energy band. Therefore the scenario remained an assumption back then. While significantly expanding the data set, the detected morphology changed. According to the methodology presented in H.E.S.S. Collaboration (2018a), HESS J1912–101 shows a highly significant shell-like appearance. To examine whether this result is statistically compatible with Aharonian et al. (2008a), a side by side comparison of the two data sets was done. Unfortunately, the low-level results of Aharonian et al. (2008a) were not available. Instead, a new analysis was carried out on the data set until 2008. Apart from reducing the data set, no boosted decision trees were used for the γ /hadron separation. This technique was not available for the study in 2008. The background method remained the same. The results were recreated using the current software version and are shown in 5.12. On the left an excess map using a Gaussian smoothing with $\sigma = 0.13^\circ$ and a color bar matching the one from Aharonian et al. (2008a) is shown. The break between blue and red was placed at an excess level roughly equal to 3σ . On the right a TeV surface brightness above 1 TeV of the reduced data set is shown using the same correlation radii and smoothing as for Fig. 5.11. The significance contours of the full data set are overlaid.

To test the compatibility of the full data set with the reduced one, an azimuthal profile of both maps was produced and overlaid. This is shown in Fig. 5.13. The results agree well expect one outlier, which is still less than three standard deviations away from the value of the full data set. It is concluded that the seeming difference in appearance of the source is due to the five times larger data set.

The interpretation of Aharonian et al. (2008a) was mainly driven by the presence of the pulsar PSR J1913+1011 that is capable of driving the TeV emission, and the

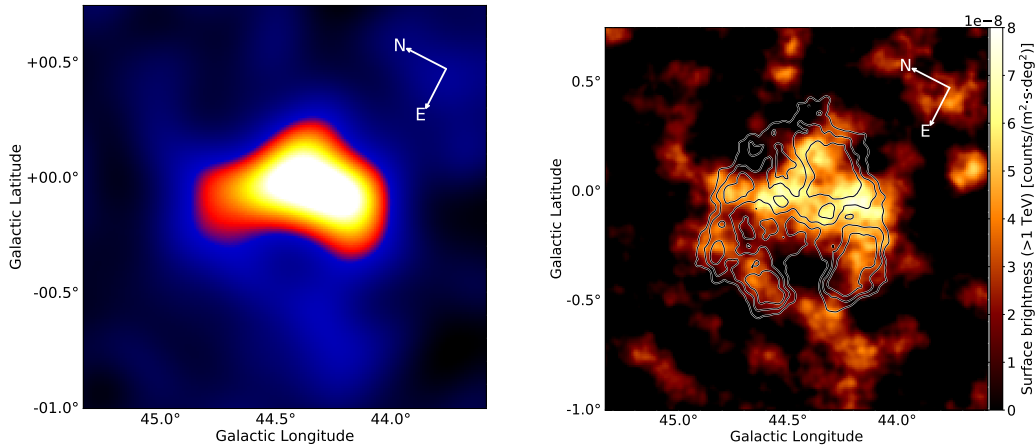


Figure 5.12: **Left:** TeV excess for the data set used by Aharonian et al. (2008a): The map was created using the technique described in section 5.3 without using boosted decision trees for γ /hadron separation. The resulting excess was smoothed with a Gaussian function with $\sigma = 0.13^\circ$. The color bar was matched to the one in Aharonian et al. (2008a). The results were reproduced with the current software version. **Right:** TeV surface brightness above 1 TeV of the reduced data set. From the same excess as on the left, a surface brightness map was created using a correlation radius of 0.1° and an additional Gaussian smoothing with $\sigma = 0.01^\circ$. Overlaid are the significance contours of the full data set (see Fig. 5.11).

morphological appearance of HESS J1912–101. The resulting PWN scenario could not be confirmed by any other measurements. The different appearance of the source in this study is compatible with the original result. Thus, a main candidate is a SNR in which the pulsar could be the remnant of the progenitor star of the supernova. Therefore, the distance of the pulsar remains one of the distance estimates of this source. Other scenarios are still possible, e.g. a super bubble or several unrelated sources mimicking the shell appearance. Consequently the source remains a SNR candidate.

A catalog search for pulsars and PWN did not reveal further information. For details see H.E.S.S. Collaboration (2018a).

5.4.3.2 Other Wavebands

Due to the source GRS 1915+105 which is only $47'$ away from the center of HESS J1912–101, X-ray observations are affected by strong stray light, for example in *ASCA* observations. The pulsar PSR J1913+1011 was observed with *Chandra*, but the observation only covers the central part of the source. No diffuse emission was detected (Chang et al., 2008). For the time being the shell of HESS J1912–101 remains unexplored in X-ray.

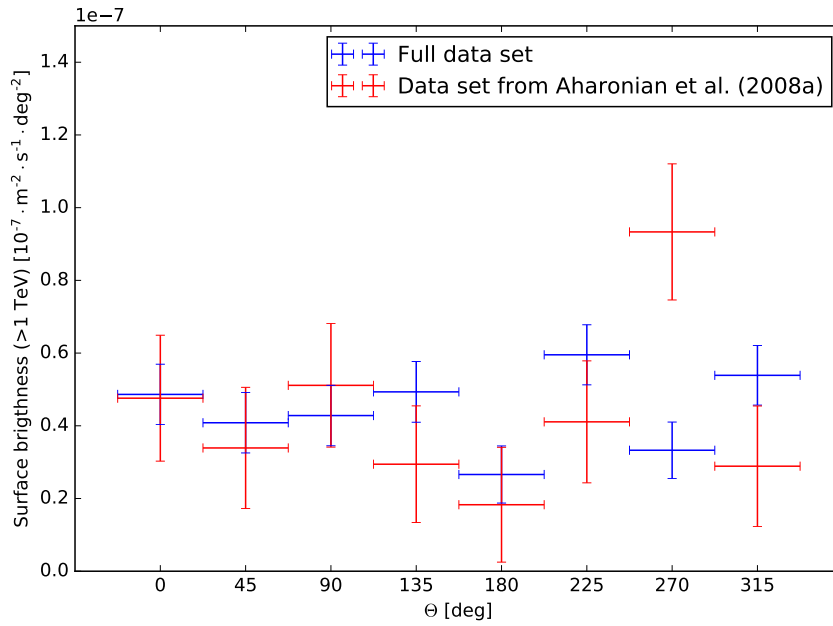


Figure 5.13: Azimuthal profiles of the full data set overlaid with the reduced data set following Aharonian et al. (2008a): The same method as in Fig. 5.4 was used and the data sets were overlaid. Apart from one outlier the data set is well compatible within statistical uncertainties. The remaining outlier is still less than 3σ apart. The differences in morphological appearance is due to the five times larger data set.

Also radio continuum observations from the NRAO/VLA Sky Survey (Condon et al., 1998) at 1.4 GHz and from MAGPIS (Helfand et al., 2006) were examined. No obvious counterpart was found. The radio SNR candidate G44.6+1.0 is coincident with a part of HESS J1912–101, but the source is much smaller. Furthermore, there are no morphological correspondences between the two sources. It is not apparent that the sources are connected.

Infrared images from Spitzer in the 24 μm (Carey et al., 2009), 8 μm , and 2.4 μm band (Churchwell et al., 2009) were investigated without a conclusive result.

Further details can be found in H.E.S.S. Collaboration (2018a).

5.4.3.3 Atomic and Molecular Gas Density

Publicly available radio data were studied to examine the surroundings of the sources, and to constrain the distance estimate. In the case of HESS J1912+101, Nanten (CO(1-0)) data (Matsunaga et al., 2001), the Galactic Ring Survey ($^{13}\text{CO}(1-2)$ and CS(2-1))

(Jackson et al., 2006), and VLA Galactic Plane Survey (HI) (Stil et al., 2006) were examined. Additionally Columbia CO(1-0) data (Dame et al., 2001) were used to create longitude-velocity plots to illustrate the large scale structure towards the sources. In the velocity plots, two components are visible meeting close to the tangential point of the Sagittarius arm which results in large uncertainties in the distance estimate. Nevertheless, a distance estimate of 4.5 kpc, also compatible with the dispersion measurement of PSR J1913+1011 for the Sagittarius arm, and 10 kpc for the Perseus arm was chosen to derive gas density numbers for the discussion of a potential hadronic scenario. For details on this measurement see H.E.S.S. Collaboration (2018a).

Based on the conference proceedings by Gottschall et al. (2017) and Pühlhofer et al. (2015), Su et al. (2017) speculate that HESS J1912+101 is associated to an old SNR. By looking at ^{12}CO and HI lines, they identified features pointing towards turbulent gas that has been shocked by the shock front of a supernova. They also describe an HI shell consistent with an old SNR. Although the age would be consistent with the characteristic age of the pulsar PSR J1913+1011, the resulting kinematics make explaining the VHE emission challenging.

5.5 Discussion

Based on the morphological study, HESS J1534–571, HESS J1614–518, and HESS J1912–101 were classified as SNR candidates. The association of HESS J1534–571 with the radio SNR candidate G323.7–1.0 led to a classification as SNR. The TeV flux of HESS J1912–101 is sufficiently high so that a detection with *Fermi-LAT* should be possible just like for the other two sources. Templates of all three sources have been shared with the *Fermi-LAT* collaboration. To support the classification, the GeV emission will most likely not be helpful, but constraining the details on the emission process is possible as for example shown by Araya (2017). The non-detection of a non-thermal radio counterpart for HESS J1614–518 and HESS J1912–101 is not contradicting the SNR hypothesis. The lack of non-thermal X-rays is interesting, but the coverage of the outer shell is incomplete for all three sources.

It is important to put these sources in context with the existing firmly identified TeV shell SNRs. Unfortunately, no firm distance estimates are available for the three sources from the search. A generic case for 1 kpc and two cases with the most probable distance estimate were calculated and are shown in table 5.11. For HESS J1731–347 two cases are shown as well.

The lack of constraining observations of these sources apart from the flux and extent in the TeV band makes it very difficult to constrain the nature of the sources itself.

Table 5.11: Basic parameters of known SNRs and the new shell-like sources: For every source the most probable distances are shown together with the calculated diameter and luminosity. In addition to the power-law index, the age is quoted if known. For the new sources a generic case at 1 kpc together with the two most probable distance estimates are shown.

Source name	Dist. [kpc]	Diameter [pc]	Age [kyr]	$L_{1\text{ TeV}-10\text{ TeV}}$ [10^{33} ergs^{-1}]	Γ_{PLfit}	Ref.
HESS J0852–463	0.75	26.2	1.7–4.3	5.7	2.3	(1)
HESS J1442–624	2.5	30.0	1.8	6.3	2.3	(2)
HESS J1502–418	2.2	22.3	1	0.46	2.4	(3)
HESS J1502–421				0.31	2.3	(3)
HESS J1713–397	1	20.2	1	7.2	2.3	(4)
HESS J1731–347	3.2	30.2	2.5	8.5	2.3	(5)
	5.2	49.0		22.4		
HESS J1534–571	1.0	14.0		0.78		
	3.5	48.9		9.6	2.5	(6)
	8	111.7		50		
HESS J1614–518	1.0	14.7		2.4		
	1.5	22.0		5.3	2.4	(6)
	5.5	80.6		71		
HESS J1912+101	1.0	17.1		0.97		
	4.5	77.0		19.6	2.6	(6)
	10	171.0		97		

References. (1) Aharonian et al. (2007); H.E.S.S. Collaboration (2018b); (2) H.E.S.S. Collaboration (2018c); (3) Acero et al. (2010); (4) Aharonian et al. (2006a); H.E.S.S. Collaboration (2018e); (5) H.E.S.S. Collaboration (2011); Klochkov et al. (2015); (6) H.E.S.S. Collaboration (2018a)

Although the lack of non-thermal radiation in other wavebands (apart from the radio counterpart of HESS J1534–571) seems to be promising for a purely hadronic emission scenario of an older population than the other shell-like SNRs, it can be explained, for example with stray light and lack of coverage in X-ray or complex regions in the radio band. When comparing the new sources to the existing ones, one fact seems to be obvious: The far estimate at 5.5, 8 and 10 kpc would result in a size above 80 pc and up to 171.0 pc. A study by Badenes et al. (2010) on SNRs in the LMC and M 33 shows a cut-off at around 60 pc. Also in this study outliers to larger diameters are present, mainly attributed to the ambient medium modified by a progenitor stars. Compared to the other known sources, both the luminosity and diameter for these distances would be at least by a factor of a few higher. The closer distance estimate for the sources is in line for HESS J1534–571 and HESS J1614–518. For HESS J1912+101 the luminosity and size are much larger than for the other known sources.

Overall the index of the fitted power-law models is softer than for the other known sources. However, for the individual sources the uncertainty of the power-law index is too high to draw any conclusions from this.

5.5.1 TeV Emission from Leptons or Protons

One fundamental question raised in the introduction is how much of the energy of the ejecta of SNRs goes into a non-thermal component of relativistic particles and what is the share of hadrons and leptons. Together with the maximum energy of the hadrons, it can be determined whether and how much SNRs contribute to the Galactic CRs. An estimate of the energy that went into the production of CRs was done based on the TeV luminosity and the distance estimates of the sources. Note that it was assumed that the luminosity is only caused by decaying π^0 produced by protons. For this calculation, following Kelner et al. (2006), the argument was used that $E_p = 10 \times E_\gamma$ and that the total energy of accelerated protons in the 10 TeV to 100 TeV range can be estimated from the γ -ray luminosity in the 1 TeV to 10 TeV using the characteristic cooling time of protons by the π^0 production (Aharonian et al., 2006a):

$$W_p^{\text{tot}}(10 - 100 \text{ TeV}) \approx \tau_{\text{pp} \rightarrow \pi^0} L_\gamma(1 - 10 \text{ TeV}) \quad (5.20)$$

and

$$\tau_{\text{pp} \rightarrow \pi^0} \approx 4.5 \times 10^{15} \left(\frac{n}{\text{cm}^{-3}} \right)^{-1} \text{ s}. \quad (5.21)$$

To calculate the total energy for a wider energy range, the luminosity of the source was calculated based on the measured spectral parameter while introducing a break at 10 TeV where the index changes from $\Gamma = 2$ for $1 \text{ GeV} \leq E_p \leq 10 \text{ TeV}$ to the measured one for $10 \text{ TeV} \leq E_p \leq 100 \text{ TeV}$. This assumption is reasonable for the spectra derived in the H.E.S.S. study and also fits to the spectrum of 3FGL J1615.3–5146e.

Table 5.12 lists the distance estimates, the corresponding velocity of the gas, the total proton density estimated from atomic and molecular gas, and the total proton energy from 1 GeV to 100 TeV for each source.

For the generic case and the closer of the two solutions, the proton scenario for all sources is reasonable with an expected energy content of 10% of 1×10^{51} erg. For distances at the 8 kpc..10 kpc scale and beyond, the hadronic scenario is disfavored. To further constrain this value, additional MWL data is needed. First attempts have been made by Araya (2017) through the examination of the *Fermi-LAT* data towards HESS J1534–571, detecting the source in the GeV band, and modeling the emission

Table 5.12: Proton energy content: Assuming a generic distance of 1 kpc, and proton density of 1 cm^{-3} , the total proton energy from 1 GeV to 100 TeV was calculated. The same value was derived for the two most probable distance estimates from the MWL study and for the proton density derived from radio observations (c.f. H.E.S.S. Collaboration, 2018a). The luminosities of the sources were calculated based on the measured spectral parameter, but introducing a break at 10 TeV where the index changes from $\Gamma = 2$ for $1 \text{ GeV} \leq E_p \leq 10 \text{ TeV}$ to the measured one for $10 \text{ TeV} \leq E_p \leq 100 \text{ TeV}$.

Source name	Dist. [kpc]	velocity [km s ⁻¹]	$n_{\text{p,HI+H2}}$ [cm ⁻³]	$W_{\text{p,1 GeV-100 TeV}}^{**}$ [1×10^{51} erg]
	1.0	-	1	0.03
HESS J1534–571	3.5	–55..–45	4..29	0.08..0.009
	8	–88..–78	1.3..7	1.34..0.25
	1.0	-	1	0.08
HESS J1614–518	1.5	–30..–12	3..71	0.06..0.002
	5.5	–110..–80	17..110	0.14..0.02
	1.0	-	1	0.04
HESS J1912+101	4.5	45..73	28..178	0.03..0.004
	10	5..15	4..8	0.88..0.44

in a leptonic scenario together with the preliminary H.E.S.S. spectrum by Gottschall et al. (2017).

5.6 Summary

On the entire legacy H.E.S.S. phase I dataset covering the Galactic plane, a search for sources with shell morphology was done. In addition to pointed observations on specific sources, a scan was done such that the search covered almost half of the Galactic plane. The goal of the presented study was to exploit this data set in order to select SNRs from their VHE γ -ray morphology. From this search four candidates revealed a significant shell morphology compared to a simple Gaussian model. Since the search itself and the statistical test used have some limitations, a rigorous re-analysis and morphological study of these four sources was performed. HESS J1023–577 turned out to be a false positive, and three candidates remained. A MWL study was done, revealing the SNR candidate G323.7–1.0 with an excellent match to the TeV properties of HESS J1534–571. From the TeV data alone other scenarios could not be excluded, but with the detection of non-thermal radio emission with a perfect match to the properties of HESS J1534–571, HESS J1534–571 has been classified as SNR whereas the other two sources, HESS J1614–518 and HESS J1912+101 remain SNR candidates. No

other constraining counterparts for the sources were found. The spectral analysis together with the measured gas densities and the Galactic spiral arms on the line of sight made it possible to make some statements on the distance based on associations with Galactic arms and comparison with other TeV SNRs. Distances smaller than 1 kpc are very unlikely due to the missing X-ray emission, distances larger than 8 kpc would lead to very large physical diameters and very high luminosities for the sources compared to other TeV SNRs. Distances at the 1 kpc to 4 kpc range seem to be most likely. The ongoing work has been presented at conferences (Pühlhofer et al., 2015; Gottschall et al., 2017) and created great interest in the community. Following the presentations, studies in other wavebands were done, most notable Araya (2017) in the GeV band for HESS J1534–571 and Su et al. (2017) using radio line emission to study the surroundings of HESS J1912+101. From the current MWL data both leptonic or hadronic processes are possible as well as a mixture of both. The complete work has been published in *Astronomy & Astrophysics* (H.E.S.S. Collaboration, 2018a).

This study shows that IACTs with their high sensitivity in a relatively large field of view of the order of a few degrees are a perfect tool to discover new SNRs. It also shows the great potential of Cherenkov Telescope Array to discover new TeV SNRs.

6 Target of Opportunity Observation of the Classical Nova Sgr 2015 No. 2 with H.E.S.S.

6.1 Introduction

Novae occur when white dwarf stars accrete matter from a companion star onto their surface. During this process a thermonuclear runaway explosion can be triggered on the surface of the white dwarf star (Kraft, 1964). Novae are usually discovered by the optical brightening of the binary system (e.g. Lundmark, 1921). Spectral studies in the optical band and studies of counterparts in radio, infrared and X-ray show that as part of the process, ejecta are expanding into the ISM (Bode & Evans, 2008; Woudt & Ribeiro, 2014). In the process γ -ray emission from nuclear decay is produced with lines at \sim MeV energies from unstable isotopes and positron annihilation (e.g. Clayton, 1981, and references therein).

In 2010 for the first time GeV γ -ray emission from the symbiotic nova V 407 Cyg was discovered with *Fermi-LAT* (Abdo et al., 2010). The binary system V 407 Cyg consists of a Mira-type pulsating red giant and a white dwarf companion which places it among the class of symbiotic binaries. Abdo et al. (2010) proposed both a leptonic model and a hadronic model as possible explanation. In terms of modeling, two examples are discussed here. Sitarek & Bednarek (2012) speculated that the strong radiation field of the red giant could explain the GeV emission through inverse Compton scattering. From the same model, a second TeV component is expected from proton-proton interaction with the stellar wind of the red giant. Martin & Dubus (2013) consider leptons and hadrons being accelerated in the shock of the nova. From an estimate of the magnetic field and the acceleration efficiency, protons up to 300 GeV are expected. The γ -ray emission itself would be dominated by inverse Compton scattering from relativistic electrons. For symbiotic novae it should be possible to probe these models with IACTs by measuring the high-energy component of the emission. Especially CT5 with its energy threshold of tens of GeV is a perfect instrument for such a measurement. For short lasting phenomena up to $\sim 10 \times 10^7$ s, H.E.S.S. is more sensitive than *Fermi-LAT*

at tens of GeV in energy. Figure 6.1 shows the differential sensitivity over observation time for three different fixed energies for H.E.S.S., *Fermi-LAT*, and CTA.

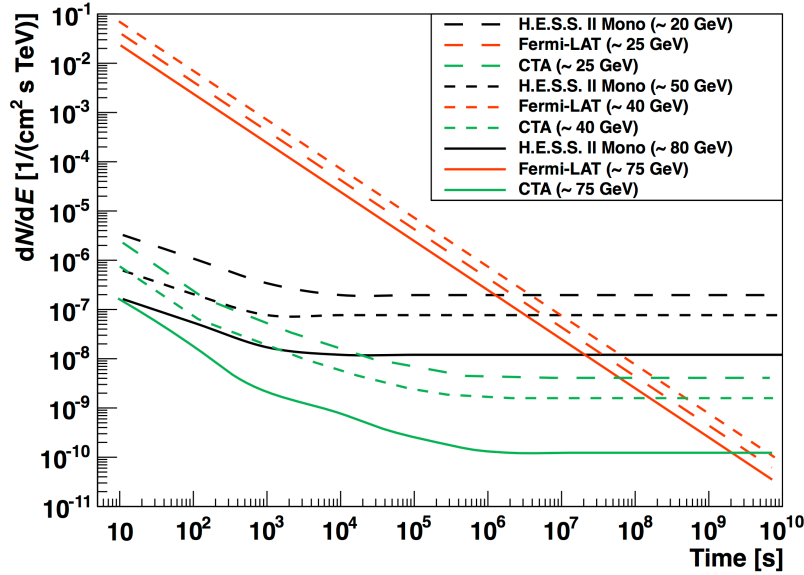


Figure 6.1: Differential sensitivity of different H.E.S.S. cut sets at several energies as a function of observation time, in comparison with *Fermi-LAT* and CTA. The figure is taken from the poster presented by Parsons et al. (2015a) at the ICRC in 2015.

The models were developed to explain the emission from a symbiotic nova, where the companion of the white dwarf star is a red giant with strong stellar wind and a dense radiation field. In the last years, *Fermi-LAT* discovered emissions from several classical novae (Ackermann et al., 2014). In these cases the strong wind of the red giant is missing, nevertheless the spectral properties are similar to those of V 407 Cyg. Possible explanations are that acceleration occurs in a bow shock between the ejecta and the ISM or in internal shocks in the inhomogeneous ejecta (Ackermann et al., 2014). Following this discovery, Chomiuk et al. (2014) presented a model in which the orbital motion of the system shapes the ejecta into a faster polar wind component and a slower region of denser material along the equatorial plane. Metzger et al. (2015) suggest that fast outflows from the nova might interact with the ejected shell to create γ -ray emission from hadronic interaction. The γ -ray emission from this suggested process is in an energy range accessible to current IACTs.

No VHE emission has been detected for any nova so far. The symbiotic nova V 407 Cyg was observed by VERITAS, 10 days after the optical peak and a differential upper limit at 1.6 TeV of $2.3 \times 10^{-12} \text{ erg cm}^{-2} \text{ s}^{-1}$ was derived (Aliu et al., 2012). The classical

nova V 339 Del, the symbiotic nova YY Her and the dwarf nova ASASSN-13ax were observed with MAGIC. For V 339 Del, upper limits were derived to constrain the ratio of hadronic emission from neutral pion decay L_p to inverse Compton from electrons L_e (Ahnen et al., 2015). A limit of $L_p \lesssim 0.15L_e$ was deduced following the model from Metzger et al. (2015).

H.E.S.S. has a ToO program for novae in place. Here a study on the classical nova Sgr 2015 No. 2 (V 5668 Sgr), observed with H.E.S.S., is discussed. The observation was triggered by a *Fermi-LAT* observation which led to a detection in the GeV band (Cheung et al., 2016). The observation of this target with H.E.S.S. is presented in detail together with a data analysis of the available data. Upper limits were derived from this observation and studied together with the *Fermi-LAT* data to constrain the L_p/L_e ratio. Possible updates to the ToO policy for novae are discussed in the context of this observation and recent discoveries in other wavebands.

6.2 Observation of the Classical Nova Sgr 2015 No. 2 with H.E.S.S.

The observation was triggered on the 24th of March 2015 by an Astronomers Telegram (Atel) of Cheung et al. (2015a). They reported that *Fermi-LAT* began a pointed observation on MJD57098.9 about 2 days after the optical discovery. The optical emission of the nova peaked on MJD57102.5. Between MJD57104 and MJD57105.24 evidence of emissions at energies greater than 100 MeV from the nova with 3.8σ significance was reported 1.5 days after the optical peak. Following this announcement H.E.S.S. commenced an observation in the following night. Nine runs were taken in two nights with CT5 only four to five days after the optical peak. In the first night no problems were reported, in the second night three runs were affected by bad weather and one run was interrupted by a shooting star. A second Atel reporting continuous activity of the source led to the decision to conduct a second H.E.S.S. observation (Cheung et al., 2015b). Two runs were taken in the night from the 1st to the 2nd of April. Bad weather was reported from the shift crew. Further observations were prevented by the period of full moon. When the source was observable again, it was decided not to continue observing because too much time had passed since the peak in the optical band.

6.3 Analysis of Available H.E.S.S. Data

6.3.1 Data Quality

A marginal signal was expected from the data if at all. Additionally, since the observations were performed with CT5 only, the reconstruction is susceptible to hardware problems which can lead to a high intensity in a small group of pixels. When those pixels are reconstructed as showers, hot spots can appear in the camera. Generally the calibration chain detects such events and removes problematic pixels. Nevertheless, the analysis was carried out very carefully following the suggestions of the internal H.E.S.S. GRB task group including low level checks on the raw data which usually are taken care of by the calibration chain and the run quality selection.

From the shift reports it was already to be expected that a few runs were not usable due to bad weather. This was confirmed by the standard quality cuts discussed in section 3.3.8. From the eleven runs taken during the observation campaign, five runs were rejected because of an unstable trigger rate due to clouds which was also confirmed by a manual inspection of the trigger rate evolution of the runs. No technical problems were found in any of the runs passing the automatic quality selection.

One simple way to detect a group of noisy pixels is to look at the pixel participation fraction. After calibration and image cleaning, which removes all pixels except clusters of pixels above a certain threshold (c.f. section 3.3.9), the number of times an individual pixel is participating in an event is counted. Typical values for a CT5 mono observation are a pixel participation of $(1.0 \pm 0.4)\%$ of the events for each pixel. Figure 6.2 shows two examples for two randomly chosen observation runs of the data set. Apart from a missing drawer (16 pixel) nothing unusual is seen in the plot. The missing drawer is not a problem for the quality of the run. These plots have been created and inspected for all runs.

This test, together with a check of the stability of the trigger rate, confirmed the result of the automated run quality selection. The total good observation time is 2.7 h.

6.3.2 Skymap and Upper Limits

For the event reconstruction, a maximum likelihood fit of camera pixel amplitudes to an expected image amplitude was used (Parsons & Hinton, 2014; Parsons et al., 2015b). This Image Pixel-wise fit for Atmospheric Cherenkov Telescopes (ImPACT) provides a better reconstruction result and, especially for monoscopic events, a higher sensitivity compared to a Hillas based analysis like the reconstruction technique presented in

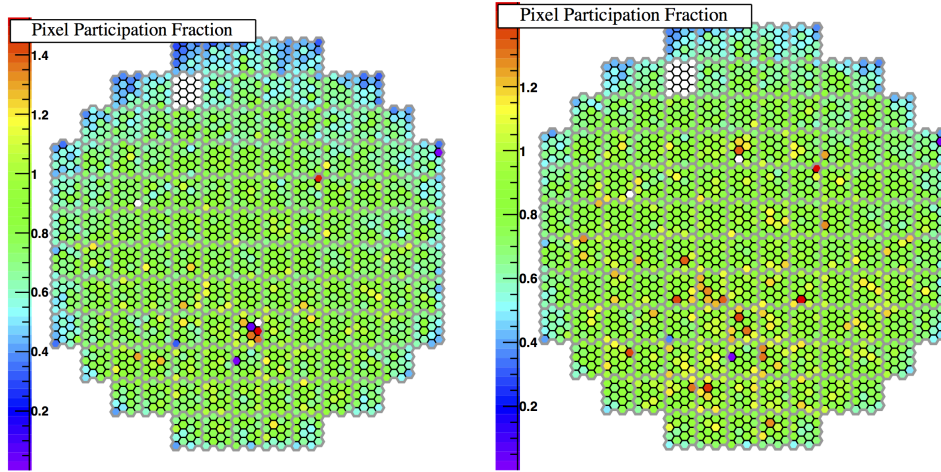


Figure 6.2: Pixel participation fraction of two CT5 mono runs: The plot shows how often an individual pixel was part of a shower event after image cleaning in percent. In both cases the plot is as expected apart from a missing drawer on the top right.

Murach et al. (2015). For a H.E.S.S. I stereo reconstruction, the differences between the ImpACT and Hillas reconstruction with BDT for γ /hadron separation, like it was applied in chapter 5, are not big. Furthermore, for the study in chapter 5, an analysis setup close to the one used for the HGPS was applied to treat the different analysis steps as homogeneously as possible. In this case, the cuts on image amplitude and also on the shower parameters used, were optimized for sources with a spectral index of around 2.5. This set of cuts is called standard cuts. A cut set for very soft sources has been tested as well. These so-called loose cuts result in a lower energy threshold, but the overall sensitivity is lower.

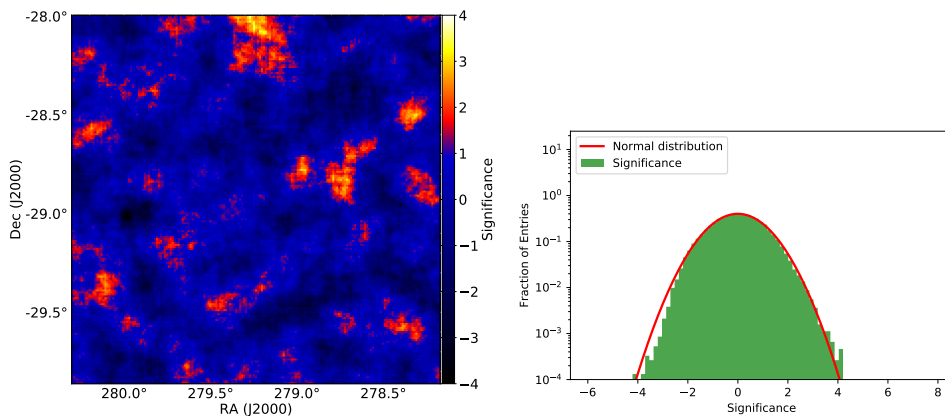


Figure 6.3: Significance map for Nova Sgr 2015 No. 2: The significance per pixel was calculated using equation 17 of Li & Ma (1983) for a circle with a radius of 0.1° . On the right, the number of entries per significance is shown compared to a normal distribution.

For source detection, an excess and significance sky map was created using the ring background method, described in section 3.3.10. Checks on the resulting maps were performed using the same technique as outlined in section 5.3.2.2. Neighboring pixels were correlated using a circle with a radius of 0.1° . The angular resolution of this dataset, using a monoscopic reconstruction, is $R_{68} = 0.16^\circ$. The significance of the excess has been calculated using equation 17 of Li & Ma (1983). The result is shown in figure 6.3 on the left. For the position used by Cheung et al. (2016) for the *Fermi-LAT* analysis, the results of the event reconstruction for a point source assumption is shown in table 6.1.

Table 6.1: Livetime and event statistics for the ring background method for Nova Sgr 2015 No. 2: The table lists the livetime after exposure correction, the number of ON events falling into the test position, the number of OFF events within the background control region, the ratio between ON and OFF region α , the number of excess events, the signal to background ratio, and the significance (equation 17 of Li & Ma (1983)).

Source	Livetime	ON	OFF	α	Excess	S/B	σ
Nova Sgr 2015 No. 2	2.6 h	291	3494	0.08	8.5	0.03	0.5

Figure 6.3 on the right shows the distribution of entries of the significance map. In addition, a normal distribution with a mean of 0 and a width of 1 is plotted. Fitting a Gaussian function shows parameters well compatible with a normal distribution.

No significant excess was detected, neither at the position of the nova in other wavebands nor for any other positions in the field of view of the observation.

To extract upper limits at the position of the source, the reflected region background method was used for the most reliable background estimation (section 3.3.10). Furthermore, an energy bias cut was applied to ensure that the energy bias from the reconstruction is smaller than 10%. Table 6.2 lists the event statistics.

Table 6.2: Livetime and event statistics for the reflected region background method for Nova Sgr 2015 No. 2: The table lists the livetime after exposure correction, the number of ON events falling into the test position, the number of OFF events within the background control region, the ratio between ON and OFF region α , the number of excess events, the signal to background ratio, and the significance (equation 17 of Li & Ma (1983)).

Source	Livetime	ON	OFF	α	Excess	S/B	σ
Nova Sgr 2015 No. 2	2.6 h	150	2089	0.07	3.1	0.02	0.24

Differential upper limits for 95% confidence were derived in four equidistant bins in log spaces from 0.2 TeV to 5.9 TeV. As spectral shape a power law was assumed with

an index of 2.42 matching the observations at HE by Cheung et al. (2016). Following Rolke & López (2001), the *TRolke* implementation in the H.E.S.S. software was used to calculate the limits. Systematic uncertainties have not been taken into account. The result is listed in table 6.3.

Table 6.3: Differential upper limits derived for Nova Sgr 2015 No. 2: Following Rolke & López (2001), the *TRolke* implementation in the H.E.S.S. software was used to calculate the limits.

E [TeV]	E_{\min} [TeV]	E_{\max} [TeV]	95 % differential upper limits [$\text{TeV}^{-1}\text{s}^{-1}\text{cm}^{-2}$]
0.31	0.2	0.47	$< 2.12 \times 10^{-11}$
0.71	0.47	1.09	$< 4.15 \times 10^{-12}$
1.66	1.09	2.54	$< 5.40 \times 10^{-13}$
3.88	2.54	5.93	$< 2.12 \times 10^{-13}$

6.3.3 *Fermi*-LAT Data Set

The nova was detected by *Fermi*-LAT and the results were published in Cheung et al. (2016). Figure 6.4 on the left shows the light curve of the source and the exposure time on the source. The observation was partially conducted as a ToO which explains the higher exposure in the first fifteen days. Emission from the source was detected for 55 days.

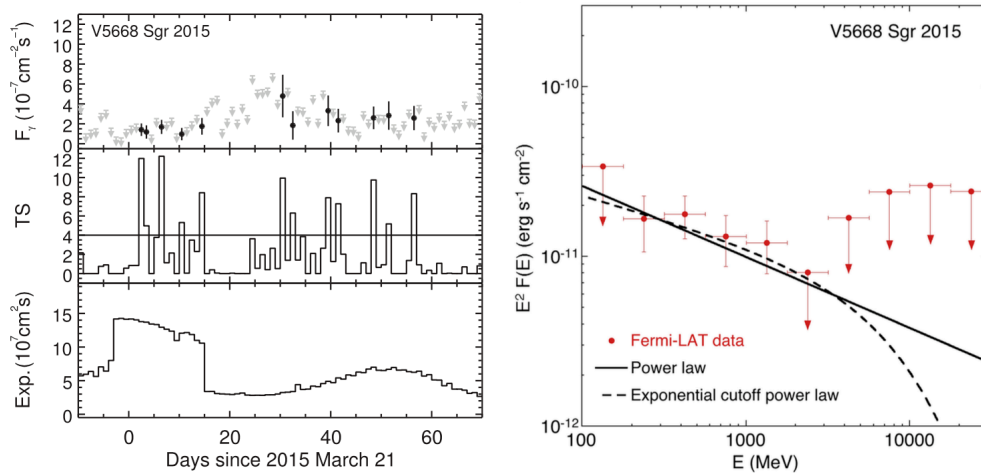


Figure 6.4: *Fermi*-LAT results for Nova Sgr 2015 No. 2: On the left the light curve and exposure on the source is shown. On the right the spectrum of the source is shown with the best fit power-law model (solid line) compared to an exponential cut off power-law model. The plots are taken from Cheung et al. (2016).

On the right in figure 6.4, the spectral result of the source is shown. The source is best fitted with a point source model. The emission is best described by a power law with a slope of 2.42 ± 0.13 and a total flux above 100 MeV of $(11.4 \pm 2.2) \times 10^{-8} \text{ cm}^{-2} \text{ s}^{-1}$. The total TS is 70.4. The improvement in test statistics due to more complex models is negligible.

6.3.4 Interpretation

No VHE emission was detected from Nova Sgr 2015 No. 2 with H.E.S.S. Nevertheless, following the expectation from Metzger et al. (2015) and the simulations of Ahnen et al. (2015), the ratio of hadronic emission from neutral pion decay L_p to inverse Compton from electrons L_e was estimated. The individual components, namely the model for inverse Compton emission, neutral pion decay, and pair production for V 339 Del shown in Ahnen et al. (2015) figure 2 were scaled individually to match the measured excess and upper limits for Nova Sgr 2015 No. 2. The extent and strength of the photosphere of Nova Sgr 2015 No. 2 and V 339 Del has to be identical for this simple approach. For the Nova Sgr 2015 No. 2 no precise measurement is available, but according to the information in Cheung et al. (2016) the evolution of the system is comparable to V 339 Del.

The strength of γ -ray emission from hadronic interaction strongly depends on the dynamic time scale of the system because this limits the time during which hadrons are accelerated. A typical dynamic time scale is ten days (Ahnen et al., 2015). The γ -ray emission is caused by the cooling of the protons which depends on the speed of the ejecta and the mass of the total ejecta. By comparing the dynamic time scales and the cooling time, Ahnen et al. (2015) concluded that the cooling becomes dominant only after tens of days. The H.E.S.S. observations were taken well inside this time window.

Figure 6.5 shows the resulting spectral energy distribution of the H.E.S.S. and *Fermi-LAT* observation. The model scaled to this observation is shown as well. The ratio of hadronic emission from neutral pion decay L_p to inverse Compton from electrons L_e was estimated to be $\lesssim 45\%$. Considering that the MAGIC data set on V 339 Del in which Ahnen et al. (2015) concluded that $L_p/L_e \lesssim 15\%$, is a factor of five deeper than this data set and the data was taken in a two telescope configuration, the result is reasonable.

Assuming an observation with the full H.E.S.S. array with an observation time of 20 h, and the spectral parameter of the proton component in figure 2 of Ahnen et al. (2015), a detection would have been possible.

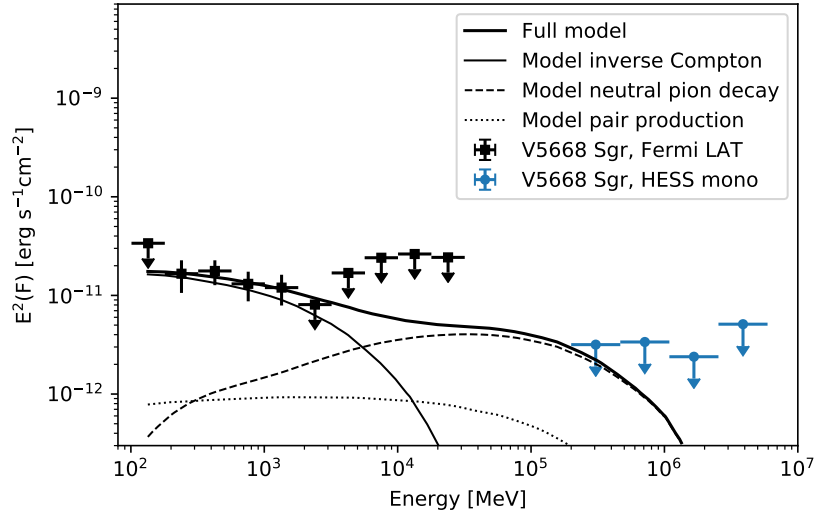


Figure 6.5: Spectral energy distribution for Nova Sgr 2015 No. 2: In black the data points and upper limits from Cheung et al. (2016) are shown. In blue the 95 % upper limits from the H.E.S.S. observation is shown. The emission model components are taken from Ahnen et al. (2015) and rescaled to this results.

6.4 Target of Opportunity Observation Program of Novae with H.E.S.S.

This work was presented during an internal H.E.S.S. Galactic working group meeting. It was concluded that the ToO program for classical novae in H.E.S.S. should emphasize that a deep data set of 20 h is needed. Furthermore, the observation should take place as close as possible to the optical peak based on the argument of Ahnen et al. (2015) and recent measurements of Li et al. (2017) showing a correlation of the optical light-curve and the *Fermi-LAT* light curve. As part of the program for 2018 it is planned that an observation is triggered when a nova is detected by *Fermi-LAT* and/or a nova with a visible magnitude of 9 is detected. The following observations should aim for 20 h with the full array.

6.5 Summary

The Classical Nova Sgr 2015 No. 2 is the first classical nova observed with H.E.S.S. phase II. The results of the analysis are presented here and put into a context with the *Fermi-LAT* observations on the same source. The ratio of hadronic emission from

neutral pion decay L_p to inverse Compton from electrons L_e was estimated to be smaller than 45 % adjusting the simulation results of Ahnen et al. (2015) for V 339 Del. While this result shows that the H.E.S.S. observations were less constraining than another study of Ahnen et al. (2015) on V 339 Del, which constrains the same ratio to be smaller than 15 %, this analysis shows the capability of H.E.S.S. for a competitive study. It is worth mentioning that the results from Ahnen et al. (2015) were achieved with a five times deeper data set. Limited observability and weather prevented a deeper H.E.S.S. data set on Nova Sgr 2015 No. 2. Nevertheless, this study shows the capability of H.E.S.S. to study transient Galactic phenomena like classical novae. Partially based on the experience presented in this study, the ToO program of H.E.S.S. has been adjusted.

7 Conclusions and Outlook

The origin of CRs, their energy distribution, and their composition is a subject of active research even though the existence of CRs has been known for a century. Since the information of their directional information is lost on their way to Earth and since the flux is low, studies of very energetic CRs are complex. By studying VHE γ -rays, IACTs evolved to a major tool in studying CR sources. Furthermore, IACTs revealed properties of γ -ray emitters previously unknown.

By imaging the Cherenkov light from EAS induced by γ -rays from astrophysical sources with sensitive and fast PMT cameras, IACTs measure the energy and astrophysical origin of γ -rays from cosmic sources. One key aspect of the technique is the reflective dish of each telescope. The limited number of Cherenkov photons per EAS requires large mirror areas. In case of the newest fifth telescope of H.E.S.S. phase II, 876 hexagonal mirror segments are used with a total mirror area of 614 m². For the first four telescopes with a dish diameter of 12 m, the telescopes are equipped with 381 round mirror segments each, which results in a total mirror area of 108 m². The precise alignment of the mirror segments is one of the challenges of operating an IACT. Here, the first results of the mirror alignment and control system of H.E.S.S. phase II has been presented after a successful alignment of CT5 mirror segments. Results from a re-alignment campaign that became necessary due to a calibration problem of the tracking system is presented as well. Before the alignment, other improvements were introduced to the system. The results, including monitoring of the long term stability of the alignment as well as the functionality of the hard- and software components, were presented here and also in Gottschall et al. (2015).

After an replacement of degraded mirror segments of CT3, one of the 12 m telescopes of H.E.S.S., the alignment system was reactivated, an alignment was done and the results were measured. The alignment system of CT1-4 has been developed and built by the Universität Hamburg. After the previous mirror exchange in 2010, the alignment system was no longer used or maintained. After not having been used in seven years, the alignment system was serviced as part of this work and performed as expected afterwards. The telescope regained a major part of the original optical efficiency because of the newly coated mirror segments.

The sensitivity level of current IACT experiments, amongst many other things, opened up a new window of follow-up observations of transient phenomena like flaring AGNs, gravitational waves, novae, GRBs, and many more. Especially for GRBs an immediate follow-up is crucial because of their duration of only up to tens of seconds. Hence, CT5 supports a fast tracking system where the telescope can be moved through zenith reducing the angular distance to the target. The dish bending and the bending of the mirror support structure has a negative impact on the mirror alignment when the telescope moves through zenith. This effect was studied with the conclusion that the long term stability of the alignment is not in danger and the negative impact on the γ -rays sensitivity is acceptable. Therefore, the system is operated including the fast follow-up tracking described above. The first results of the GRB follow-up program of H.E.S.S. phase II were presented by Hoischen et al. (2017).

Since the beginning of H.E.S.S., a survey observation of the Galactic plane was done. Together with pointed observations in the Galactic plane, this data set provides a wide coverage of the Galactic plane with unprecedented sensitivity. Based on this data set, a systematic search for sources showing a shell morphology was done. A shell morphology is a strong hint towards a super nova remnant scenario for the emission. Four candidates were discovered and studied in detail. The newly discovered source HESS J1534–571 was classified as super nova remnant because of the association with the radio SNR candidate G323.7–1.0. The previously known sources HESS J1614–518 and HESS J1912+101 are now classified as SNR candidates based on this study. In total the number of sources with confirmed shell morphology in the Galactic survey region of H.E.S.S. was almost doubled by this search. This study presents the first time SNR candidates were selected by their TeV morphology. After presenting this work at conferences, a lot of interest was generated in the community leading to follow-up work in the GeV and radio band. The available MWL data was also examined as part of this work. The main focus was to investigate the possibility of a purely hadronic or leptonic scenario. Since the lack of X-ray emission is not constraining and a purely hadronic scenario is feasible based on the spectral analysis and the study of gas densities and possible distances, both scenarios or a mixture of both is possible. The results were published in H.E.S.S. Collaboration (2018a).

As part of the target of opportunity observation program of H.E.S.S., the Galactic nova Nova Sgr 2015 No. 2 was observed. Emission up to GeV energies from these novae are one of the puzzling discoveries of *Fermi-LAT*. Detecting or constraining the emission at TeV energies could improve the understanding of the processes in nova explosions significantly. The question whether the HE γ -ray emission is produced by shock interaction in the ejecta of the nova or in a bow-shock with the ISM is an open question at the time of writing this thesis. No emission was detected with H.E.S.S. from the Nova

Sgr 2015 No. 2. Upper limits were derived to constrain the maximum luminosity from hadronic interaction. It was estimated that the luminosity from hadronic interaction cannot be more than 45 % of the luminosity of the inverse Compton component. With upcoming observations H.E.S.S. should be able to constrain this ratio to less than 10 % or to detect this emission component. The results from this study were used to update the ToO program of H.E.S.S.

For this work and the service work to the collaboration including observation shifts, hardware and software maintenance, and the contribution to the regular in run coordination meetings, the H.E.S.S. collaboration awarded the author with the H.E.S.S. prize. With the HESS Prize the collaboration acknowledges a young scientist (PhD, postdoc, junior staff) who made an outstanding service contributions to the experiment. The prize is awarded twice a year. A full publication list of the author can be found in the Curriculum Vitae.

The work on the mirror alignment system also provided input for the future observatory CTA, especially the validation of the durability of the mechanical design of the CT5 actuators. The author contributed to the development of a mirror control system and a mirror testing facility for CTA at the IAAT (Dick et al., 2015). With its improved angular resolution, sensitivity, and flexibility CTA will provide valuable insights for all astrophysical topics discussed in this work. More radio and X-ray quiet SNRs are expected to be found with an improved sensitivity and energy coverage as well as an improved resolution of the shells. Furthermore, if counterparts in other wavebands are known, a refined correlation study between wavebands is possible. Following up on triggers of other wavebands, for example in the case of novae, is one of the key projects of CTA.

Bibliography

- AAB, A.; ABREU, P.; AGLIETTA, M.; AHN, E.J.; SAMARAI, I.A.; ET AL., 2015: Searches for Anisotropies in the Arrival Directions of the Highest Energy Cosmic Rays Detected by the Pierre Auger Observatory. *The Astrophysical Journal*, 804:15.
- AARTSEN, M.G.; ABRAHAM, K.; ACKERMANN, M.; ADAMS, J.; AGUILAR, J.A.; ET AL., 2016: Observation and Characterization of a Cosmic Muon Neutrino Flux from the Northern Hemisphere Using Six Years of IceCube Data. *The Astrophysical Journal*, 833:3.
- ABBOTT, B.P.; ABBOTT, R.; ABBOTT, T.D.; ABERNATHY, M.R.; ACERNESE, F.; ET AL., 2016: Observation of Gravitational Waves from a Binary Black Hole Merger. *Physical Review Letters*, 116(6):061102.
- ABBOTT, B.P.; ABBOTT, R.; ABBOTT, T.D.; ACERNESE, F.; ACKLEY, K.; ET AL., 2017: Gravitational Waves and Gamma-Rays from a Binary Neutron Star Merger: GW170817 and GRB 170817A. *The Astrophysical Journal Letters*, 848:L13.
- ABDO, A.A.; ACKERMANN, M.; AJELLO, M.; ATWOOD, W.B.; BALDINI, L.; ET AL., 2010: Gamma-Ray Emission Concurrent with the Nova in the Symbiotic Binary V407 Cygni. *Science*, 329:817–821.
- ABEYSEKARA, A.U.; ALBERT, A.; ALFARO, R.; ALVAREZ, C.; ÁLVAREZ, J.D.; ET AL., 2017: The 2HWC HAWC Observatory Gamma-Ray Catalog. *The Astrophysical Journal*, 843:40.
- ABRAHAM, J.; AGLIETTA, M.; AGUIRRE, I.C.; ALBROW, M.; ALLARD, D.; ET AL., 2004: Properties and performance of the prototype instrument for the Pierre Auger Observatory. *Nuclear Instruments and Methods in Physics Research A*, 523:50–95.
- ABU-ZAYYAD, T.; AIDA, R.; ALLEN, M.; ANDERSON, R.; AZUMA, R.; ET AL., 2012: Search for Anisotropy of Ultrahigh Energy Cosmic Rays with the Telescope Array Experiment. *The Astrophysical Journal*, 757.
- ACERO, F.; ACKERMANN, M.; AJELLO, M.; ALBERT, A.; ATWOOD, W.B.; ET AL., 2015: Fermi Large Area Telescope Third Source Catalog. *The Astrophysical Journal Supplement Series*, 218:23.

- ACERO, F.; AHARONIAN, F.; AKHPERJANIAN, A.G.; ANTON, G.; BARRES DE ALMEIDA, U.; ET AL., 2010: First detection of VHE γ -rays from SN 1006 by HESS. *Astronomy & Astrophysics*, 516:A62.
- ACHARYA, B.S.; ACTIS, M.; AGHAJANI, T.; AGNETTA, G.; AGUILAR, J.; ET AL., 2013: Introducing the CTA concept. *Astroparticle Physics*, 43:3–18.
- ACKERMANN, M.; AJELLO, M.; ALBERT, A.; BALDINI, L.; BALLETT, J.; ET AL., 2014: Fermi establishes classical novae as a distinct class of gamma-ray sources. *Science*, 345:554–558.
- ACKERMANN, M.; AJELLO, M.; ALLAFORT, A.; BALDINI, L.; BALLETT, J.; ET AL., 2013: Detection of the Characteristic Pion-Decay Signature in Supernova Remnants. *Science*, 339:807–811.
- ACKERMANN, M.; AJELLO, M.; ATWOOD, W.B.; BALDINI, L.; BALLETT, J.; ET AL., 2016: 2FHL: The Second Catalog of Hard Fermi-LAT Sources. *The Astrophysical Journal Supplement Series*, 222:5.
- ADAMS, J.H.; AHMAD, S.; ALBERT, J.N.; ALLARD, D.; ANCHORDOQUI, L.; ET AL., 2015: The JEM-EUSO mission: An introduction. *Experimental Astronomy*, 40(1):3–17. ISSN 1572-9508.
- AHARONIAN, F.; AKHPERJANIAN, A.G.; AYE, K.M.; BAZER-BACHI, A.R.; BEILICKE, M.; ET AL., 2004: Calibration of cameras of the H.E.S.S. detector. *Astroparticle Physics*, 22:109–125.
- AHARONIAN, F.; AKHPERJANIAN, A.G.; BARRES DE ALMEIDA, U.; BAZER-BACHI, A.R.; BEHERA, B.; ET AL., 2008a: Discovery of very-high-energy γ -ray emission from the vicinity of PSR J1913+1011 with HESS. *Astronomy & Astrophysics*, 484:435–440.
- AHARONIAN, F.; AKHPERJANIAN, A.G.; BARRES DE ALMEIDA, U.; BAZER-BACHI, A.R.; BEHERA, B.; ET AL., 2008b: HESS very-high-energy gamma-ray sources without identified counterparts. *Astronomy & Astrophysics*, 477:353–363.
- AHARONIAN, F.; AKHPERJANIAN, A.G.; BAZER-BACHI, A.R.; BEHERA, B.; BEILICKE, M.; ET AL., 2008c: Discovery of very high energy gamma-ray emission coincident with molecular clouds in the W 28 (G6.4-0.1) field. *Astronomy & Astrophysics*, 481:401–410.
- AHARONIAN, F.; AKHPERJANIAN, A.G.; BAZER-BACHI, A.R.; BEILICKE, M.; BENBOW, W.; ET AL., 2006a: A detailed spectral and morphological study of the gamma-ray supernova remnant RX J1713.7-3946 with HESS. *Astronomy & Astrophysics*, 449:223–242.

-
- AHARONIAN, F.; AKHPERJANIAN, A.G.; BAZER-BACHI, A.R.; BEILICKE, M.; BENBOW, W.; ET AL., 2006b: Observations of the Crab Nebula with HESS. *Astronomy & Astrophysics*, 457:899–915.
- AHARONIAN, F.; AKHPERJANIAN, A.G.; BAZER-BACHI, A.R.; BEILICKE, M.; BENBOW, W.; ET AL., 2006c: The H.E.S.S. Survey of the Inner Galaxy in Very High Energy Gamma Rays. *The Astrophysical Journal*, 636:777–797.
- AHARONIAN, F.; AKHPERJANIAN, A.G.; BAZER-BACHI, A.R.; BEILICKE, M.; BENBOW, W.; ET AL., 2007: H.E.S.S. Observations of the Supernova Remnant RX J0852.0-4622: Shell-Type Morphology and Spectrum of a Widely Extended Very High Energy Gamma-Ray Source. *The Astrophysical Journal*, 661:236–249.
- AHARONIAN, F.; BERGSTRÖM, L.; DERMER, C., 2013: Astrophysics at Very High Energies. *Astrophysics at Very High Energies: Saas-Fee Advanced Course 40. Swiss Society for Astrophysics and Astronomy, Saas-Fee Advanced Course, Volume 40. ISBN 978-3-642-36133-3. Springer-Verlag Berlin Heidelberg, 2013*, 40.
- AHARONIAN, F.A.; ATOYAN, A.M.; KIFUNE, T., 1997: Inverse Compton gamma radiation of faint synchrotron X-ray nebulae around pulsars. *Monthly Notices of the Royal Astronomical Society*, 291:162–176.
- AHNEN, M.L.; ANSOLDI, S.; ANTONELLI, L.A.; ANTORANZ, P.; BABIC, A.; ET AL., 2015: Very high-energy γ -ray observations of novae and dwarf novae with the MAGIC telescopes. *Astronomy & Astrophysics*, 582:A67.
- AKAIKE, H., 1974: A New Look at the Statistical Model Identification. *IEEE Transactions on Automatic Control*, 19:716–723.
- ALIU, E.; ARCHAMBAULT, S.; ARLEN, T.; AUNE, T.; BEILICKE, M.; ET AL., 2012: VERITAS Observations of the Nova in V407 Cygni. *The Astrophysical Journal*, 754:77.
- ANDERSON, C.D., 1933: The Positive Electron. *Physical Review*, 43:491–494.
- ARAYA, M., 2017: Detection of GeV Gamma-Rays from HESS J1534-571 and Multi-wavelength Implications for the Origin of the Nonthermal Emission. *The Astrophysical Journal*, 843:12.
- ARNAUD, K.; SMITH, R.; SIEMIGINOWSKA, A., 2011: Handbook of X-ray Astronomy. Cambridge Observing Handbooks for Research Astronomers, Cambridge University Press. ISBN 9781139502566.
- ASCHENBACH, B., 1995: ROSAT Results on Supernova Remnants. A. Ferrara; C.F. McKee; C. Heiles; P.R. Shapiro, editors, *The Physics of the Interstellar Medium*

- and Intergalactic Medium, vol. 80 of *Astronomical Society of the Pacific Conference Series*, page 432.
- ATWOOD, W.B.; ABDO, A.A.; ACKERMANN, M.; ALTHOUSE, W.; ANDERSON, B.; ET AL., 2009: The Large Area Telescope on the Fermi Gamma-Ray Space Telescope Mission. *The Astrophysical Journal*, 697:1071–1102.
- BADENES, C.; MAOZ, D.; DRAINE, B.T., 2010: On the size distribution of supernova remnants in the Magellanic Clouds. *Monthly Notices of the Royal Astronomical Society*, 407:1301–1313.
- BAMBA, A.; UENO, M.; KOYAMA, K.; YAMAUCHI, S., 2001: A Diffuse X-Ray Source, AX J1843.8-0352: Association with the Radio Complex G28.6-0.1 and Identification of a New Supernova Remnant. *Publications of the Astronomical Society of Japan*, 53:L21–L24.
- BAMBA, A.; UENO, M.; KOYAMA, K.; YAMAUCHI, S., 2003: Diffuse Hard X-Ray Sources Discovered with the ASCA Galactic Plane Survey. *The Astrophysical Journal*, 589:253–260.
- BERGE, D.; FUNK, S.; HINTON, J., 2007: Background modelling in very-high-energy γ -ray astronomy. *Astronomy & Astrophysics*, 466:1219–1229.
- BERNLÖHR, K., 2008: Simulation of imaging atmospheric Cherenkov telescopes with CORSIKA and sim_telarray. *Astroparticle Physics*, 30:149–158.
- BERNLÖHR, K.; CARROL, O.; CORNILS, R.; ELFAHEM, S.; ESPIGAT, P.; ET AL., 2003: The optical system of the H.E.S.S. imaging atmospheric Cherenkov telescopes. Part I: layout and components of the system. *Astroparticle Physics*, 20:111–128.
- BODE, M.; EVANS, A., 2008: Classical Novae. Cambridge Astrophysics, Cambridge University Press. ISBN 9781139469555.
- BOLMONT, J.; CORONA, P.; GAURON, P.; GHISLAIN, P.; GOFFIN, C.; ET AL., 2014: The camera of the fifth H.E.S.S. telescope. Part I: System description. *Nuclear Instruments and Methods in Physics Research A*, 761:46–57.
- BOLZ, O., 2004: Absolute Energiekalibration der abbildenden Cherenkov-Teleskope des H.E.S.S. Experiments und Ergebnisse erster Beobachtungen des Supernova-Überrests RX J1713.7-3946. Ph.D. thesis.
- BRAUN, I., 2007: Improving the Pointing Precision of the H.E.S.S. Experiment. Ph.D. thesis, Ruprecht-Karls-Universität Heidelberg.
- BURNHAM, K.; ANDERSON, D., 2013: Model Selection and Inference: A Practical Information-Theoretic Approach, Springer New York. ISBN 9781475729177.

- CAREY, S.J.; NORIEGA-CRESPO, A.; MIZUNO, D.R.; SHENOY, S.; PALADINI, R.; ET AL., 2009: MIPS GAL: A Survey of the Inner Galactic Plane at 24 and 70 μm . *Publications of the Astronomical Society of the Pacific*, 121:76–97.
- CASE, G.L.; BHATTACHARYA, D., 1998: A New Σ -D Relation and Its Application to the Galactic Supernova Remnant Distribution. *The Astrophysical Journal*, 504:761–772.
- CASH, W., 1979: Parameter estimation in astronomy through application of the likelihood ratio. *The Astrophysical Journal*, 228:939–947.
- CHANG, C.; KONOPELKO, A.; CUI, W., 2008: Search for Pulsar Wind Nebula Associations with Unidentified TeV γ -Ray Sources. *The Astrophysical Journal*, 682:1177–1184.
- CHEUNG, C.C.; JEAN, P.; FERMI LARGE AREA TELESCOPE COLLABORATION; SHORE, S.N., 2015a: Fermi-LAT Gamma-ray Observations of Nova Sagittarii 2015 No. 2. *The Astronomer's Telegram*, 7283.
- CHEUNG, C.C.; JEAN, P.; SHORE, S.N., 2015b: Further Fermi-LAT Gamma-ray Observations of Nova Sagittarii 2015 No. 2. *The Astronomer's Telegram*, 7315.
- CHEUNG, C.C.; JEAN, P.; SHORE, S.N.; STAWARZ, Ł.; CORBET, R.H.D.; ET AL., 2016: Fermi-LAT Gamma-Ray Detections of Classical Novae V1369 Centauri 2013 and V5668 Sagittarii 2015. *The Astrophysical Journal*, 826:142.
- CHOMIUK, L.; LINFORD, J.D.; YANG, J.; O'BRIEN, T.J.; PARAGI, Z.; ET AL., 2014: Binary orbits as the driver of γ -ray emission and mass ejection in classical novae. *Nature*, 514:339–342.
- CHURCHWELL, E.; BABLER, B.L.; MEADE, M.R.; WHITNEY, B.A.; BENJAMIN, R.; ET AL., 2009: The Spitzer/GLIMPSE Surveys: A New View of the Milky Way. *Publications of the Astronomical Society of the Pacific*, 121:213–230.
- CLAYTON, D.D., 1981: Li-7 gamma-ray lines from novae. *The Astrophysical Journal Letters*, 244:L97.
- CONDON, J.J.; COTTON, W.D.; GREISEN, E.W.; YIN, Q.F.; PERLEY, R.A.; ET AL., 1998: The NRAO VLA Sky Survey. *The Astronomical Journal*, 115:1693–1716.
- CORNILS, R., 2006: Justierung und Abbildungsfunktion der H.E.S.S.-Reflektoren sowie Untersuchung der ultraleuchtkräftigen Infrarot-Galaxie Arp 220 mit dem H.E.S.S.-Telekopsystem. Ph.D. thesis, Ruprecht-Karls-Universität Heidelberg.

- CORNILS, R.; GILLESSEN, S.; JUNG, I.; HOFMANN, W.; BEILICKE, M.; ET AL., 2003: The optical system of the H.E.S.S. imaging atmospheric Cherenkov telescopes. Part II: mirror alignment and point spread function. *Astroparticle Physics*, 20:129–143.
- DAME, T.M.; HARTMANN, D.; THADDEUS, P., 2001: The Milky Way in Molecular Clouds: A New Complete CO Survey. *The Astrophysical Journal*, 547:792–813.
- DE NAUROIS, M.; ROLLAND, L., 2009: A high performance likelihood reconstruction of γ -rays for imaging atmospheric Cherenkov telescopes. *Astroparticle Physics*, 32:231–252.
- DEIL, C.; VAN ELDIK, C.; FÖRSTER, A.; HERMANN, G.; HOFMANN, W.; ET AL., 2008: H.E.S.S. II-Telescope Structure, Reflector and Drive System. F.A. Aharonian; W. Hofmann; F. Rieger, editors, American Institute of Physics Conference Series, vol. 1085 of *American Institute of Physics Conference Series*, pages 693–695.
- DICK, J.; BONARDI, A.; BRESSEL, S.; CAPASSO, M.; DIEBOLD, S.; ET AL., 2015: Recent developments for testing of Cherenkov Telescope Array mirrors and actuators in Tuebingen. Proceedings of the 34th International Cosmic Ray Conference (ICRC2015). 30 July - 6 August, 2015. The Hague, The Netherlands, vol. 34.
- DUBNER, G.; GIACANI, E., 2015: Radio emission from supernova remnants. *The Astronomy & Astrophysics Review*, 23:3.
- EADIE, W., 1971: Statistical methods in experimental physics, North-Holland Pub. Co.
- FERMI, E., 1949: On the Origin of the Cosmic Radiation. *Physical Review*, 75:1169–1174.
- FRASCHETTI, F., 2008: On the acceleration of ultra-high-energy cosmic rays. *Philosophical Transactions of the Royal Society of London Series A*, 366:4417–4428.
- FUNK, S., 2005: A new population of very high-energy gamma-ray sources detected with H.E.S.S. in the inner part of the Milky Way. Ph.D. thesis, <http://www.ub.uni-heidelberg.de/archiv/5542>.
- FUNK, S.; HERMANN, G.; HINTON, J.; BERGE, D.; BERNLÖHR, K.; ET AL., 2004: The trigger system of the H.E.S.S. telescope array. *Astroparticle Physics*, 22:285–296.
- GAISSER, T., 2017: Challenges for cosmic-ray experiments. European Physical Journal Web of Conferences, vol. 145 of *European Physical Journal Web of Conferences*, page 18003.
- GAISSER, T.K.; ENGEL, R.; RESCONI, E., 2016: Cosmic Rays and Particle Physics.

-
- GIAVITTO, G., 2006: Reflectivity measurements on mirrors for Cherenkov telescopes. Master's thesis, Università degli Studi di Trieste.
- GOLDSTEIN, A.; VERES, P.; BURNS, E.; BRIGGS, M.S.; HAMBURG, R.; ET AL., 2017: An Ordinary Short Gamma-Ray Burst with Extraordinary Implications: Fermi-GBM Detection of GRB 170817A. *The Astrophysical Journal*, 848.
- GOTTSCHALL, D., 2013: Development of a PDM-Simulator Board for JEM-EUSO. Master's thesis, Eberhard Karls Universität Tübingen.
- GOTTSCHALL, D.; CAPASSO, M.; DEIL, C.; DJANNATI-ATAI, A.; DONATH, A.; ET AL., 2017: Discovery of new TeV supernova remnant shells in the Galactic plane with H.E.S.S. 6th International Symposium on High Energy Gamma-Ray Astronomy, vol. 1792 of *American Institute of Physics Conference Series*, page 040030.
- GOTTSCHALL, D.; FÖRSTER, A.; BONARDI, A.; SANTANGELO, A.; PUEHLHOFER, G., 2015: The Mirror Alignment and Control System for CT5 of the H.E.S.S. experiment. 34th International Cosmic Ray Conference (ICRC2015), vol. 34 of *International Cosmic Ray Conference*, page 1017.
- GREEN, A.J.; REEVES, S.N.; MURPHY, T., 2014: The Second Epoch Molonglo Galactic Plane Survey: Images and Candidate Supernova Remnants. *Publications of the Astronomical Society of Australia*, 31:e042.
- GREISEN, K., 1966: End to the Cosmic-Ray Spectrum? *Physical Review Letters*, 16:748–750.
- GRIEDER, P., 2010: Extensive Air Showers: High Energy Phenomena and Astrophysical Aspects - A Tutorial, Reference Manual and Data Book. Astrophysics and space science library, Springer Berlin Heidelberg. ISBN 9783540769415.
- HAHN, J.; DE LOS REYES, R.; BERNLÖHR, K.; KRÜGER, P.; LO, Y.T.E.; ET AL., 2014: Impact of aerosols and adverse atmospheric conditions on the data quality for spectral analysis of the H.E.S.S. telescopes. *Astroparticle Physics*, 54:25–32.
- HAVERKORN, M.; GAENSLER, B.M.; MCCLURE-GRIFFITHS, N.M.; DICKEY, J.M.; GREEN, A.J., 2006: The Southern Galactic Plane Survey: Polarized Radio Continuum Observations and Analysis. *The Astrophysical Journal Supplement Series*, 167:230–238.
- HECK, D.; KNAPP, J.; CAPDEVIELLE, J.N.; SCHATZ, G.; THOUW, T., 1998: CORSIKA: a Monte Carlo code to simulate extensive air showers., Forschungszentrum Karlsruhe GmbH, Karlsruhe (Germany).

- HEITLER, W., 1954: The Quantum Theory of Radiation. Dover Books on Physics, Dover Publications. ISBN 9780486645582.
- HELFAND, D.J.; BECKER, R.H.; WHITE, R.L.; FALLON, A.; TUTTLE, S., 2006: MAGPIS: A Multi-Array Galactic Plane Imaging Survey. *The Astronomical Journal*, 131:2525–2537.
- H.E.S.S. COLLABORATION, 2011: A new SNR with TeV shell-type morphology: HESS J1731-347. *Astronomy & Astrophysics*, 531:A81.
- H.E.S.S. COLLABORATION, 2015: The exceptionally powerful TeV γ -ray emitters in the Large Magellanic Cloud. *Science*, 347:406–412.
- H.E.S.S. COLLABORATION, 2017: Gamma-ray blazar spectra with H.E.S.S. II mono analysis: The case of PKS 2155-304 and PG 1553+113. *Astronomy & Astrophysics*, 600:A89.
- H.E.S.S. COLLABORATION, 2018a: A search for new supernove remnant shells in the Galactic plane with H.E.S.S. *Astronomy & Astrophysics*, 612:A8.
- H.E.S.S. COLLABORATION, 2018b: Deeper H.E.S.S. Observations of Vela Junior (RX J0852.0-4622): Morphology Studies and Resolved Spectroscopy. *Astronomy & Astrophysics*, 612:A7.
- H.E.S.S. COLLABORATION, 2018c: Detailed spectral and morphological analysis of the shell type SNR RCW 86. *Astronomy & Astrophysics*, 612:A4.
- H.E.S.S. COLLABORATION, 2018d: The H.E.S.S. Galactic plane survey. *Astronomy & Astrophysics*, 612:A1.
- H.E.S.S. COLLABORATION, 2018e: H.E.S.S. observations of RX J1713.7-3946 with improved angular and spectral resolution; evidence for gamma-ray emission extending beyond the X-ray emitting shell. *Astronomy & Astrophysics*, 612:A6.
- H.E.S.S. COLLABORATION, 2018f: The supernova remnant W49B as seen with H.E.S.S. and Fermi-LAT. *Astronomy & Astrophysics*, 612:A5.
- HILLAS, A.M., 1984: The Origin of Ultra-High-Energy Cosmic Rays. *Annual Review of Astronomy and Astrophysics*, 22:425–444.
- HILLAS, A.M., 1985: Cerenkov light images of EAS produced by primary gamma. *International Cosmic Ray Conference*, 3.
- HOFMANN, W., 1998: Alignment of the hess mirrors using images of stars. *Internal note H.E.S.S.*

-
- HOFVERBERG, P.; KANKANYAN, R.; PANTER, M.; HERMANN, G.; HOFMANN, W.; ET AL., 2013: Commissioning and initial performance of the H.E.S.S. II drive system. *ArXiv e-prints*, 1307.4550.
- HOISCHEN, C.; BALZER, A.; BISSALDI, E.; FÜSSLING, M.; GARRIGOUX, T.; ET AL., 2017: GRB Observations with H.E.S.S. II. *ArXiv e-prints*, 1708.01088.
- HOLLER, M.; BERGE, D.; VAN ELDIK, C.; LENAIN, J.P.; MARANDON, V.; ET AL., 2015: Observations of the Crab Nebula with H.E.S.S. Phase II. *ArXiv e-prints*, 1509.02902.
- JACKSON, J.M.; RATHBORNE, J.M.; SHAH, R.Y.; SIMON, R.; BANIA, T.M.; ET AL., 2006: The Boston University-Five College Radio Astronomy Observatory Galactic Ring Survey. *The Astrophysical Journal Supplement Series*, 163:145–159.
- JELLEY, J., 1958: Cherenkov Radiation and its Applications. *Proceedings of the International Workshop on Very High Energy Gamma Ray Astronomy*, page 64.
- KELNER, S.R.; AHARONIAN, F.A.; BUGAYOV, V.V., 2006: Energy spectra of gamma rays, electrons, and neutrinos produced at proton-proton interactions in the very high energy regime. *Physical Review D*, 74(3):034018.
- KLEPSEK, S.; ASHTON, T.; BACKES, M.; BALZER, A.; BERGE, D.; ET AL., 2017: Hardware and software architecture of the upgraded H.E.S.S. cameras. *ArXiv e-prints*, 1707.04415.
- KLOCHKOV, D.; SULEIMANOV, V.; PÜHLHOFER, G.; YAKOVLEV, D.G.; SANTANGELO, A.; ET AL., 2015: The neutron star in HESS J1731-347: Central compact objects as laboratories to study the equation of state of superdense matter. *Astronomy & Astrophysics*, 573:A53.
- KOTHEK, R.; DOUGHERTY, S.M., 2007: The distance and neutral environment of the massive stellar cluster Westerlund 1. *Astronomy & Astrophysics*, 468:993–1000.
- KOYAMA, K.; TSUNEMI, H.; DOTANI, T.; BAUTZ, M.W.; HAYASHIDA, K.; ET AL., 2007: X-Ray Imaging Spectrometer (XIS) on Board Suzaku. *Publications of the Astronomical Society of Japan*, 59:23–33.
- KRAFT, R.P., 1964: Binary Stars among Cataclysmic Variables. III. Ten Old Novae. *The Astrophysical Journal*, 139:457.
- LANDI, R.; BASSANI, L.; MALIZIA, A.; MASETTI, N.; STEPHEN, J.B.; ET AL., 2006: Swift XRT Follow-up Observations of TeV Sources of the HESS Inner Galaxy Survey. *The Astrophysical Journal*, 651:190–196.

- LI, K.L.; METZGER, B.D.; CHOMIUK, L.; VURM, I.; STRADER, J.; ET AL., 2017: A nova outburst powered by shocks. *Nature Astronomy*, 1:697–702.
- LI, T.P.; MA, Y.Q., 1983: Analysis methods for results in gamma-ray astronomy. *The Astrophysical Journal*, 272:317–324.
- LIN, D.; WEBB, N.A.; BARRET, D., 2012: Classification of X-Ray Sources in the XMM-Newton Serendipitous Source Catalog. *The Astrophysical Journal*, 756:27.
- LONGAIR, M., 2011: High Energy Astrophysics, Cambridge University Press. ISBN 9781139494540.
- LUNDMARK, K., 1921: Suspected New Stars Recorded in Old Chronicles and Among Recent Meridian Observations. *Publications of the Astronomical Society of the Pacific*, 33:225.
- MARTIN, P.; DUBUS, G., 2013: Particle acceleration and non-thermal emission during the V407 Cygni nova outburst. *Astronomy & Astrophysics*, 551:A37.
- MATSUMOTO, H.; UCHIYAMA, H.; SAWADA, M.; TSURU, T.G.; KOYAMA, K.; ET AL., 2008: Discovery of Extended X-Ray Emission from an Unidentified TeV Source, HESS J1614-518, Using the Suzaku Satellite. *Publications of the Astronomical Society of Japan*, 60:S163–S172.
- MATSUNAGA, K.; MIZUNO, N.; MORIGUCHI, Y.; ONISHI, T.; MIZUNO, A.; ET AL., 2001: Detection of Eight Molecular Shells in the Southern Milky Way with NANTEN. *Publications of the Astronomical Society of Japan*, 53:1003–1016.
- MATTHEWS, J., 2005: A Heitler model of extensive air showers. *Astroparticle Physics*, 22:387–397.
- MCCLURE-GRIFFITHS, N.M.; DICKEY, J.M.; GAENSLER, B.M.; GREEN, A.J.; HAVERKORN, M.; ET AL., 2005: The Southern Galactic Plane Survey: H I Observations and Analysis. *The Astrophysical Journal Supplement Series*, 158:178–187.
- METZGER, B.D.; FINZELL, T.; VURM, I.; HASCOËT, R.; BELOBORODOV, A.M.; ET AL., 2015: Gamma-ray novae as probes of relativistic particle acceleration at non-relativistic shocks. *Monthly Notices of the Royal Astronomical Society*, 450:2739–2748.
- MEYER, M.; HORNS, D.; ZEHLIN, H.S., 2010: The Crab Nebula as a standard candle in very high-energy astrophysics. *Astronomy & Astrophysics*, 523:A2.
- MIRZOYAN, R., 2014: Brief history of ground-based very high energy gamma-ray astrophysics with atmospheric air Cherenkov telescopes. *Astroparticle Physics*, 53:91–99.

- MITCHELL, A., 2016: Optical Efficiency Calibration for Inhomogeneous IACT Arrays and a Detailed Study of the Highly Extended Pulsar Wind Nebula HESS J1825–137. Ph.D. thesis, Ruperto-Carola-University of Heidelberg, Germany.
- MITCHELL, A.M.W.; PARSONS, R.D.; HOFMANN, W.; BERNLÖHR, K., 2016: Cross calibration of telescope optical throughput efficiencies using reconstructed shower energies for the Cherenkov Telescope Array. *Astroparticle Physics*, 75:1–7.
- MITSUMA, K.; BAUTZ, M.; INOUE, H.; KELLEY, R.L.; KOYAMA, K.; ET AL., 2007: The X-Ray Observatory Suzaku. *Publications of the Astronomical Society of Japan*, 59:1–7.
- MORALES, E.F.E.; WYROWSKI, F.; SCHULLER, F.; MENTEN, K.M., 2013: Stellar clusters in the inner Galaxy and their correlation with cold dust emission. *Astronomy & Astrophysics*, 560:A76.
- MURACH, T.; GAJDUS, M.; PARSONS, R., 2015: A Neural Network-based Reconstruction Algorithm for monoscopically detected Air Showers observed with the H.E.S.S. Experiment. Proceedings of the 34th International Cosmic Ray Conference (ICRC2015). 30 July - 6 August, 2015. The Hague, The Netherlands., vol. 34.
- MURPHY, T.; MAUCH, T.; GREEN, A.; HUNSTEAD, R.W.; PIESTRZYNSKA, B.; ET AL., 2007: The second epoch Molonglo Galactic Plane Survey: compact source catalogue. *Monthly Notices of the Royal Astronomical Society*, 382:382–392.
- OHM, S.; VAN ELDIK, C.; EGBERTS, K., 2009: γ /hadron separation in very-high-energy γ -ray astronomy using a multivariate analysis method. *Astroparticle Physics*, 31:383–391.
- PACINI, D., 1912: La radiazione penetrante alla superficie ed in seno alle acque. *Il Nuovo Cimento*, 3:93–100.
- PARSONS, R.; BALZER, A.; FUESSLING, M.; HOISCHEN, C.; HOLLER, M.; ET AL., 2015a: The H.E.S.S. II GRB Observation Program. 34th International Cosmic Ray Conference (ICRC2015), vol. 34 of *International Cosmic Ray Conference*, page 853.
- PARSONS, R.; MURACH, T.; GAJDUS, M., 2015b: H.E.S.S. II Data Analysis with IMPACT. 34th International Cosmic Ray Conference (ICRC2015), vol. 34 of *International Cosmic Ray Conference*, page 826.
- PARSONS, R.D.; HINTON, J.A., 2014: A Monte Carlo template based analysis for air-Cherenkov arrays. *Astroparticle Physics*, 56:26–34.
- PFEFFERMANN, E.; ASCHENBACH, B.; PREDEHL, P., 1991: Discovery of a galactic supernova remnant with ROSAT. *Astronomy & Astrophysics*, 246:L28–L31.

- PIATTI, A.E.; CLARIÁ, J.J.; BICA, E., 2000: Photometric and integrated spectral study of the young open clusters Pismis 22, NGC 6178, NGC 6216 and Ruprecht 130. *Astronomy & Astrophysics*, 360:529–538.
- PIRAN, T., 1999: Gamma-ray bursts and the fireball model. *Physics Reports*, 314:575–667.
- PRICE, S.D.; EGAN, M.P.; CAREY, S.J.; MIZUNO, D.R.; KUCHAR, T.A., 2001: Mid-course Space Experiment Survey of the Galactic Plane. *The Astronomical Journal*, 121:2819–2842.
- PÜHLHOFER, G.; BRUN, F.; CAPASSO, M.; CHAVES, R.C.G.; DEIL, C.; ET AL., 2015: Search for new supernova remnant shells in the Galactic plane with H.E.S.S. *ArXiv e-prints*, 1509.03872.
- REAMES, D.V., 2013: The Two Sources of Solar Energetic Particles. *Space Science Reviews*, 175:53–92.
- ROLKE, W.A.; LÓPEZ, A.M., 2001: Confidence intervals and upper bounds for small signals in the presence of background noise. *Nuclear Instruments and Methods in Physics Research A*, 458:745–758.
- SAKAI, M.; YAJIMA, Y.; MATSUMOTO, H., 2011: Nature of the Unidentified TeV Source HESS J1614-518, Revealed by Suzaku and XMM-Newton Observations. *Publications of the Astronomical Society of Japan*, 63:S879–S887.
- SANTANGELO, A.; MADONIA, R., 2014: Fifty years of X-ray astronomy: A look back and into the (near) future. *Astroparticle Physics*, 53:130–151.
- SAVCHENKO, V.; FERRIGNO, C.; KUULKERS, E.; BAZZANO, A.; BOZZO, E.; ET AL., 2017: INTEGRAL Detection of the First Prompt Gamma-Ray Signal Coincident with the Gravitational-wave Event GW170817. *The Astrophysical Journal*, 848.
- SCHÜSSLER, F.; BACKES, M.; BALZER, A.; BRUN, F.; FÜSSLING, M.; ET AL., 2017: The H.E.S.S. multi-messenger program: Searches for TeV gamma-ray emission associated with high-energy neutrinos. 6th International Symposium on High Energy Gamma-Ray Astronomy, vol. 1792 of *American Institute of Physics Conference Series*, page 060006.
- SCHWARZBURG, S., 2012: A Mirror Alignment Control System for Phase II of the HESS Experiment and a Morphology Study of HESS J1837-069. Ph.D. thesis, Eberhard Karls Universität Tübingen.
- SITAREK, J.; BEDNAREK, W., 2012: GeV-TeV gamma rays and neutrinos from the Nova V407 Cygni. *Physical Review D*, 86(6):063011.

-
- STIL, J.M.; TAYLOR, A.R.; DICKEY, J.M.; KAVARS, D.W.; MARTIN, P.G.; ET AL., 2006: The VLA Galactic Plane Survey. *The Astronomical Journal*, 132:1158–1176.
- SU, Y.; ZHOU, X.; YANG, J.; CHEN, Y.; CHEN, X.; ET AL., 2017: Is HESS J1912+101 Associated with an Old Supernova Remnant? *The Astrophysical Journal*, 845:48.
- SUGIZAKI, M.; MITSUDA, K.; KANEDA, H.; MATSUZAKI, K.; YAMAUCHI, S.; ET AL., 2001: Faint X-Ray Sources Resolved in the ASCA Galactic Plane Survey and Their Contribution to the Galactic Ridge X-Ray Emission. *The Astrophysical Journal Supplement Series*, 134:77–102.
- TIAN, W.W.; LEAHY, D.A.; HAVERKORN, M.; JIANG, B., 2008: Discovery of the Radio and X-Ray Counterpart of TeV γ -Ray Source HESS J1731-347. *The Astrophysical Journal Letters*, 679:L85.
- VALLÉE, J.P., 2008: New Velocimetry and Revised Cartography of the Spiral Arms in the Milky Way — A Consistent Symbiosis. *The Astronomical Journal*, 135:1301-1310.
- VALLÉE, J.P., 2013: A Synthesis of Fundamental Parameters of Spiral Arms, Based on Recent Observations in the Milky Way. *International Journal of Astronomy and Astrophysics*, 3:20–28.
- WEEKES, T.C.; CAWLEY, M.F.; FEGAN, D.J.; GIBBS, K.G.; HILLAS, A.M.; ET AL., 1989: Observation of TeV gamma rays from the Crab nebula using the atmospheric Cerenkov imaging technique. *The Astrophysical Journal*, 342:379–395.
- WILKS, S.S., 1938: The Large-Sample Distribution of the Likelihood Ratio for Testing Composite Hypotheses. *The Annals of Mathematical Statistics*, 9(1):60–62. ISSN 0003-4851.
- WOUDT, P.A.; RIBEIRO, V.A.R.M., editors, 2014: Stella Novae: Past and Future Decades, vol. 490 of *Astronomical Society of the Pacific Conference Series*.
- YAMAGUCHI, H.; UENO, M.; KOYAMA, K.; BAMBA, A.; YAMAUCHI, S., 2004: XMM-Newton Observations of G32.45+0.1 and G38.55+0.0: Diffuse Hard X-Ray Sources Found by the ASCA Galactic Plane Survey. *Publications of the Astronomical Society of Japan*, 56:1059–1065.
- ZATSEPIN, G.T.; KUZ'MIN, V.A., 1966: Upper Limit of the Spectrum of Cosmic Rays. *Soviet Journal of Experimental and Theoretical Physics Letters*, 4:78.

A Appendix

A.1 Optical Point Spread Function Monitoring of H.E.S.S.

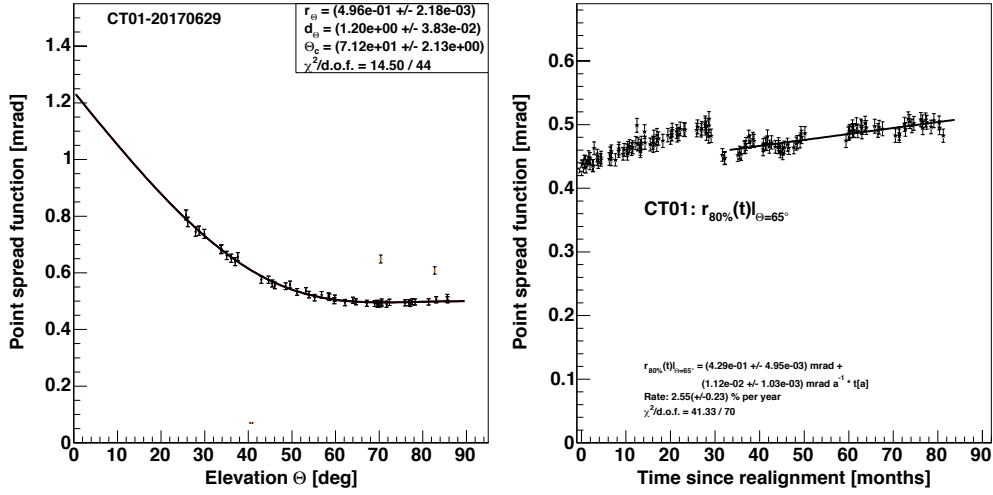


Figure A.1: Long term monitoring of the optical psf of CT1: The plot on the left shows the measured R_{80} over the elevation angle for one night. On the right, the R_{80} at 65° is shown over time. To derive this value, the function fitted to the data from one night is evaluated at 65° . Normally, the monitoring is done twice a month. A linear trend is fitted to the data.

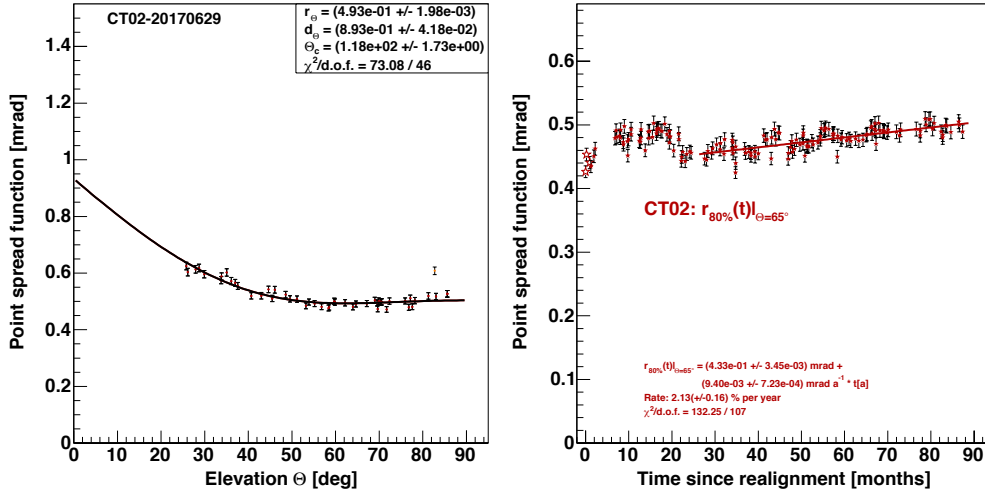


Figure A.2: Long term monitoring of the optical psf of CT2: The plot on the left shows the measured R_{80} over the elevation angle for one night. On the right, the R_{80} at 65° is shown over time. To derive this value, the function fitted to the data from one night is evaluated at 65° . Normally, the monitoring is done twice a month. A linear trend is fitted to the data.

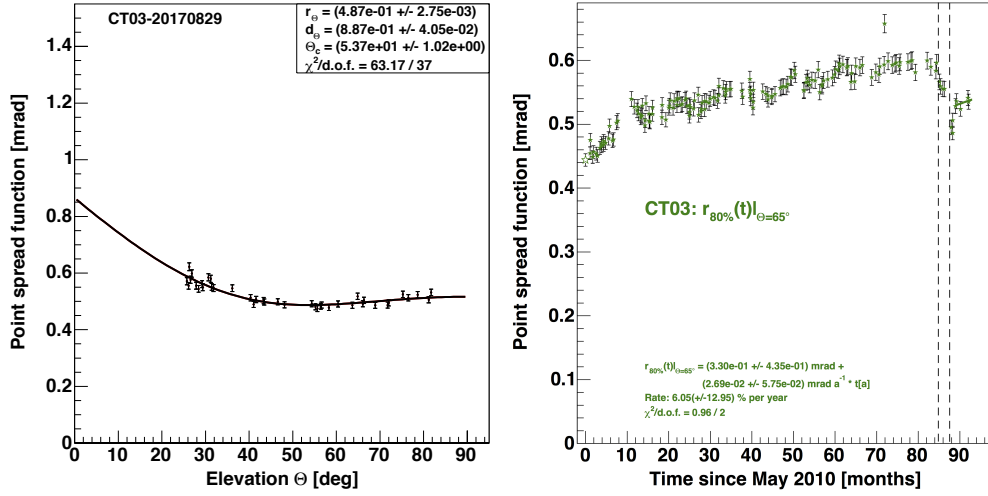


Figure A.3: Long term monitoring of the optical psf of CT3: The plot on the left shows the measured R_{80} over the elevation angle for one night. On the right, the R_{80} at 65° is shown over time. To derive this value, the function fitted to the data from one night is evaluated at 65° . Normally, the monitoring is done twice a month. A linear trend is fitted to the data. The first dotted lines indicate the time of a focusing of the lens of the CCD camera. The second dotted line shows the time of the mirror exchange.

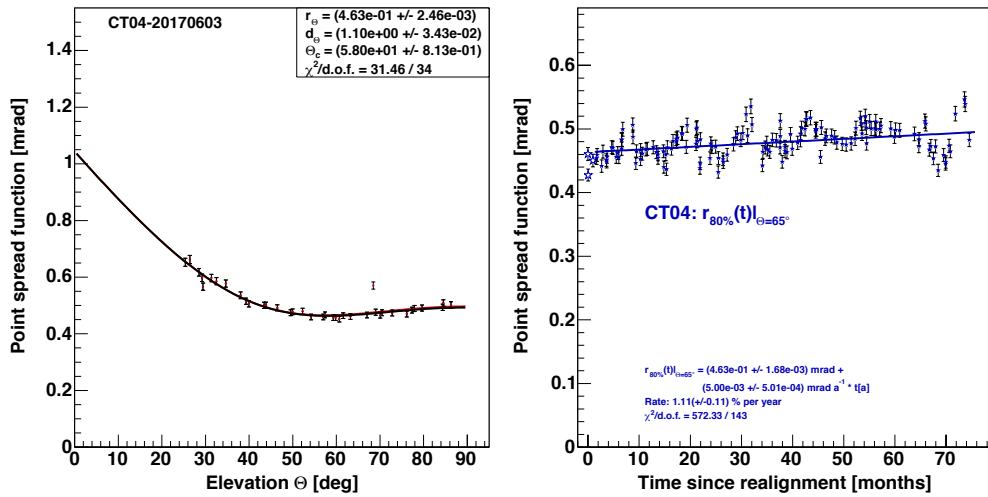


Figure A.4: Long term monitoring of the optical psf of CT4: The plot on the left shows the measured R_{80} over the elevation angle for one night. On the right, the R_{80} at 65° is shown over time. To derive this value, the function fitted to the data from one night is evaluated at 65° . Normally, the monitoring is done twice a month. A linear trend is fitted to the data.

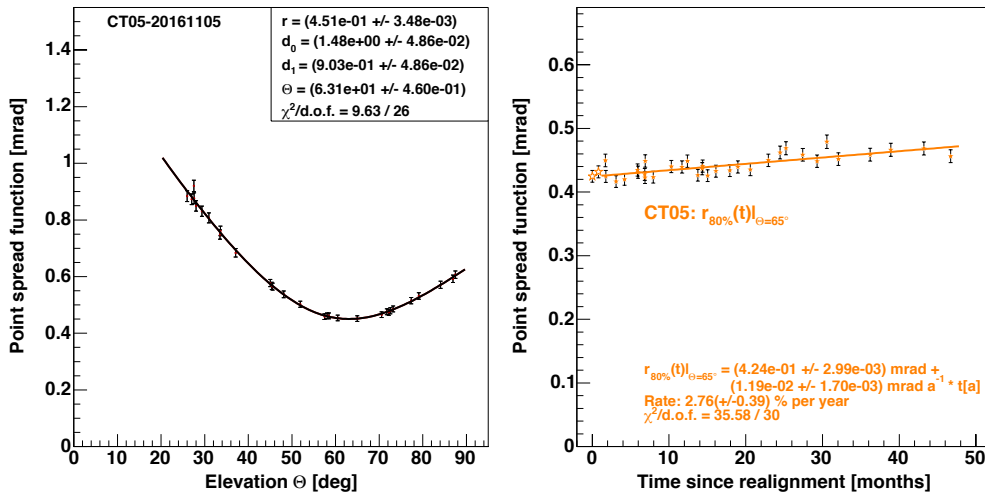


Figure A.5: Long term monitoring of the optical psf of CT5: The plot on the left shows the measured R_{80} over the elevation angle for one night. On the right, the R_{80} at 65° is shown over time. To derive this value, the function fitted to the data from one night is evaluated at 65° . Normally, the monitoring is done every second month. A linear trend is fitted to the data.

Acknowledgments

I would like to thank everyone who supported me, contributed to my work for the H.E.S.S. experiment, my studies, and the thesis presented here. This work would not have been possible without the support and friendship I got from members of the H.E.S.S. collaboration, colleagues at the IAAT, and members of the University of Tübingen. Among all these people I would like to highlight:

Prof. Dott. Andrea Santangelo: Thank you for the opportunity to work at this great institute and within the H.E.S.S. collaboration. Thank you for supervising this work, the scientific and political discussions, the coffee breaks, the dinners, and for the pasta before we went to the telescopes. Andrea, working with you was a pleasure.

Prof. Dr. Josef Jochum: Vielen Dank, dass Sie mich während meiner Promotion betreut haben, danke auch für die Organisation der Doktorandentage des Kepler Center.

Dr. Gerd Pühlhofer: Vielen Dank für Deine Betreuung und dafür, dass Du mich durch Deine kritischen Nachfragen immer einen Schritt weiter gebracht hast. Danke außerdem für Deine Unterstützung innerhalb der Kollaboration, aber auch dafür, dass ich sehr eigenständig an meinen Projekten arbeiten durfte.

Dr. Jan-Christoph Tenzer: Danke für die vielen Unterschriften, die Motivationsgesprächen, das Gefühl, dass es für jedes Problem eine Lösung gibt, und für die Kaffeepausen.

Massimo Capasso: Massimo, thanks for sharing an office with me, the coffee, the talks, the fun we had and of course your contribution to our great paper. Thanks for watering my plants, they would not have survived me without you.

Stefan Schwarzburg und **Andreas Förster:** Vielen Dank für Eure Hilfe, während ich meine ersten Schritte in der H.E.S.S.-Kollaboration gemacht habe. Es war mir eine Freude, mit Euch zusammenzuarbeiten.

Of all the great colleagues of the H.E.S.S. collaboration a special thanks goes to **Benjamin, Dan, Heike, Johannes, Phillip, Stefan, Thomas** and **Vincent** for their

ACKNOWLEDGMENTS

help with HAP, the DAQ and (more or less) fruitful discussions in the evenings of H.E.S.S.- and other meetings.

This work would not have been possible without the **local crew of H.E.S.S.** Thank you for the repeated warm welcome, the braai and the beer. Special thanks to **Volker** and his wife for their hospitality.

Für die morgendlichen Kaffeepausen und das Funktionieren der IT möchte ich mich bei **Heinz** bedanken, für die Hilfe beim “Verwaltungskram” und die gelegentlichen morgendlichen Busfahrten bei **Angela** und für den ganzen Mist mit den Spiegeln bei **Radu** und **Mathias**.

Besonderer Dank gebührt der Werkstatt des Instituts. Egal wie bescheuert mein Vorschlag war, am Ende ist immer etwas Praktikables raus gekommen.

I thank **Alexjandro, Conny, Gabi, Jörg, Laura, Martina, Samuel, Sara, Sebastian** and **Stephanie**. Sharing Pizza, coffee and the occasional drink with you was always fun and your friendship and support made all the difference in the last years.

Liebe **Karola**, vielen Dank für die vielen Pakete und das Mitfiebern.

Ich danke meiner ganzen Familie. Ohne die Unterstützung durch meine Eltern und meine Brüder wäre ich nie soweit gekommen.

Liebe **Ruth**, vielen Dank für die letzten Jahre. Du warst jederzeit für mich da, ohne Dich gäbe es diese Arbeit nicht.